NanoSQUID Magnetometers and High Resolution Scanning Squid Microscopy

Aico Troeman

Ph.D. committee

Chairman
Prof. Dr. F.G. Mugele, University of Twente

Secretary
Prof. Dr. Ing. M. Wessling, University of Twente

Supervisor
Prof. Dr. Ir. J.W.M. Hilgenkamp, University of Twente

Members
Prof. Dr. J.R. Kirtley, Chalmers University of Technology
Prof. Dr. V.V. Moshchalkov, Katholieke Universiteit Leuven
Prof. Dr. Ir. J.E. Mooij, Delft University of Technology
Prof. Dr. Ir. H.J.W. Zandvliet, University of Twente
Prof. Dr. Ir. J. Huskens, University of Twente

Cover: Artist's impression of a nanoSQUID based on superconducting bridges, created by Jeroen Huijben.

The research described in this thesis was performed in the Faculty of Science and Technology and the MESA$^+$ Institute for Nanotechnology of the University of Twente. The project was primarily supported by the Netherlands Organization for Scientific Research (NWO) through a VIDI grant. Additional support was provided by the IBM T.J. Watson Research Center, Yorktown Heights, USA, by the European Science Foundation (ESF) PiShift programme, by the Dutch foundation for research on matter (FOM), and by the NanoNed programme of the Dutch Technology Foundation (STW).

A.G.P. Troeman
NanoSQUID Magnetometers and High Resolution Scanning SQUID Micrscopy,
Ph.D. Thesis, University of Twente, Enschede, the Netherlands

ISBN 978-90-365-2572-5

Printed by PrintPartners Ipskamp, Enschede, the Netherlands

NANOSQUID MAGNETOMETERS AND HIGH RESOLUTION SCANNING SQUID MICROSCOPY

PROEFSCHRIFT

ter verkrijging van
de graad van doctor aan de Universiteit Twente,
op gezag van de rector magnificus,
prof. dr. W.H.M. Zijm,
volgens besluit van het College voor Promoties
in het openbaar te verdedigen
op donderdag 13 december 2007 om 15.00 uur

door

Aico Giardano Paul Troeman

geboren op 28 november 1980
te Eindhoven

Dit proefschrift is goedgekeurd door de promotor:

Prof. Dr. Ir. J.W.M. Hilgenkamp

"*Any intelligent fool can make things bigger, more complex, and more violent. It takes a touch of genius -- and a lot of courage -- to move in the opposite direction*"

Albert Einstein, 1879 – 1955

Table of Contents

Chapter 1
Introduction

Throughout the history of mankind the desire and will to explore the unknown has always played a central role. This desire not only focuses on the exploration of major unknown objects such as "the new world", but also on the investigation of properties which cannot be detected with the use of only the human senses. One of the best known examples of such studies is research conducted with an optical microscope.

The earliest optical microscope, yielding a magnification of ten, consisted of a tube with a plate for the object that was to be investigated on the one end and a simple lens on the other side. It is hard to pinpoint the first invention of a compound microscope, which consists of a system of several lenses. Two Dutch spectacle makers, Zaccharias Janssen and his son Hans, are considered to be the self-proclaimed first inventors, even though the date (1590) they report to have invented their optical microscope is considered to be highly unlikely. Another likely fist inventor was Galileo, who developed a multi lens system in 1609, before Anton van Leeuwenhoek, who is considered to be the father of microscopy, developed systems based on polished lenses, with considerable curvature, at the end of the 17^{th} century.

With this new equipment the investigation of small (microscopy) or distant (telescopy) objects became possible. Nowadays, the light microscope is an indispensable scientific instrument on which much of modern science is based. With the advances in technology, the development of microscopy has not only focused on the amplification of the senses already possessed by man, but also on the inspection of new properties.

In this thesis the detection of very small variations in the magnetic flux above an object is described. Apart from the fact that this is also a form of microscopy there is one more similarity between this work and the first development of microscopy: It is based on the desire to investigate quantities that are undetectable with commonly available equipment.

1.1 Motivation

In 1962 Brian Josephson predicted that a supercurrent could tunnel through an insulating barrier separating two superconducting materials [1]. The formulation of this theory, though met with a lot of resistance at that time, proved to be the starting point for the development of what are nowadays known as Josephson devices. One type of such devices, the Superconducting QUantum Interference Device (SQUID), is the most sensitive detector of magnetic field that is currently available. Any physical quantity that can be converted into a magnetic flux (such as magnetic field, magnetic field gradient, current, voltage or displacement) can be measured with these sensors. Since their discovery, SQUIDs have been applied in a wide scope of applications, ranging from the detection of human brainwaves to the observation of single atomic spin flips [2]. In the first part of this thesis the development of miniaturized SQUID structures is described. The development and application of SQUIDs in scanning SQUID microscope systems are described in the second part.

Recent interest in the development of miniature SQUIDs has been motivated by the applicability of these sensors for investigations of small, local, magnetic signals, such as the magnetization reversal of small magnetic clusters deposited inside the SQUID [3,4,5,6] and the observation of local magnetic structures using a scanning SQUID microscope (SSM) [7,8,9,10]. Further miniaturization of the sensors offers a possibility to increase the sensitivity and spatial resolution of these experiments. Also, the realization of miniaturized SQUIDs patterned in three dimensions, e.g. on the tip of an AFM cantilever, could significantly improve on the resolution of SSM systems.

The size of SQUIDs based on conventional superconductor – insulator – superconductor (S-I-S) tunnel junctions is limited by the lithography process. Even if the junctions can be miniaturized, achieving a sufficiently high critical current (I_0) would pose a limitation on the size of an eventual SQUID. Based on a standard 4.5 kA/cm^2 process [11], a 100 x 100 nm^2 junction would have an I_0 of approximately 0.5 μA. The RSJ noise parameter $\Gamma = 2\pi k_b T/I_0\Phi_0$, describing the ratio of the thermal and Josephson coupling energies, at $T = 4.2$ K, of such a structure would have a value of approximately 0.35, resulting in noise–rounded current–voltage (IV) characteristics and reduced performance.

Superconducting nanobridges, exhibiting non–trivial current–phase relationships and high current densities [12], can be very suitable alternatives to tunnel junctions. These structures can be created in a single nano–patterning step. By patterning two nanobridges in a miniature superconducting ring a DC SQUID with sub–micrometer effective area ($A_{eff} = \Phi_0/H_0$, where Φ_0 is the magnetic flux quantum (h/2e ≈ 2 x 10^{-15} Tm^2) and H_0 the applied field for which a SQUID completes one voltage oscillation) can be created. SQUIDs based on nanobridges, patterned by means of electron beam lithography (EBL), have been reported in the literature [5,7,8,13]. Recently, also small

SQUIDs with Carbon nanotubes as junctions have been reported [6], though these sensors were not really miniaturized in terms of their effective area. In the first part of this thesis, SQUIDs based on Niobium nanobridges, produced by focused ion beam (FIB) milling, are described. Compared to EBL, FIB nano–patterning offers the advantage of not being limited to flat surfaces, which allows for the creation of devices patterned in three dimensions, as demonstrated e.g. in [14]. The smallest realized sensor has an effective area of 3.6 x 10^{-2} μm^2, which is believed to be smaller than any SQUID reported in literature. Determination of the properties of such devices also has a more fundamental interest since, in contrast to SQUIDs based on SIS junctions, no model describing the complete behavior of these sensors is currently available. It is thus not yet clear what sensor properties and performance can be achieved.

As mentioned before, the second part of this thesis focuses on the experimental detection of local magnetic flux patterns above a sample. The described measurements are conducted with scanning SQUID microscopy systems, which are based on the widely applied principle of scanning probe microscopy (SPM). Even though profilometers had been in use for several decades (e.g. in [15] (1956)), the first example of an SPM system is considered to be the invention of the Scanning Tunneling Microscope (STM) in 1981 [16]. This triggered the development of many related SPM techniques, such as Atomic Force Microscopy (AFM) [17]. STM systems are widely used to probe the tunnel probability of electrons from a voltage–biased tip to a conducting sample as a function of position. With AFM the topography of a sample can be sensed down to the atomic scale. A different application of the SPM technique can be found in Magnetic Scanning Probe Microscopes (MSPM), with which the magnetic characteristics of a sample can be investigated. Systems based on different magnetic sensors, such as Hall probe and magnetic force microscopes, were developed. Given their unprecedented magnetic sensitivity, the application of SQUIDs as the magnetic field detectors in a scanning probe microscope yielded the type of magnetic microscope with the highest magnetic sensitivity [18]. These systems are nowadays known as Scanning SQUID Microscopes (SSM). The aim of the SSM–based research described in this thesis is the development of high–resolution scanning SQUID microscopy. The typical spatial resolutions of scanning SQUID microscope systems are of the order of 10 - 50 microns. This value is limited by the diameter of the sensing area, which is commonly a pick–up loop structure in direct connection to the SQUID washer, and the separation of sensor and sample during measurements. By minimizing both the effective sensor area relative to the sample and the sensor to sample separation, improvements in the spatial sensitivity during SSM operation could in principle be achieved.

As an introduction different topics will be shortly discussed in this first chapter. In the next two paragraphs a brief description of generally used models for Josephson tunnel junctions and DC SQUID operation is given. The fourth paragraph is dedicated to an

introduction to the SSM technique, followed by an outlook on the rest of the thesis in the last section.

1.2 General theory

The Josephson effect

As described before, Josephson predicted that a supercurrent could tunnel through an insulating barrier separating two superconducting electrodes [1]. He formulated two equations describing such a structure:

$$I_s = I_0 \sin(\varphi) \tag{1.1}$$

$$V = \frac{\hbar}{2e}\frac{d\varphi}{dt} \tag{1.2}$$

Equation (1.1) describes the superconducting current (I_s) as a function of the critical current (I_0) and the phase difference (φ) between the superconducting order parameters of the two electrodes. In equation (1.2) the relationship between the voltage (V) across the junction and the time–derivative of this phase difference is described (this is known as the AC Josephson effect). From these equations it can be concluded that a time-averaged voltage $<V>$ across the junction will induce a supercurrent with amplitude I_0, oscillating at the Josephson frequency ($\omega_j = 2e/h \approx 483.6$ MHz/μV).

As described by Likharev [12], the Josephson effect is not only a characteristic of superconductor – insulator – superconductor (SIS) junctions, but of any weak link. These structures can be defined as conducting junctions between superconducting electrodes of which the critical current is much smaller than that of the electrodes. The sinusoidal dependence of the supercurrent described by equation (1.1) is only valid for S-I-S junctions, where the width of the barrier is comparable to, or less than, the superconducting coherence length (ξ). Several deviations from this "ideal Josephson effect" can exist in different types weak links. Equation (1.2), however, is derived from the main principles of quantum mechanics and contains only fundamental constants. It holds for any type of weak link.

Fluxoid and Flux Quantization

The fact that the magnetic flux in a superconducting ring is quantized was first predicted by F. London [19]. He based this assumption on the theory describing the two basic electrodynamic properties of superconductivity. However, it was not until the formulation of the microscopic BCS theory describing the pair–forming of electrons in superconductors [20], that this phenomenon was fully understood.

In a superconductor, the electrons condense into Cooper pairs, all occupying the same macroscopic quantum state, which can be described by the complex wave function: $\Psi = |\Psi| e^{i\varphi r}$. The phase of this wave function is dependent on the supercurrent density J_s and the magnetic vector potential A. This relationship can be described by [21]:

$$\nabla\varphi = 2\pi\left(\frac{2m}{hn_s e}J_s + \frac{2e}{h}A\right) \tag{1.3}$$

In this equation the mass ($2m$) corresponds to the mass of two electrons forming a Cooper pair. The superconducting electron density is denoted by n_s. To ensure the single–valuedness of the complex wave function the phase difference across an arbitrary closed path can only vary by an integer times 2π. This gives the fluxoid (Φ') quantization condition:

$$\Delta\varphi = 2\pi\frac{2e}{h}\left(\frac{m}{n_s e^2}\int_{contour} J_s dl + \int_{contour} A dl\right) = 2\pi\frac{2e}{h}\Phi' = n2\pi \tag{1.4}$$

Rearranging this equation and applying the theory of Stokes gives:

$$\frac{m}{n_s e^2}\int_{contour} J_s dl + \int_{area} B da = \Phi' = n\frac{h}{2e} = n\Phi_0 \tag{1.5}$$

In this equation Φ_0 is the magnetic flux quantum ($h/2e \approx 2.07 \times 10^{-15}$ Wb). If the radius of the integration path is taken to be several times larger than the magnetic penetration depth (λ_L), i.e. the supercurrent is zero over the entire integration path, the equation can be further reduced to the familiar flux (Φ) quantization condition:

$$\int_{area} B da = \Phi = n\Phi_0 \tag{1.6}$$

Josephson Inductance

A Josephson junction can be modeled as a highly nonlinear inductance [22]. This lossless element exhibits a kinetic inductance in much the same way as a superconducting thin film. For a classical Josephson tunnel junction (equation 1.1) one can derive an expression for the Josephson inductance as follows:

The time integral of the voltage equals the fluxoid. Using equation 1.2 this leads to the following expression:

$$\Phi' = \int V dt = \frac{\Phi_0 \varphi}{2\pi} \tag{1.7}$$

Rearranging and inserting this result in equation 1.1 yields:

$$I_s = I_0 \sin\left(\frac{2\pi\Phi'}{\Phi_0}\right) \tag{1.8}$$

The effective kinetic inductance is the slope of $\Phi'(I)$, which can be calculated from equation 1.8:

$$\frac{\partial\Phi'}{\partial I_s} = \frac{\Phi_0}{2\pi I_0} \frac{1}{\sqrt{1-\left(I_s / I_0\right)^2}} \tag{1.9}$$

In the linear regime of this equation ($I_s << I_0$) this gives the following expression for the Josephson inductance L_{jo}:

$$L_{jo} = \frac{\Phi_0}{2\pi I_0} = \frac{\hbar}{2eI_0} \tag{1.10}$$

For a tunnel junction with a critical current of 100 μA this corresponds to a Josephson inductance of about 3 pH at $I_s << I_0$.

1.3 DC SQUIDs

Direct current (DC) SQUIDs basically consist of a superconducting loop interrupted by two Josephson junctions, or two of any other type of weak link exhibiting a non-trivial current–phase relationship. The sensitivity to changes in magnetic flux of these devices is

based on two physical effects: the Josephson effect and the quantization of magnetic flux in a superconducting ring, both of which were shortly reviewed in the previous section.

In figure 1 - 1 a schematic representation of a DC SQUID is shown. The descriptions in this section are limited to SQUIDs which consist of two Josephson tunnel junctions. According to the RCSJ model [23], these elements can be modeled as a parallel combination of a (external) shunt resistor R_j, a capacitor C_j, and an element representing the critical current. It is assumed that the shunt resistor is large enough to eliminate hysteresis in the current–voltage (IV) characteristics of the junctions. This assumption is valid if the McCumber parameter β_c is smaller than unity:

$$\beta_c = \frac{2\pi I_0 R_j^2 C_j}{\Phi_0} < 1 \tag{1.11}$$

The IV characteristics of DC SQUIDs exhibit periodic behavior (1 period = 1 Φ_0) as a function of the applied magnetic flux (figure 1 - 2).

Commonly, DC SQUID measurements are conducted by biasing the device with a current which is somewhat larger than the SQUID critical current (I_c) and measuring the voltage as a function of the applied magnetic field (see figure 1 - 2). The critical current modulation depth, defined as the difference between the maximum and minimum values of I_c, is dependent on the inductance of the SQUID loop.

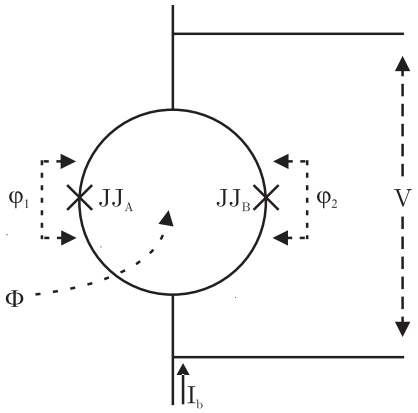

Figure 1 - 1:
Schematic representation of a DC SQUID. The Josephson junctions (JJ_A and JJ_B) are represented by the crosses, with the corresponding differences of the phases of the complex wave functions denoted by φ_1 and φ_2. Typically a DC SQUID is operated by biasing the device at a constant current (I_b) and measuring the change in the voltage (V) as a function of the applied magnetic flux (Φ).

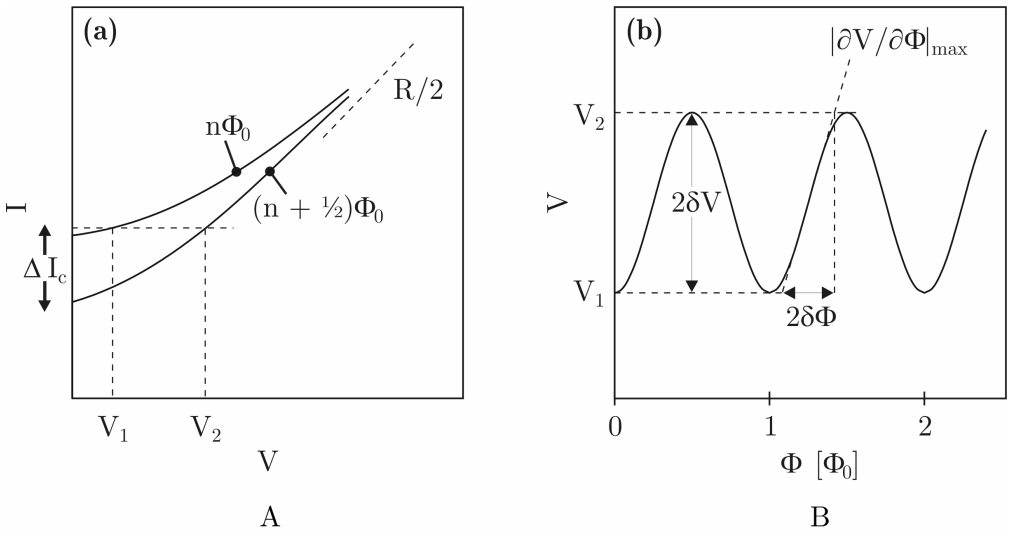

Figure 1 - 2:

(A) Schematic representation of the current–voltage (IV) characteristic of a DC SQUID as a function of the applied magnetic flux. The two limiting situations, occurring for $\Phi = n\,\Phi_0$ and $\Phi = (n+{}^1/_2)\,\Phi_0$ are shown.

(B) DC SQUID voltage modulation characteristic as a function of applied magnetic field, measured at a constant bias current.

In the strong screening limit the loop inductance (L_s) is much larger than the total Josephson inductance (L_{jo}) of both junctions:

$$\frac{L_s}{L_{jo}} = \frac{2\pi L_s I_0}{\Phi_0} >> 1 \tag{1.12}$$

In this case the maximum screened flux corresponds to half a flux quantum, which induces a circulating screening current of $\Phi_0/2L_s$. This limits the maximum SQUID modulation depth to:

$$\Delta I_c \leq \frac{\Phi_0}{L_s} \tag{1.13}$$

In the other limit, where the loop inductance is small compared to the Josephson inductance of the two junctions, there will be no screening current (I_s) induced by the applied magnetic flux in the SQUID loop since this flux will be completely divided over the kinetic inductances of the junctions.

The optimum situation occurs when the total Josephson and loop inductances are comparable. Calculations have shown the best performance is achieved when:

$$\frac{2I_0L_s}{\Phi_0} = \beta_L \approx 1 \tag{1.14}$$

Here β_L is known as the screening parameter or reduced inductance. For this situation the critical current modulation of the SQUID can be approximated by:

$$\Delta I_c = \frac{1}{1+\beta_L} 2I_0 \tag{1.15}$$

For a complete description of this intermediate regime reference is made to Tinkham [24]. As stated before, most of the modeling described here is applicable to superconducting interference devices based on classical Josephson tunnel junctions, for which the current phase relationship (CPR) can be described by equation 1.1. However, since SQUIDs are merely based on the incorporation of superconducting elements exhibiting a non–trivial CPR in a superconducting ring, also other types of elements can be used. As described in section 1.1, superconducting nanobridges also exhibit a non–trivial CPR. In chapter 2, a more detailed description of these structures, the type of weak link used when fabricating the miniaturized SQUID structures described in this thesis, will be given.

Noise in DC SQUIDs based on resistively shunted SIS junctions

The dominant noise source in DC SQUIDs based on resistively shunted SIS junctions is Johnson noise, which can be described by the following voltage noise spectral density ($S_v^{1/2}$) [25]:

$$S_v^{1/2} \approx \gamma 2k_BTR \tag{1.16}$$

Here $\gamma\,(\approx 8)$ is a factor associated with down-mixing of Johnson noise generated at the Josephson frequency and R is the shunting resistor of a single junction. Based on this equation the corresponding flux noise spectral density can be calculated as follows:

$$S_\Phi = \frac{S_v}{(\partial V/\partial\Phi)^2} \approx \gamma \frac{2k_BTL_{sq}^2}{R}\left(\frac{1+\beta_L}{2\beta_L}\right)^2 \tag{1.17}$$

The equation described above is only valid for devices where $\beta_L \approx 1$. Typical white flux noise spectral densities of optimized non–hysteretic DC SQUIDs are in the order of:

$$\sqrt{S}_{\Phi} \approx 1\mu\Phi_0 / \sqrt{Hz} \tag{1.18}$$

Since the flux noise spectral density scales with the SQUID inductance, it is convenient to compare different devices by means of their energy resolution, which is defined by:

$$\varepsilon = \frac{S_{\Phi}}{2L_{sq}} \tag{1.19}$$

In applications where SQUID measurements are required to be conducted down to low frequencies, the $1/f$ contribution to the total noise starts to play a role. At least three separate sources of $1/f$ noise can be distinguished in DC SQUIDs based on SIS resistively shunted junctions [26]. The first is associated with the trapping of electrons in defects in the junction tunnel barriers. Next to this $1/f$ noise is also caused by the motion of flux lines which are trapped in the SQUID. Recently, $1/f$ noise has also been associated with the magnetic moments of electrons trapped in defect states in the superconductor [27].

1.4 Scanning SQUID microscopy

As described in the first section of this chapter, scanning SQUID microscopy is a form of SPM where a SQUID sensor is used to map the magnetic flux at a certain height above the surface of the sample which is to be investigated. In figure 1 - 3 the basic setup of a scanning probe microscope is schematically shown. By scanning a sensor across the surface of a sample an image can be created depicting the sensed value as a function of the relative position between the sample and the sensor.

Many different techniques for measuring the local magnetic field or flux above the surface of a sample exist. A comparison of the spatial and magnetic resolutions of different types of systems is shown in figure 1 - 4. Decoration techniques [28], are known for their relative simplicity. Magneto–optical imaging [29], also a relatively simple technique, allows for time–resolved studies and with scanning electron microscopy [30] and electron holography [31] high spatial resolutions can be achieved. Magnetic force microscopy [32] can be used to combine topographic and magnetic information. Finally, scanning Hall probe microscopy [33] is a technique which, resulting from the relatively high sensitivity and small sensors, yields a high flux resolution. The main advantage of scanning SQUID microscopes is the unprecedented magnetic sensitivity of the SQUID sensors.

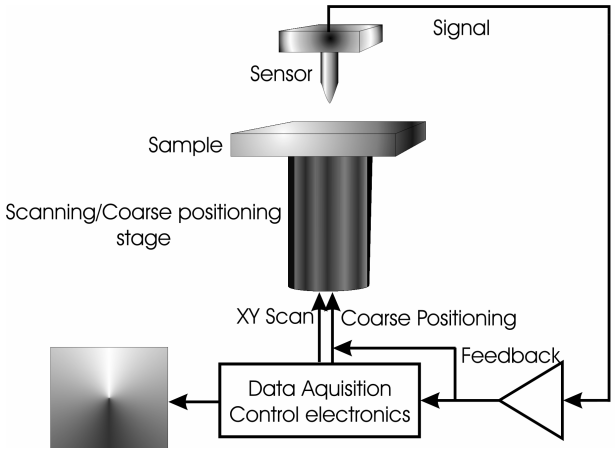

Figure 1 - 3:
Schematic representation of a scanning probe microscopy setup.

A comparison of these different imaging techniques can be found in [18] and [34]. The comparison shown in figure 1 - 4 is still relatively up–to–date, though miniaturized techniques for SHPM [35], MFM [36] and SSM [7] have been reported in the literature over the past years. These latter three techniques are considered the most commonly used to map the magnetic stray field (flux) above a sample.

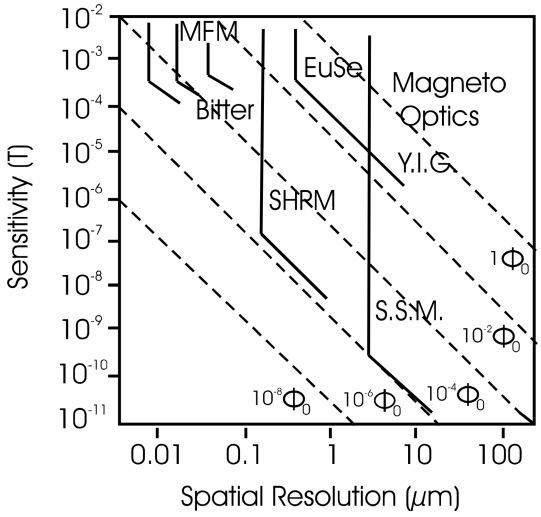

Figure 1 - 4:
Comparison of the spatial and magnetic sensitivities of different magnetic microscopy techniques. This figure was published in [18].

Each of the described forms of magnetic microscopy poses specific limitations on possible experiments. With MFM sensors very high spatial resolutions can be achieved, though the acquired data is a map of the local magnetic force acting on the magnetic dipoles of the tip instead of an image of the magnetic flux at a certain point above a sample. To transform this acquired data back into an image of the magnetic flux distribution above the sample, complex mathematical operations should be performed. Furthermore, the magnetic sensitivity is limited compared to SSM systems. This last limitation also holds for SHPM systems. Recently, however, magnetic exchange force microscopy (MExFM) has been proposed [37,38]. With this MFM–like technique, short range magnetic exchange forces between tip and sample are measured. The first report of the experimental realization of such a microscopy setup has recently been made [39]. By aligning the tip and sample moments in a 5 Tesla background field, atomic resolution was achieved. In terms of the reduction of flux sensitivity (as in figure 1 - 4) this technique thus offers significant improvements. The main limitation of the presented measurements, however, arises from the necessity to perform the experiments in a relatively large background field. Another MFM-like technique is Magnetic Resonance Force Microscopy. Sub-micron resolutions and single spin sensitivities have been reported for such microscopes [40]. For these experiments, however, a microwave magnetic field should be applied to the sample.

For many experiments achieving high magnetic sensitivities is not relevant. There are, however, specific cases, such as for the measurements of fractional half flux quanta [10], where MFM and SHPM measurements do not suffice and SSM experiments are the only viable option. The spatial resolution of these measurements is, however, limited compared to MFM and SPHM. Furthermore, in contrast to the sensors in these latter techniques, SQUID operation requires a cryogenic sensor environment.

From the discussion of different magnetic imaging techniques presented above it can be concluded that, in principle, the used technique should be adapted to the specific experiment. In this thesis SSM measurements will be described. Apart from the realization of such setups and experiments, also the miniaturization of existing SSM sensors will be discussed.

After the first report of a scanning SQUID microscope [41], several state of the art systems, such as the ones described by Kirtley [42,43], Hasselbach [44,45] and Morooka [46], have been developed. As mentioned before, the advantages of the technique are the high magnetic sensitivity and bandwidth. However, the modest spatial resolution and the need to cool the sensor below its superconducting transition temperature pose limitations on the applicability of scanning SQUID microscopes. Some SPM systems, such as AFM or STM, use a feedback signal to control the separation between the tip and the sample. For scanning SQUID microscopes it is, however, common to operate with the sensor chip in direct contact with the sample. Apart from the fact that most SQUID chips have proven to be robust enough to survive long term operation in this way, this measurement technique is facilitated by the fact that the characteristic sensor size is usually a lot

larger than the height differences on the surface of the sample, which limits the need to compensate for measured flux differences associated with the lateral movement of the sensor relative to the sample.

1.5 Outline

In the first part of this thesis, which covers chapters 2 and 3, a description of the theory, fabrication method and characterization of Nb nanobridges and nanobridge–based SQUIDs is given. Firstly, the origin of the current–phase relationship in superconducting nanobridges is discussed in the first section of chapter 2, followed by a description of the fabrication methods of Nb nanobridges and measurements on these structures in the rest of the chapter. In chapter 3 SQUIDs based on Nb nanobridges are described.

The second part of this thesis is devoted to SSM experiments. In chapter 4 an overview of the measurement techniques, systems and sensors is given, followed by a description of different measurement results in the next chapter. In the last chapter of this thesis an outlook on future experiments and applications based on the described research is given.

Bibliography

[1] **B.D. Josephson**; Phys. Lett 1, 251 (1962)

[2] **J.C. Gallop**; Jour. Phys. E (Scientific Instruments) 9, 417 (1967)

[3] **M. Jamet, W. Wernsdorfer, C. Thirion, D. Mailly**, **V. Dupuis, P. Mélinon, and A. Pérez**; Phys. Rev. Lett. 86, 4676 (2001)

[4] **J. Gallop, P.W. Joseph – Franks, J. Davies, L. Hao and J. Macfarlane**; Phys C 368, 109 (2002)

[5] **S.K.H. Lam and D.L. Tilbrook**; Appl. Phys. Lett. 82, 1078 (2003)

[6] **J.-P. Cleuziou, W. Wernsdorfer, V. Bouchiat, T. Ondarçuhu and M. Monthioux**; Nature Nanotech. 1, 53 (2006)

[7] **K. Hasselbach, C. Veauvy and D. Mailly**; Phys. C 332, 140 (2000)

[8] **C. Veauvy, K.Hasselbach and D. Mailly**; Rev. Sci. Instrum. 73, 3825 (2002)

[9] **K. Chen, P. Magnelind, P. Larsson, A.Y. Tzalenchuk and Z.G. Ivanov**; Phys C 372-376, 63 (2002)

[10] **H. Hilgenkamp, Ariando, H.-J. Smilde, D.H. Blank, G. Rijnders, H. Rogalla, J.R. Kirtley and C. C. Tsuei**; Nature 442, 50 (2003)

[11] Hypres Niobium Integrated Circuit Fabrication, Proces #03-10-45 Design Rules, Revision 23 (2006)

[12] **K.K. Likharev**; Rev. Mod. Phys. 51, 101 (1979)

[13] **R.F. Voss, B. Laibowitz, M.B Ketchen and A.N. Boers**; "Superconducting Quantum Interference Devices and their Applications", H.D. Hahlbohm and H. Luebigg (eds.), W. de Gruyter, pp. 365 (1980)

[14] **M.G. Blamire**; Supercond. Sci. Technol. 19, S132 (2006)

[15] **N. Stolow**; J. Sci. Instrum. 33, 333 (1956)

[16] **G. Binnig and H. Rohrer**; Scientific American 253,40 (1985)

[17] **G. Binnig, C.F. Quate and Ch. Geber**; Phys. Rev. Lett 56, 930 (1986)

[18] **S. Bending**; Adv. Phys. 48, 449 (1999)

[19] **F. London and H. London**; Proc. Roy. Soc. A149, 71 (1935)

[20] **J. Bardeen, L.N. Cooper and J.R. Schrieffer**; Phys. Rev. 108, 1175 (1957)

[21] **L. Solymar**; Superconductive Tunneling and Applications, Chapman and Hall Ltd., London (1972)

[22] **A.M. Kadin**; Introduction to Superconducting Circuits, John Wiley & Sons inc, USA (1999)

[23] **W. Buckel and R. Kleiner**; Superconductivity, Wiley –VCH Verlag CmbH & Co. KGaA, Germany (2004)

[24] **M. Tinkham**; Introduction to Superconductivity, McGraw-Hill Inc, USA (1975)

[25] **C.D. Tesche and J. Clarke**; J. Low Temp. Phys. 29, 301 (1977)

[26] **R.H. Koch, J. Clarke, W.M. Goubau, J.M. Martinis, C.M. Pegrum and D.J. van Harlingen**; J. Low Temp. Phys. 51, 207 (1983)

[27] **R.H Koch**, **D.P. DiVicenzo and J. Clarke**;arXiv.org:cond-mat/0702025 (2007)

[28] **D.J. Bishop, P.L. Gammel, D.A. Huse and C.A. Murray**; Science 255, 165 (1992)

[29] **S. Gotoh and N. Koshizuka**; Phys. C 176, 300 (1991)

[30] **M.R. Scheinfein, J. Unguria, M.H. Kelley, D.T. Pierce and R.J. Celotta**, Rev. Sci. Instrum; 61, 2501 (1990)

[31] **K. Harada, T. Matsuda, J. Bonevich, M. Igarashi. S. Kondo, G. Pozzi, U. Kawabe and A. Tonomura**; Nature 360, 51 (1992)

[32] **D. Rugar, H.J. Mamin, S.E. Kambert, J.E. Stern, L. McFadyen and T. Yogi**; J. Appl. Phys. 68, 1169 (1990)

[33] **A.M. Chang, H.D. Dallen, L. Harriott, F. Hess, L. Kao, R.E. Miller, R. Wolfe, T.Y. Chang and J. van der Ziel**; Appl. Phys. Lett. 61, 1974 (1992)

[34] **L.N. Vu and D.J. van Harlingen**; IEEE Trans. Appl. Supercond. 3, 1918 (1993)

[35] **H. Kuramochi, T. Uzumaki, M. Yasutake, A. Tanaka, H. Akinaga and H. Yokohama**; Nanotech. 16, 24 (2005)

[36] **A.S. Sandhu, H. Sanbonsugi, I. Shibasaki, M. Abe and H. Handa**; J. Appl. Phys. 43, 777 (2004)

[37] **R. Wiesendanger, D. Bürgler, G. Tarrach, A. Wadas, D. Brodbeck, H.-J. Güntherodt, G üntherodt, R.J. Gambino and R. Ruf**; J. Vac. Sci. Technol. B 9, 519 (1991)

[38] **K. Nakamura, H. Hasegawa, T. Oguchi, K. Seuoka, K. Hayakawa and K. Musaka**; Phys. Rev. B 56, 3218 (1997)

[39] **U. Kaiser, A. Schwarz and R. Wiesendagner**; Nature 446, 522 (2007)

[40] **D. Rugar, R. Budaklan, H.J. Mamin and B.W. Chul**; Nature 430, 329 (2005)

[41] **FP Rogers**; BS/MS thesis, EICS Department, MIT (1983)

[42] **J.R. Kirtley, M.B. Ketchen, C.C. Tsuei, J.Z. Sun, W.J. Gallagher, L.S. Yu-Jahnes, A. Gupta, K.G. Stawiasz and S.J. Wind**; IBM J. Res. Develop. 39, 656 (1995)

[43] **J.R. Kirtley, M.B. Ketchen, C.C. Tsuei, J.Z. Sun, W.J. Gallagher, L.S. Yu-Jahnes, A. Gupta, K.G. Stawiasz and S.J. Wind**; Appl. Phys. Lett. 66, 1138 (1995)

[44] **K. Hasselbach, C. Veauvy and D. Mailly**; Phys. C. 332, 140 (2000)

[45] **C. Veauvy, K. Hasselbach and D. Mailly**; Rev. Sci. Instrum 73, 3825 (2002)

[46] **T. Morooka, S. Nakayama, A. Odawara, M. Ikeda, S. Tanaka and K. Chinone**; IEEE Trans. Appl. Supercond. 9, 3491 (1999)

Chapter 2

Superconducting Nanobridges

As mentioned in chapter one, the Josephson effect is not only a characteristic of "classical" superconductor – insulator – superconductor (S-I-S) tunnel junctions, where the coupling of the order parameters of the two superconducting electrodes is a result of the tunneling of Cooper pairs through the barrier, but also of other types of superconducting weak links. A superconducting weak link can be defined as a structure with reduced critical current separating two relatively bulky superconducting electrodes. In contrast to the conventional S-I-S junctions described above, the current in these devices flows along a conducting, either superconducting or normal, path. The best–known examples of such weak links are superconductor – normal metal – superconductor (S-N-S) junctions, where the Josephson effect is the result of the coupling of the superconducting wave functions due to proximity effects in the barrier.

In this chapter another type of weak link will be described, namely the superconducting nanobridge. These structures are of the S-S'-S type, where S' denotes a superconducting region with reduced critical current. Superconducting nanobridges are very suitable structures for practical experiments, because in principle they can be created without having to face the complexities of several deposition, alignment and patterning steps associated with multi–layer thin film devices.

The devices described in this thesis are created in a single Niobium layer using focused ion beam milling. Due to the size and shape of the ion beam, the smallest producible structures still have lengths and widths which are of the order of the superconducting coherence length ($\xi(T) \approx 40$ nm @ $T = 4.2$ K) and the magnetic penetration depth ($\lambda(T) \approx 40$ nm @ $T = 4.2$ K) of Niobium. Because nonlinear effects extend into the electrodes, the effective length (L_{eff}) of these nanobridges is always larger than the geometrical length. Due to diffuse scattering at the surface of the structure, the mean free path (l) in nanobridges is limited to a few hundred Ångstroms, which is smaller than the effective length (dirty limit). To summarize, the superconducting nanobridges described in this chapter and the rest of the thesis can be classified as long ($L_{eff} \geq \xi(T), \lambda(T)$), dirty ($L_{eff} \geq l$) structures.

In the first paragraph of this chapter an overview of theory describing the origin of the current-phase relationship in superconducting nanobridges will be given, followed by a description of the fabrication technique in the next two sections. Simulation and calculation of the damage induced to Niobium structures patterned by means of Gallium focused ion beam milling are also described in this paragraph. The results are used to estimate the actual shapes and sizes of the patterned nanobridges. In the last two paragraphs the electrical characterization of such structures and measurements of the current-phase relationship in different nanobridges are described.

2.1 The current–phase relationship in superconducting nanobridges

One of the fundamental characteristics of superconducting structures is the relationship between the supercurrent through and the phase difference across the structure. The prediction [1] and first experimental verification [2] of periodical current-phase relationships (CPR's) in superconductor – insulator – superconductor tunnel junctions triggered the onset of research on Josephson devices. Much of the classical studies on this subject focused on structures where two superconducting layers are separated by a barrier with a thickness of the order of the superconducting coherence length. With the advances in nanotechnology, also, the development of structures with lateral dimensions of the order of $\xi(T)$ became possible. Examples of such systems are superconducting nanobridges, which, when of sufficiently small dimensions, are known to exhibit a periodical CPR [3,4]. As described before, based on this similarity to classical Josephson tunnel junctions, the development of superconducting quantum interference devices (SQUIDs) incorporating two of such nanobridges has been a topic of ongoing research, e.g. for the detection of the magnetization reversal of small magnetic clusters [5,6,7] and in scanning SQUID microscopes [8,9,10]. The application of superconducting nanobridges as single photon detectors, for instance as described in [11], has been a topic of interest in recent years. In addition, hot electron bolometers based on superconducting nanobridges are expected to be important detectors in astrophysical observations at THz frequencies [12]. Recent fundamental interest in superconducting nanobridges has been motivated by the possible application of such structures in flux qubits [13,14]. Although the experimental confirmation is not yet conclusive, the proposition of such devices is based on the expectation of quantum phase slippage (QPS) in these structures at low temperatures.

Even though applications based on the Josephson-like characteristics of superconducting nanobridges have been investigated extensively, up until now the exact nature of the CPR in these structures has mainly been studied theoretically. In this section an overview of the studies describing the origin of the CPR in superconducting

nanobridges will be given. A complete overview is given in reviews by Likharev [3] and Golubov, Kupriyanov and Il'Ichev [15].

Aslamazov – Larkin Model

The first step towards the theoretical description of the origin of the current–phase relationship in superconducting nanobridges was given in 1969 by Aslamazov and Larkin [16]. The basic principles of the coupling of the order parameters of the electrodes separated by a weak link with strong current concentration were described. Because the derivations are based on the Ginzburg – Landau equations [17], the results are only applicable for temperatures close to the critical temperature ($T \approx T_c$). In this temperature regime the modulus of the superconducting order parameter (Ψ) is relatively small throughout the structure ($|\Psi| << k_b T_c$). Furthermore, the model is limited to short weak links. This means that the effective length of the link is short compared to both the coherence length and the magnetic field penetration depth:

$$L_{eff} << \xi(T), \lambda(T) \tag{2.1}$$

The main result obtained is the "classical" sinusoidal dependence of the supercurrent (I_S) on the phase–difference (φ) of the superconducting order parameters (Ψ_1, Ψ_2) of the two electrodes:

$$I_S(\varphi) = \frac{\pi |\psi_1||\psi_2|}{4eR_N T} \sin(\varphi) \tag{2.2}$$

In this equation R_N denotes the normal state resistance and T the temperature.

Temperature dependent CPR in S- S'- S weak links with finite length

Based on the dirty limit Kulik-Omelyanchuk (KO-1) model [18], which is valid for quasi one dimensional nanowires with lengths $l << (\xi_0 \lambda)^{1/2}$ (where ξ_0 is the BCS coherence length and λ the electronic mean free path) and transverse sizes $a << l$, a gradual temperature dependent deformation of the CPR is expected. This was experimentally verified by determining the CPR in ballistic Nb point contacts, as described in [19]. Likharev and Yakobson first considered the effect of an increasing weak link length on the CPR for structures in which the temperature is close to the critical temperatures of both the electrodes (T_c) and the nanobridge (T_c') [20]. Their model describes a deformation of the CPR from sinusoidal to saw tooth-like as a function of increasing bridge length. Such deformations of the CPR in Indium microbridges were experimentally verified in 1980 by Pei et al. [21].

Furthermore, at a critical length $l >\approx 3.5\ \xi(T)$, with $\xi(T)$ the Ginzburg-Landau (GL) coherence length, the nature of the CPR is predicted to become multi-valued. In this limit superconductivity is suppressed above the critical current by the nucleation of phase slip centers in the structure. Calculation of the critical current (I_0) of the structures revealed that, at first, I_0 decreases with increasing weak link length. Saturation to a constant value occurs for lengths larger than approximately 10 $\xi(T)$. The shape of the CPR changes from single–valued to multi–valued for lengths larger than a critical length (L_c) of approximately 3.5 $\xi(T)$. This variation is shown for different weak link lengths in figure 2 - 1.

The shape of the CPR for S-S'-S weak links with lengths that are larger than the critical length ($L_c \approx 3.5\ \xi(T)$) is approximated by:

$$I_S(\varphi) = \frac{\Phi_0}{2\pi L_k}\left[\varphi - \left(\frac{\xi(T)}{l}\right)^2 \varphi^3\right] \tag{2.3}$$

In this equation, the kinetic inductance of the nanobridge, L_k, is defined by equation 2.4:

$$L_k = \mu_0 \lambda^2 \frac{l}{\sigma} \tag{2.4}$$

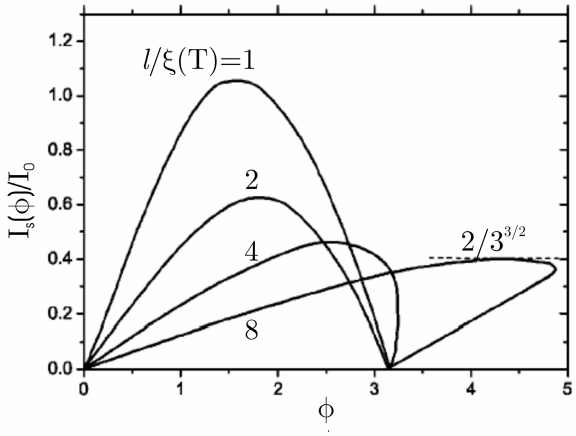

Figure 2 - 1:
The current–phase relationship, calculated for different weak link lengths. This figure was adapted from Likharev and Yakobson [20].

Here l denotes the bridge length and σ its cross-sectional area. Since at $T << T_c$, σ is simply the ratio I_0/J_c, equation 2.4 can alternatively be rewritten as [22]:

$$L_k = \frac{1}{\pi}\left[\frac{\Phi_0 l}{2\pi I_0 \xi(T)}\right] \tag{2.5}$$

Based on this equation it can be estimated that a Nb nanobridge can have a significant kinetic inductance. A 150 nm long bridge, with an I_0 of 10 μA, would have a kinetic inductance of several tens of pH. Application of such structures in a miniature SQUID loop would result in a device where contribution to the total inductance of the kinetic inductances of the nanobridges could well dominate the geometrical inductance of the device. For classical SQUIDs the contributions of the Josephson inductances of the junctions is usually neglected ($L_{jo} << L_{sq}$). For the miniature nanobridge based devices described later in this thesis this is, however, not necessarily the case.

For fixed values of the bridge length and $T_c = T_c'$, the described deformation and cross-over were also predicted as a function of decreasing temperature by Kupriyanov and Lukichev [23]. In terms of the previous model this can be explained by the fact that $\xi(T)$ increases as function of temperature, which, for fixed l, is physically similar to a decrease of the effective bridge length.

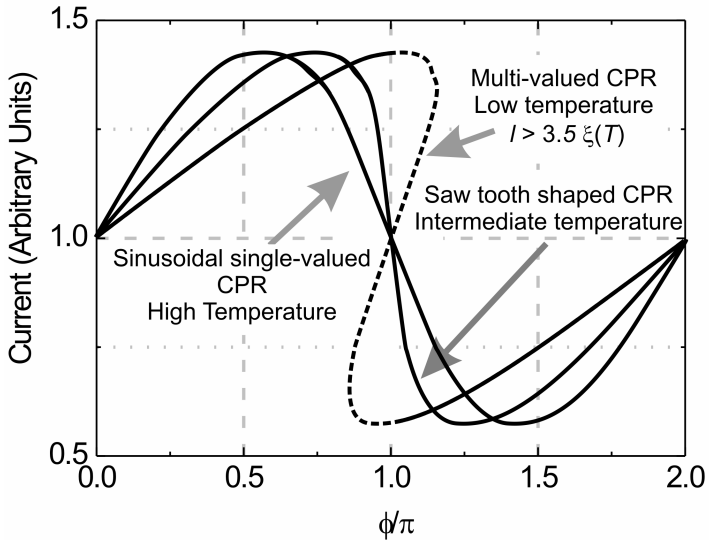

Figure 2 - 2:

Schematic representation of the discussed predicted deformation of the CPR in superconducting nanobridges.

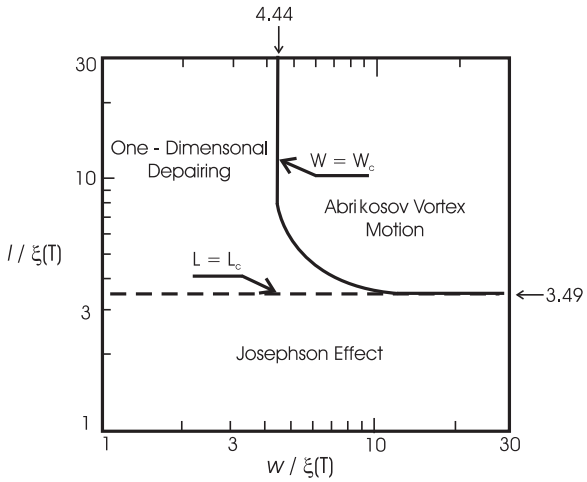

Figure 2 - 3:
The origin of the current–phase relationship in weak links of different dimensions, adapted from Likharev [3].

Based on the models discussed above, the predicted transition of the CPR in a superconducting nanobridge ($l >\approx (\xi_0\lambda)^{1/2}$) is qualitatively depicted in figure 2 - 2. The dotted line corresponds to the sharp drop in phase related to the phase slip mechanism.

S- S'- S weak links with increased width

As described by Likharev [3], the origin of the current–phase relationship in S-S'-S weak links with lengths larger than the critical length ($L_c \approx 3.5\ \xi(T)$) is dependent on the width of the structures. This dependence is shown schematically in figure 2 - 3. From this figure, which is based on numerical simulations, it can be concluded that superconducting nanobridges with lengths smaller than $3.49\ \xi(T)$ ($L_{eff} < 3.49\ \xi(T)$) behave as classical Josephson junctions; i.e. the current–phase relationship is sinusoidal and single-valued. The physical nature of the current phase relationship in longer bridges is dependent on the width of the structures:

- For bridges with widths smaller than $4.44\ \xi(T)$ ($w < 4.44\ \xi(T)$), the CPR is the result of one dimensional (1D) depairing, associated with the nucleation of phase slip centers in the structure.
- In bridges with widths that are larger than $4.44\ \xi(T)$, but smaller than the effective magnetic penetration depth λ_{eff}, ($4.44\ \xi(T) < w < \lambda_{eff}$), the coherent motion of vortices allows the growing phase difference across the

weak link to relax by multiples of 2π, thus preserving long–range order [24].

- Wider bridges are not expected to exhibit coherent vortex motion. No periodic CPR is thus expected.

Superconducting nanobridges in microSQUID geometries

When two superconducting nanobridges are incorporated in a miniature superconducting loop (loop diameter in the order of microns) a microSQUID is formed. As described before, the non–linear effects associated with such nanobridges extend into the electrodes ($l < L_{eff}$). For microSQUIDs this implies that, since the dimensions of the SQUID loop are comparable to the effective nanobridge length, the effects of the nanobridges could influence a significant part of this loop. Based on this assumption Hasselbach, Mailly and Kirtley have modeled microSQUID current–phase relationships by solving the 2D Ginzburg – Landau equations over the entire SQUID geometry [25]. From the numerical simulations discussed in this study it is clear that, when modeling a nanobridge based microSQUID the phase–drop along the whole geometry should be taken into account. In chapter 3 devices for which this description is expected to hold, will be described.

In the rest of this chapter the fabrication and characterization of realized single Niobium nanobridges will be discussed. As discussed in chapter 1, the structures described in this thesis are patterned by focused ion beam milling. Before proceeding to a description of the fabrication of the nanobridges, this patterning technique will shortly be described.

2.2 General aspects of FIB patterning

In contemporary integrated circuit fabrication, photolithography is the key patterning step. Ion beams focused to sub-micrometer diameters offer a radical departure from this technique [26]. Some of the advantages are that resists can be eliminated and that the dose of ions can be varied as a function of the position on the wafer. The obtainable spatial resolution is of the order of the beam diameter. For the research described in this report this means that using an FIB smaller SQUIDs can be fabricated than by using conventional photolithography techniques. The fabrication of thin film devices using an FIB is a serial process. The wafer is exposed point by point, which makes the technique slow and unsuitable for mass industrial production. It is, however, well suited to use in research where only a limited number of samples have to be fabricated. To gain further insight in the focused ion beam patterning technique, a short summary of the interactions of ions with matter is given below. After that the basic setup and principles of an FIB system are described.

Interaction of ions with matter

An incident ion on a substrate loses energy in the following ways:

- Due to Coulomb interaction the passing ion excites electrons into bound or continuum states of the substrate. This is a predictable process.
- On its way through the substrate an ion loses a significant amount of energy in a finite number of collisions with the atoms of the solids. These collisions cause the ions to be deflected from their paths and displace the atoms from their lattice sites. The depth distribution of this damage follows the distribution of implanted ions. If the substrate is irradiated too long or if the ion dose is too high an amorphous layer will be formed.

The ions penetrate to an average depth R_p. Around a depth Z the ion distribution D has the following Gaussian form:

$$D = C \cdot \exp\left(\frac{-(Z - R_p)^2}{2(\Delta R_p)^2}\right) \tag{2.6}$$

In this equation ΔR_p is called the range straggle and C is a constant. In addition to the processes described above an incident ion produces the following changes in the substrate:

- Sputtering: this is the removal of atoms from the substrate due to collisions with the incident ions. The number of atoms removed by each ion, the yield, is typically in the range of 1 to 10 atoms per ion. Sputtered atoms leave the substrate with an energy of a few electronvolts.
- As with the atoms, electrons are also emitted from the substrate. The yield is about the same as for atoms.
- Ion–electron and ion–atom interactions could result in chemical effects that damage the substrate. A simple example of this kind of damage is the change induced in a photoresist molecule after the resist is irradiated.
- Due to the incoming ion beam the substrate is heated (via phonons).

In figure 2 - 4 the basic interactions of the incoming ion beam with the substrate are summarized.

Focused ion beam systems

A focused ion beam system consists of three main parts: an ion source, an ion optics column and a displacement table for the sample. Early FIB systems used a gaseous ion

source. Such a source emits ions from a relatively large area. A desired source though, would emit ions from a single point, preferably into a limited angle. A good approach to this ideal source is the liquid metal field ionization source.

In this kind of source a reservoir of liquid metal is maintained at one end of a sharp Tungsten needle. The metal wets this needle and flows down to the tip, which faces an extraction aperture. A voltage is applied between the tip and the aperture. The electrical field is the strongest at the tip of the needle and the sharper the tip, the higher the field will be. An electric force is exerted on the liquid metal surface, which causes the liquid to be pulled into a sharp cone. From the tip of this cone ions are emitted. The liquid metal can be of any composition. Due to the fact that it is a liquid just above room temperature and that it yields a long lifetime, the most commonly used source is Gallium. The system used to pattern the devices described in this thesis is based on a commercially available Gallium ion source (*FEI type 83-2LI EVA)* [27].

The focusing system of an FIB setup can be compared to a set of optical lenses used to focus a source of light. Instead of the optical lenses, concentric electrostatic lenses are used. These lenses consist of electrodes operated at high potentials. The electric fields generated by these lenses are used to deflect and accelerate the ion beam. This is the principle behind the focusing of the ion beam.

Due to the statistical nature of the ion emission and the mutual electrostatic repulsion between ions, there is a spread in the energy of the ions emitted by the source. This energy spread, ΔE, poses one of the main problems for the focusing system: chromatic aberration. This effect would cause a beam of zero radius to have a diameter given by:

$$d = C_c \alpha \left(\Delta E / E \right) \tag{2.7}$$

In this equation C_c is the chromatic aberration coefficient, α is the half angle of the beam arriving at the final focal spot of the lens and E is the total beam energy.

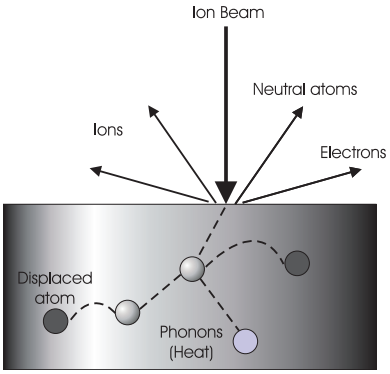

Figure 2 - 4:
Summary of the interaction of ions with matter.

From the description given above it should be clear that chromatic aberration poses a limit to the diameter of the ion beam.

Another problem arises due to spherical aberration: the focal length of a lens is dependent on the distance of the ion path from the main axis. Although not as big a problem as the chromatic aberration, it does contribute to the finite beam diameter. The total beam diameter is thus limited by the finite source size, chromatic aberration and spherical aberration. The beam diameter in the used FIB system was approximately 150 nm. The non–homogeneous ion distribution profile in this beam has a full width at half maximum of approximately 50 nm. As will be described in the next section, this inhomogeneity is used to create structures with effective widths that are smaller than the ion beam diameter.

As described above, the dimensions of devices produced by focused ion beam patterning are limited. Summarizing, these limitations are the results of:

- The modifications of the sample matter (apart from the sputtering itself). In a patterned structure there will be a thin layer of film that is damaged. The source of damage extending furthest inwards from the surface is the implantation of ions.
- The finite diameter of the ion beam. The spatial resolution of the FIB patterning technique is limited by the size and shape of the beam.

In the next section simulations and experiments determining the extent of the damaged region in patterned Nb striplines will be described.

2.3 Niobium nanobridges - fabrication

In this section the fabrication aspects related to the FIB patterning of Niobium nanobridges are described. Firstly, an overview is given of the photolithography based patterning of Niobium striplines, which are predefined in sputtered films before FIB milling. After this, the applied patterning technique is discussed, followed by a description of simulated and measured estimates of the Ga^+ ion induced damage in FIB patterned Nb structures.

Preparation of prestructured Niobium films

The Niobium thin films, in which the nanobridges described in this chapter are patterned, are sputtered on oxidized Silicon wafers. This oxide grows easily on any Silicon layer via inward diffusion of the oxidant and is electrically insulating (which makes the production of devices in a film on top of it possible). The layer is amorphous,

which takes away the risk of having large stresses in the Niobium film. Two-inch, oxidized, Silicon wafers were used to prepare the Niobium layers.

In order to structure the nanobridges using the focused ion beam system, the Nb layers have to be prestructured. This was done using standard photolithography with lift-off. First a layer of photoresist (40 nm of Olin 907-12, spun for 40 seconds at 4000 turns per minute) was spun onto the SiO_2 wafer. The photoresist was then baked at 95 degrees centigrade for 2 minutes before exposure (4 seconds). After exposure the samples were baked at 120 degrees centigrade for two minutes. Development (120 seconds) in OPD 4262 photoresist developer yields the eventual photoresist structure. On top of this photoresist structure the Nb layers were grown by means of DC sputtering in an Argon background. Removing the leftover resist in Acetone reveals the eventual Niobium structure. The lithography process is schematically summarized in figure 2 - 5. All the structures described in this chapter are patterned in 50 nm thick Niobium layers.

Nanobridge patterning

All the Niobium nanobridges described in this thesis were patterned by means of FIB in striplines of 50 nm thicknesses and 5 μm widths. All devices are patterned with 25 keV Ga^+ ions.

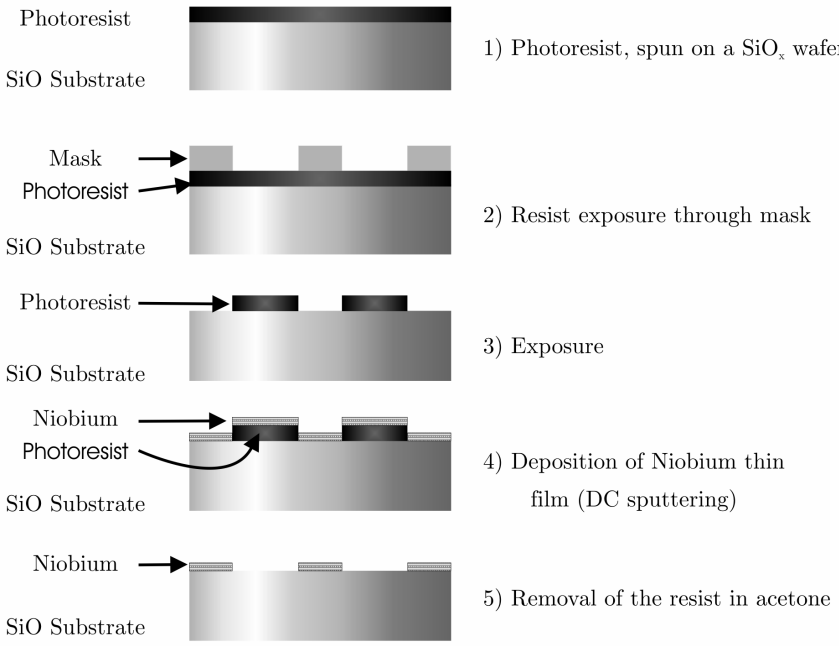

Figure 2 - 5:
Step by step summary of the photolitography process.

As was described before, when designing the Nb nanobridges the non–uniformity in the shape of the FIB ion distribution profile and the damage induced to the patterned structures by the high energy Ga ions should be taken into account. The ion distribution of the FIB beam has a Gaussian shape with tails. The full width at half maximum (FWHM) is approximately 50 nanometers and the base–width 150 nanometers. In practice, this means that patterned devices will have rounded edges with typical dimensions of 100 nm.

The patterning of the nanobridges is based on a technique developed by Blank et al. [28]. By letting two beam profiles overlap, as shown in figure 2 - 6, structures with effective widths smaller than the FIB beam diameter can be created. As was described in the previous section, when patterning structures by means of FIB milling, also changes in properties of the structured sample areas resulting from the Ga^+ ion induced damage should be taken into account. The determination of the possible effects of this type of damage on the superconducting properties of patterned Nb structures will be discussed next.

Ga ion induced damage on Nb structures during FIB patterning

From previous studies it is known that the superconducting properties of Nb are suppressed by the implantation of Kr [29] and N [30] into interstitial lattice sites. To evaluate the extent to which Ga implantation affects the properties of patterned devices, calculations were performed using SRIM, which is designed to calculate the Stopping and Range of Ions in Matter. The simulations performed with SRIM are based on a quantum mechanical treatment of ion–atom collisions using statistical algorithms. These algorithms allow the ion to make jumps between collisions and then calculate the average collision results over the intervening gap.

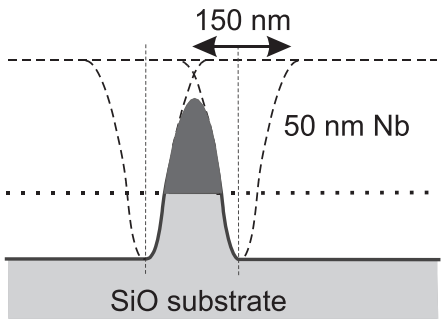

Figure 2 - 6:
By letting 2 beam profiles overlap, superconducting bridges with widths smaller than the FIB diameter can be produced.

During these collisions, the ion and atom have a screened Coulomb interaction, including exchange and correlation interactions between the overlapping electron shells. Long - range interactions have been taken into account by the excitations of electrons and the creation of plasmons in the target, using its collective electronic and interatomic bond structure. A full comprehension of the theory is not necessary to use the program and obtain estimates of ion implantation depths. For further information about the program reference is made to Ziegler et al. [31].

Simulation of the impact of 10^4 Ga ions, with 25 keV energies, at normal incidence to a 50 nm Nb layer, revealed that the average implantation depth is 10 to 15 nm inwards from the surface of the film; 2.5% of the ions reach depths of 25 nm and 0.4% is implanted as far as 30 nm inwards from the surface of the structure. These results are summarized in figure 2 - 7.

To experimentally determine the effect of the Ga–implantation on a patterned Nb device, trenches of different depths were milled in a prestructured Nb stripline of 50 nm thickness. This allows for a systematic variation of the remaining Nb height (h), as is shown in figure 2 - 8 (A). From the dependence of the resistance versus h in part (B) of this figure, it can be concluded that, at $T = 4.2$ K, superconductivity is suppressed as far as 30 nm or more inwards from the surface. This corresponds to the calculated implantation depth of 30 nm.

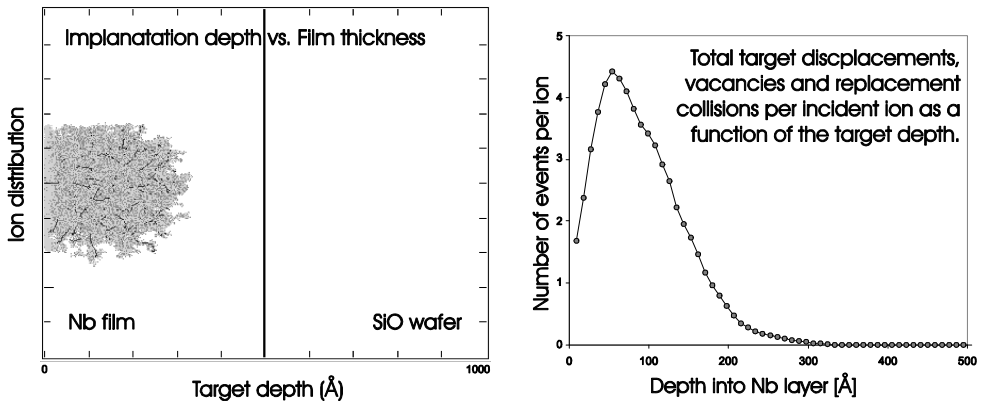

A B

Figure 2 - 7:

(A) Distribution profile of the implanted Gallium ions during FIB patterning as a function of the Nb film depth.

(B) A plot of the total target displacements, vacancies and replacement collisions as a function of target depth.

Calculation parameters: 1000 ions: Ga^+, 25 keV, normal incidence.

Combined with the prediction that only 0.4% of the ions reach this far into the structure, the known FIB beam current and corresponding Nb etching rate (41 pA and 6.7 x 10^{-3} $\mu m^3/s$), the ion-atom implantation ratio can be computed. Based on such calculations, an implantation of roughly 1.1 x 10^7 Ga ions into the bottom 5 nm of a patterned 1 x 5 μm^2 wide trench (which equals 1.6 x 10^9 Nb atoms) is enough to suppress the superconducting properties of the structure at $T = 4.2$ K. This corresponds to an implantation ratio of approximately 0.7%, which is of the same order of magnitude as the reported values for Kr (0.2 – 2%) and N (0.5 – 5%).

Given the results described in this section, the effective width at $T = 4.2$ K of patterned Nb nanobridges is defined as shown in figure 2 - 9. The length of the bridges corresponds to the ion beam diameter of 150 nm. In the next section the electronic characterization of patterned nanobridges will be described. In the final section of the chapter measurements of the current-phase relationships of two different bridges will be discussed.

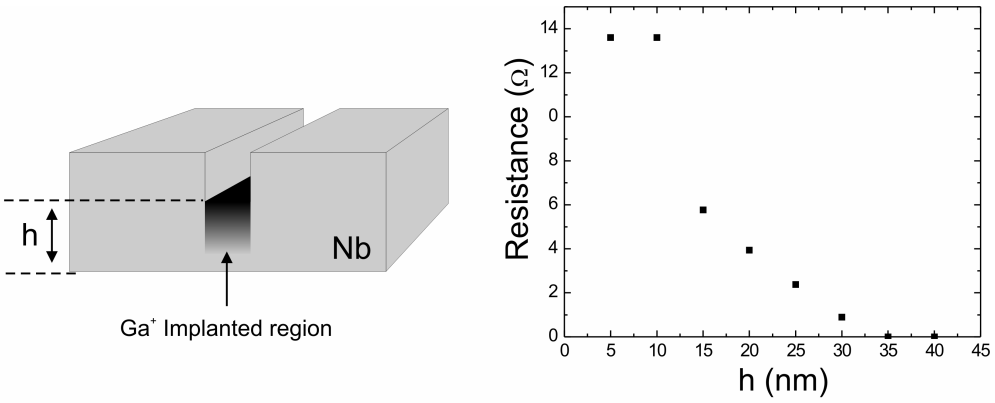

A B

Figure 2 - 8:
(A) Schematic layout of the patterned trenches in a Nb stripline of 50 nm thickness.
(B) Measured resistance as a function of the leftover height h.
From this figure it can be concluded that the transition from resistive to superconducting structures occurs for remaining heights of 30 - 35 nm.

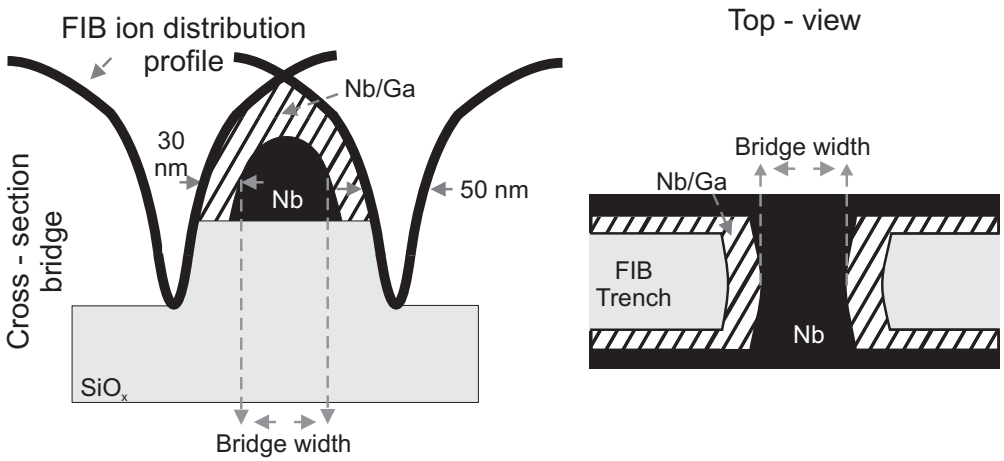

Figure 2 - 9:
The width of a patterned Nb nanobridge is defined as the FWHM of the expected superconducting structure. In this definition the Ga^+ implantation depth is taken to be 30 nm.

2.4 Niobium nanobridges – electronic properties

In this section, measurements on Niobium nanobridges patterned by means of focused ion beam milling in 50 nanometer thick films are described. In the next section measurements of the current–phase relation of the described structures will be presented.

Single layer Niobium nanobridges

In figure 2 - 10 a scanning electron micrograph is depicted of a 50 nm wide Niobium nanobridge, patterned in a predefined 50 nm thick, 50 μm wide, lead. The critical current at $T = 4.2$ K of this device was measured to be 9.2 μA. The measured IV characteristic at this temperature corresponding to this device is shown in figure 2 - 11 (A), together with characteristics belonging to 3 other structures with different designed widths. As showcased in this graph, for devices with larger critical currents an onset of hysteresis in the measured IV characteristic can be noted. This is believed to be caused by thermal effects [32] and will be further discussed in the final section of this chapter.

In figure 2 - 11 (B) the measured critical currents at $T = 4.2$ K of several nanobridges with different designed widths are shown. From this figure it appears that there is an almost linear relationship between the critical current of a nanobridge and its designed width. For most realized samples, however, this does not appear to be the case. As will be shown in the next chapter when the characteristics of nanobridge based SQUIDs are discussed, based on the designed bridge–width, the predictability of characteristics such as the device critical current is limited.

In figure 2 - 12 (A) the IV characteristic of an 80 nm wide nanobridge with a critical current of approximately 256 μA is shown. In part (B) the derivative of this curve ($\delta I/\delta V$) with respect to the voltage is shown. Two distinct peaks can be noticed, located at voltages of approximately ± 1.8 mV. From BCS theory it is known that these peaks are expected to occur at ± $2\Delta(T)$, with $\Delta(T)$ being the temperature dependent superconducting energy gap. The expected gap voltage at $T = 4.2$ K, for Nb with $T_c = 9$ K, is approximately 1.4 mV.

Since the energy gap of a superconductor is expected to scale with T_c ($\Delta(0) \approx 7/2\ k_b\ T_c$) it can be estimated that for the case depicted in figure 2 - 11, the superconducting region surrounding the nanobridge has a degraded T_c of approximately 6.4 K. From figure 2 - 13 it can be concluded that this is a realistic value for T_c. In this graph a comparison of the bridge and film critical temperatures is given. A clear difference between the two can be noted: $T_{c\_film} \approx 9.3$ K, $T_{c\_bridge} \approx 6.8$ K.

From literature it is known that superconducting nanowires have reduced critical temperatures [33]. Together with a decrease in T_c which can be accounted for by Ga^+ degradation related effects, the difference between the measured film and bridge T_c can be explained. The larger resistance drop, which occurs at approximately $T \approx 7.5$ K, is probably attributable to the degraded banks of the microbridge.

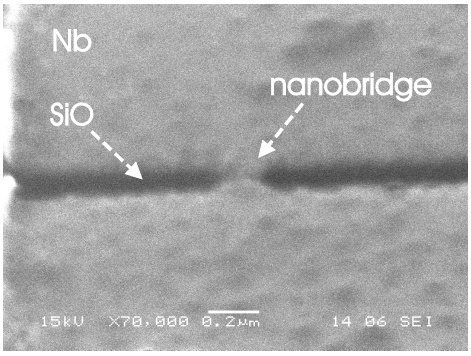

Figure 2 - 10:
Scanning electron micrograph of a nanobridge with a designed width of 50 nanometers.

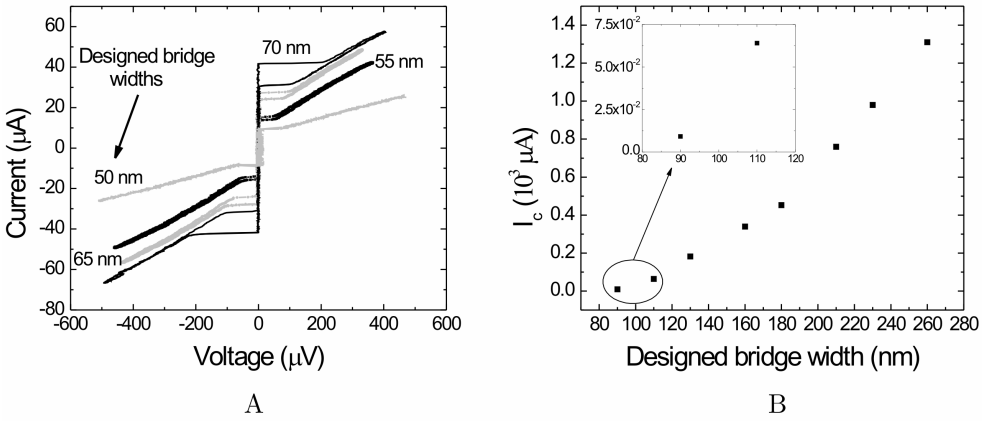

Figure 2 - 11:

(A) Current–voltage (IV) characteristic of 4 nanobridges with different designed widths. The 50 nm characteristic corresponds to the device shown in figure 2 - 10.

(B) Measured critical currents of nanobridges with different widths.

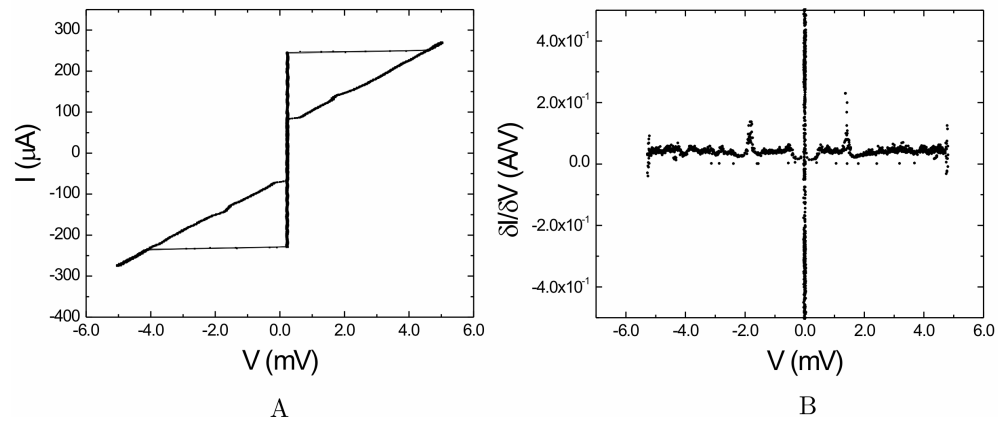

Figure 2 - 12:

(A) IV characteristic of an 80 nm wide Nb nanobridge with an I_0 of 256 μA.

(B) dI/dV vs. V curve of the IV characteristic shown in part (A), exhibiting peaks corresponding to the superconducting energy gap.

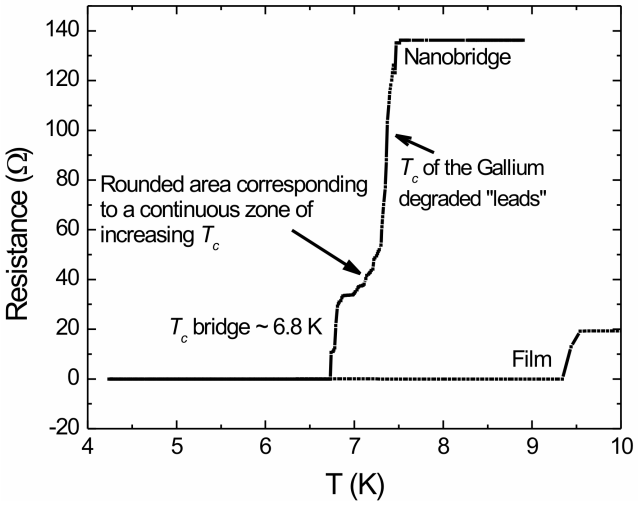

Figure 2 - 13:
Comparison of the critical temperatures of a Nb film and a nanobridge with a width of 190 nm patterned in a prestructured stripline in this film. The bridge T_c is determined by the narrowest and most degraded part.

Both aforementioned regions are connected via a "rounded" tail in the R-T characteristic, which results from the contributions of areas with increasingly reduced critical temperatures. Another possible explanation for the "rounded" region in the characteristic is the thermal activation of flux flow in the structure.

For measurements at low temperatures ($T << T_c$) distinct features are expected to appear in the IV characteristic at voltages below the gap voltage. In literature several reports have been made about these "subharmonic gap structures" [34,35,36,37,38,39,40,41]. A commonly found explanation for such measurements is that the subharmonic gap structure is the result of multiple Andreev reflection in the micro–constriction separating two superconducting electrodes [42]. Given the fact that all the described experiments were conducted at $T = 4.2$ K, which corresponds to $T/T_c \approx 0.5$, no such features were detected.

In the next section of this chapter experiments aimed towards the determination of the current–phase relationship in patterned Niobium nanobridges are described. Even though a thorough understanding of the current–phase relationship is not necessary when making SQUIDs, valuable insights in the properties of realized devices can be gained from such experiments.

2.5 Measurements of the current–phase relationship (CPR)

Measurements of the current–phase relationship were performed on Niobium nanobridges of different widths at the Institute of Photonic Technology (IPHT) in Jena, Germany. Before discussing the results, the method of measurement, described by Golubov et al. [4], will be briefly reviewed.

Experimental method

The CPR measurements are based on a method where the weak link of interest is incorporated in a superconducting ring of sufficiently small inductance (L). The flux through this ring (Φ_i) as a result of an applied flux (Φ_{ext}), is given by:

$$\Phi_i = \Phi_{ext} - IL \tag{2.8}$$

, with I being the current through the loop. The phase–difference (φ) across the weak link can than be described by:

$$\varphi = 2\pi \frac{\Phi_i}{\Phi_0} + 2\pi n \tag{2.9}$$

Assuming that the superconducting part of the current (I_s) is a lot larger than any other contribution and combining both equations gives:

$$\varphi = \frac{2\pi\Phi_{appl}}{\Phi_0} - \frac{2\pi L I_s(\varphi)}{\Phi_0} = \frac{2\pi\Phi_{appl}}{\Phi_0} - \beta f(\varphi) \tag{2.10}$$

Here β and $f(\varphi)$ are defined as follows:

$$\beta = \frac{2\pi L I_0}{\Phi_0}; \quad I_s(\varphi) = I_0 f(\varphi) \tag{2.11}$$

The measurement of the current–phase relationship is based on a radiofrequency technique developed by Silver and Zimmerman [43]. The superconducting loop containing the weak link is connected to a tank circuit with inductance L_T and quality factor Q, driven by a DC bias current (I_{dc}) and an rf current (I_{rf}) close to its resonance frequency, through a mutual inductance (M). The experiments are based on the measurement of the phase angle (α) between the tank circuit voltage (U) and driving current (I_{rf}). If the

measurements are conducted at the resonance frequency of the tank circuit (ω_0) and if $\omega_0 L/R_N << 1$ (R_N is the junction normal state resistance), the relationship between the measured phase angle and the CPR can be expressed as follows [44,45,46]:

$$\tan\alpha = \frac{M^2 Q}{LL_T}\frac{\beta f'(\varphi)}{1+\beta f'(\varphi)} \tag{2.12}$$

In the limit of small $\beta f'(\varphi)$, this reduces to:

$$\tan\alpha = \frac{M^2 Q}{LL_T}\beta f'(\varphi) \tag{2.13}$$

The described measurement method is schematically summarized in figure 2 - 14. In figure 2 - 15 a scanning electron micrograph showing the different sample components is displayed.

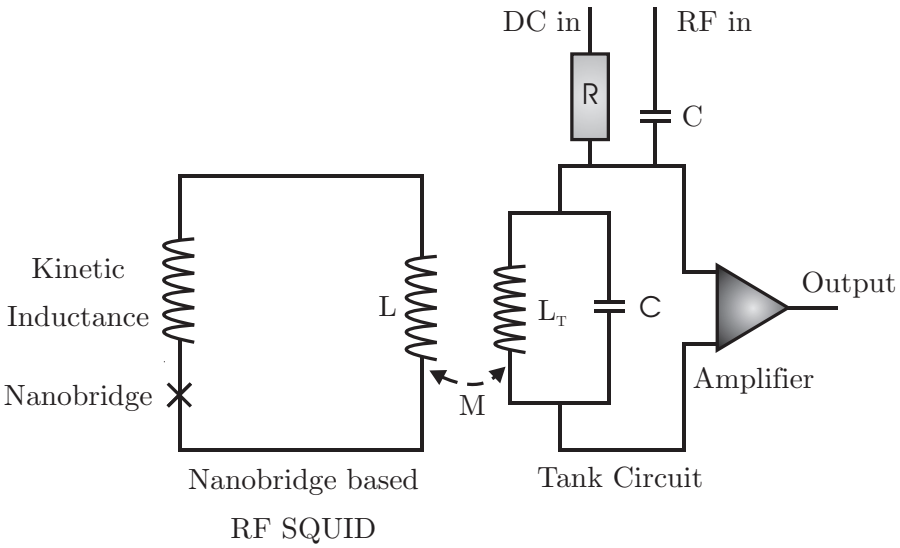

Figure 2 - 14:

Schematic representation of the discussed current-phase measurement technique.

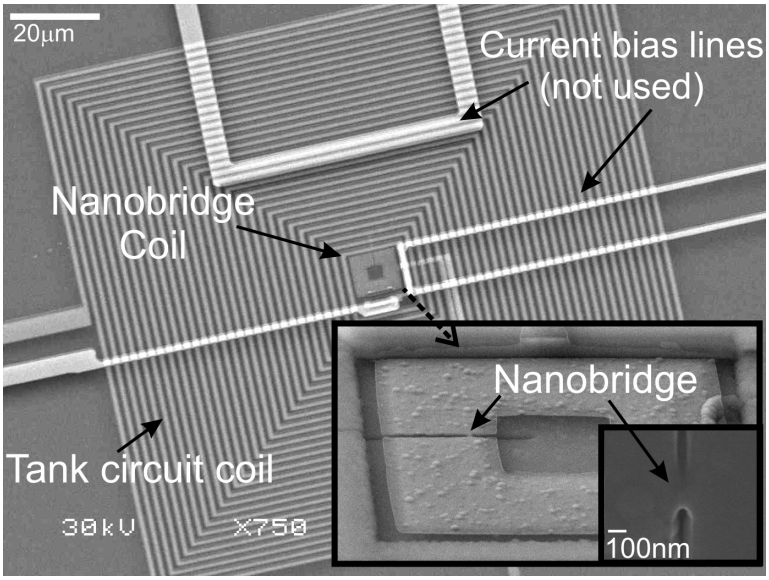

Figure 2 - 15:
Scanning electron micrograph of a sample for CPR measurements on a Nb nanobridge.

Results

Temperature dependent measurements of the phase angle (α) as a function of the DC current through the tank circuit (I_{dc}), were performed on two samples based on bridges with different widths (60 and 30 nm respectively). In the literature a cross-over from the 1D-depairing to the Josephson regime with increasing temperatures for fixed bridge lengths is predicted on the basis of numerical simulations [23].

In figure 2 - 16 the main obtained experimental results are summarized (curves have been given different vertical off-sets for clarity). Parts (A) and (B) show measured $\alpha - I_{dc}$ curves for different temperatures for the sample incorporating the 60 nm wide bridge. At low temperatures ($T < 4.9$ K) discrete jumps in the $\alpha - I_{dc}$ curves can be discerned. These originate from the fact that, due to phase – slippage, the CPR jumps to the next period before the previous one is completed. A cross-over to a single-valued regime, which corresponds to $\alpha - I_{dc}$ curves without discontinuities in the derivative ($\delta\alpha/\delta I_{dc}$ is continuous, i.e. there are no jumps in the measured $\alpha - I_{dc}$ curve), can be noted around $T = 4.9$ K. Further increase in temperature results in sine-like dependencies.

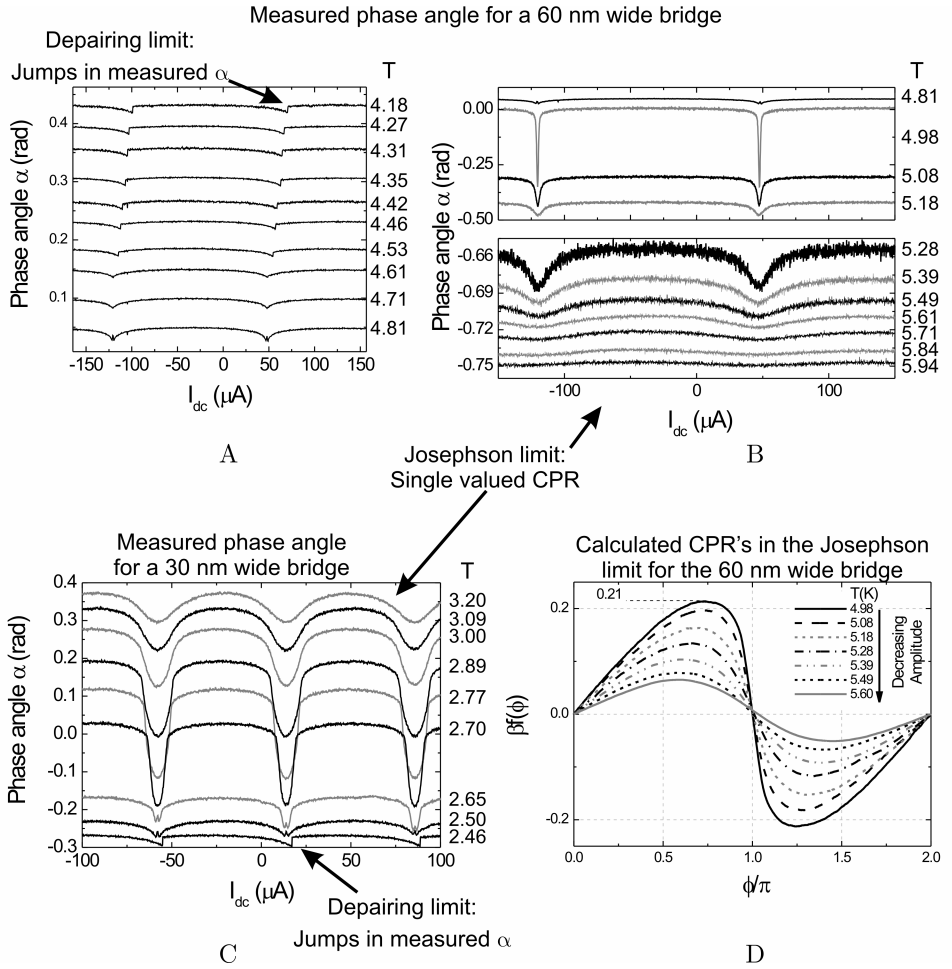

Figure 2 - 16:

(A) Measured $\alpha - I_{dc}$ curves corresponding to multi-valued CPR's for different temperatures for a 60 nm wide bridge. A cross-over from multi- to single-valued characteristics occurs around $T = 4.9$ K (part (B)).

(B) $\alpha - I_{dc}$ dependencies at higher temperatures for the 60 nm bridge (part (A)).

(C) Measured $\alpha - I_{dc}$ characteristics for a 30 nm wide bridge.

(D) Calculated CPR's corresponding to the single-valued curves shown in part (A).

Similar characteristics have been measured for a 30 nm wide bridge, as is shown in figure 2 - 16 (C). This structure appeared be in the Josephson limit at $T = 4.2$ K. Reduction of the temperature to $T = 2.65$ K induced the cross-over to 1D-deparing characteristics.

Apart from the fact that the characteristics are plotted on a different scale, the main reasons that the dips in the $\alpha - I_{dc}$ curves are wider and less deep than was the case for the 60 nm wide bridge, are that during measurements, the RF component of the current through the tank circuit was larger and the number of collected data points was lower. Still, however, a qualitative analysis of the transition from 1D-depairing to Josephson-like current-phase characteristics is warranted. It is assumed that due to the limited width of the superconducting structures (in the order of 30-80 nm), the CPR in the multi-valued regime is determined by phase slippage of the order parameter rather than the coherent motion of vortices across the structure. For the single-valued $\alpha - I_{dc}$ curves shown in figure 2 - 16 (A), calculation of the CPR ($\beta f(\varphi)$) is possible. The results of such calculations for the characteristics shown in part (A), are depicted in part (D) of figure 2 - 16.

A clear temperature dependent deformation of the calculated CPR's can be noted. At higher temperatures the determined $\beta f(\varphi)$ curves exhibit increasing deformations from sinusoidal features. The sharpest measured transition from maximum to minimum was observed at $T = 4.98$ K. Further decrease in temperature resulted in jumps in the $\alpha - I_{dc}$ curves, which in turn corresponds to a situation where the minimum is reached at a lower value of φ/π than the maximum. This situation, reminiscent of phase slippage of the superconducting order parameter, was schematically introduced in figure 2 - 2.

For the determined single-valued CPR with the lowest temperature ($T = 4.98$ K), a maximum value for $\beta f(\varphi)$ of approximately 0.21 was calculated. Based on equation 2.11, this corresponds to a critical current of the nanobridge of about 12 μA. A similar analysis can be conducted for the characteristics of the 30 nm wide bridge shown in figure 2 - 16 (B). The calculated CPR's in the Josephson limit for the latter structure are shown in figure 2 - 17. As was discussed before, the data does not incorporate the full dip in the $\alpha - I_{dc}$ curves. As a consequence of these measurement non-idealities, the derivatives of the determined CPR's appear to be discontinuous near the extremities of the curves. Still, around the transition temperature $T = 2.65$ K, a maximum value of $\beta f(\varphi) \approx 0.31$ can be determined. From this a maximum value of the critical current of approximately 12 μA can be calculated. Within the given experimental uncertainties, this value is comparable to the one found for the 60 nm wide bridge. The difference in the maximum value of $\beta f(\varphi)$ can be explained by the fact that the loop inductances of the RF SQUIDs had significantly different values (8.3 pH (60 nm) and 5.4 pH (30 nm)).

Discussion

In the preceding parts of this section temperature dependent CPR measurements on two Niobium nanobridges with different widths were presented. For both structures a transition from the 1D-depairing to the Josephson limit was determined with increasing

temperatures. In terms of the theory described in section 2.1, this transition can be explained by the fact that the coherence length is strongly dependent on temperature.

In the dirty limit and near $T = T_c$, the Ginzburg – Landau coherence length $\xi(T)$ varies with temperature as follows [4]:

$$\xi(T) \propto (1 - T/T_c)^{-1/2} \tag{2.14}$$

An increase in temperature thus corresponds to a larger value of $\xi(T)$. This in turn can be seen as a decrease of the effective bridge length. Based on this, a systematic increase of the temperature corresponds to a systematic decrease of the effective length of a nanobridge. From figure 2 - 1 it can be concluded that a transition from the phase-slippage to the Josephson-like regime is expected for increasing nanobridge effective lengths (corresponding to decreasing temperatures), which qualitatively describes the measured characteristics.

CPR measurements at $T = 4.2$ K revealed that the 60 nm wide bridge was in the 1D-depairing limit and the 30 nm wide structure in the Josephson-like limit. Geometrically, however, both structures are of the same length, since this dimension is simply determined by the diameter of the ion beam. Apart from the fact that, as described in section 2.4, the wider structure is expected to have a larger T_c, and thus a smaller $\xi(T)$ at $T = 4.2$ K [33], a possible explanation for the determined difference in the natures of the CPR's lies in the fact that the patterned nanobridges have a hyperbolic shape. For such structures the effective length, which can be significantly larger than the geometrical length, is dependent on the width of the bridge.

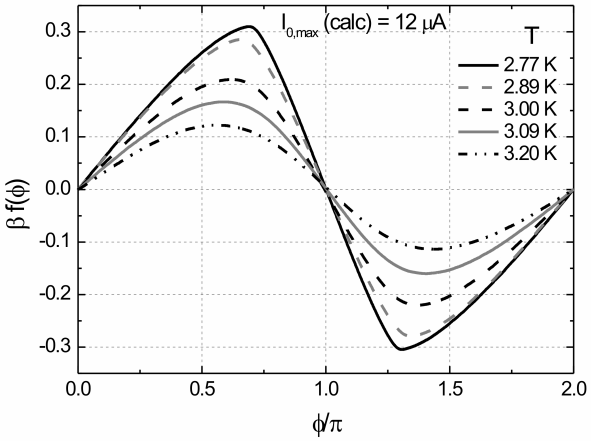

Figure 2 - 17:
Calculated CPR's for the 30 nm bridge shown in figure 2 - 16(C).

The relative effective length of the nanobridges, determined by the relation of L_{eff} to $\xi(T)$, can thus differ significantly from one structure to the other. Another notable result is the fact that the cross-over from 1D depairing to Josephson-like characteristics occurs when both investigated structures have a comparable critical current ($I_0 \approx 12$ μA). This could be explained by the fact that I_c is merely a function of the relative dimensions of the structure; i.e. the cross-over is expected for similar values of $L_{eff}/\xi(T)$, which yields identical values for I_c.

For both structures I_c was determined as the maximum current at the point of transition from single- to multi-valued CPRs. If the walls of the bridge are ideal it can be expected that superconductivity in the structure is destroyed by supercurrent induced depairing effects. To test this suggestion the experimental data was plotted in units of $eI_s(\varphi)R_N/2\pi k_b T_c$ (with e the elementary charge ≈ 1.602 x 10^{-19} C) together with the theoretical curves calculated in [23]. The results of this comparison are shown in figure 2 - 18. From this figure it can be concluded that there is good qualitative agreement in the shapes of the curves. To obtain quantitative agreement, a value of R_N of more than an order of magnitude larger than typically measured values was used. A suggested explanation for this is that the destruction of superconductivity in the structure occurs due to the penetration of Abrikosov vortices in the bridge rather than by depairing by a bias current.

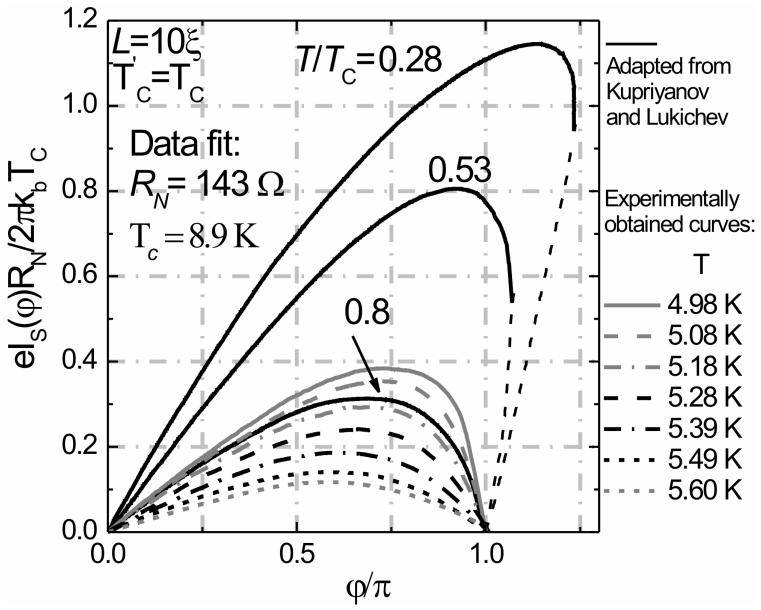

Figure 2 - 18:

Experimentally determined CPR's in units of $eI_s(\phi)R_N/2\pi k_b T_c$ and calculated CPR's for a bridge with length L = 10 ξ and $T_c' = T_c$. The data was fitted with the following parameters: R_N = 143 Ω and T_c = 8.9 K.

This mechanism of destruction is achieved at smaller supercurrent densities and, like in ordinary superconducting films, is not dependent on the length of the structure but on the probability of vortex nucleation in an in-homogeneity in the sidewalls of the bridge. This could thus be another explanation for the similarity of the critical currents near the cross-over.

The current-voltage (IV) characteristics of superconducting nanobridges exhibiting 1D depairing are known to be hysteretic. Apart from a small intrinsic contribution to the total hysteresis in the IV-characteristics [47], this effect is mainly attributed to local heating by the hot-spot associated with a phase slip center [48,49]. In the next chapter the characteristics of DC SQUIDs based on Niobium nanobridges are presented. For such devices this would imply that, in order to operate the SQUID in a conventional current-biased fashion (which is only possible when there is no hysteresis in the IV characteristic), the nature of the CPR of the nanobridges should be single-valued. From the measurements presented in this section this limits the critical currents of such devices to below $\approx$ 2 x 12 μA = 24 μA (provided both bridges are identical).

2.6 Summary

Superconducting nanobridges, which are a type of Josephson weak link, were discussed in this chapter. Firstly, based on the literature, theory describing the origin of the current–phase relationships (CPR) in these types of structures was discussed. The expected characteristics of the CPR are dependent on the dimensions of the structures. The fabrication of the described Niobium nanobridges is based on Gallium focused ion beam milling. It has been proven that, due to implantation of Gallium ions into patterned Niobium structures, superconductivity is suppressed as far as 30 nm inwards from the surface. Based on this result a model for the dimensions of the realized Niobium nanobridges was presented. In the fourth section of the chapter some electrical characteristics of realized structures were presented.

CPR measurements performed on two different Niobium nanobridges were described in the last section of the chapter. The temperature induced cross-over from the 1D depairing to the Josephson limit was observed for both structures. The critical current of both structures near this transition was comparable ($\approx$ 12 μA). For SQUIDs based on similar nanobridges, such as the ones described in the next chapter, this implies that, in order to obtain non-hysteretic current-voltage characteristics, the device critical current is limited to approximately 24 μA.

Bibliography

[1] **B.D. Josephson**; Phys. Lett. **1**, 251 (1962)

[2] **W. Anderson and J.M. Rowell;** Phys. Rev. Lett. 10, 230 (1963)

[3] **K.K. Likharev;** Rev. Mod. Phys. **51**, 101 (1979)

[4] **A.A. Golubov, M.Yu. Kupriyanov, and E. Il'Ichev;** Rev. Mod. Phys. 76, 411 (2004)

[5] **M. Jamet, W. Wernsdorfer, C. Thirion, D. Mailly, V. Dupius, P. Melinon and A. Perez**; Phys. Rev. Lett. 86, 4676 (2000)

[6] **J. Gallop**, **P.W. Joseph – Franks, J. Davies, L. Hao and J. MacFarlane**; Phys. C. 368, 109 (2002)

[7] **S.K.H. Lam and D.L. Tilbrook**; Appl. Phys. Leyy. 82, 1079 (2003)

[8] **J. Dechert, K. Krischker, T. Goddenhenrich, M. Much and C. Heiden**; IEEE Trans. Appl. Supercon. 7, 1051 (1997)

[9] **C. Veauvy, K. Hasselbach, and D. Mailly;** Rev. Sci. Instrum. 73, 3825 (2002)

[10] **K. Chen, P. Magnelind, P. Larsson, A.Ya. Tzalenchuk and Z.G. Ivanov**; Phys. C 372-376, 63 (2002)

[11] **G.N. Gol'tsman, O. Okunev, G. Chulkova, A. Lipatov, A. Semenov, K. Smirnov, B. Voronov, A. Dzardanov, C. Williams and R. Sobolewskib**; Appl. Phys. Lett. 79, 705 (2001)

[12] **D.E. Prober**; Appl. Phys. Lett. 62, 17 (1993)

[13] **J.E. Mooij and C.J.P.M. Hermans**; New. J. Phys. **7**, 219 (2005)

[14] **J.E. Mooij and Yu.V. Nazarov**; Nat. Phys. **2**, 169 (2006)

[15] **A.A. Golubov, M.Y. Kupriyanov & E. Il'Ichev**; Rev. Mod. Phys. 76, 411 (2004)

[16] **L.G. Aslamazov and A.I. Larkin**; JETP Lett. 9, 87 (1969)

[17] **V.L. Ginzburg and L.D. Landau**; Zh. Eksp. Theor. Fiz. 20, 1064 (1950)

[18] **I.O. Kulik and A.N. Omelyanchuk**; Pis'ma Zh. Eksp. Teor. Fiz. 21, 216 (1975) [JETP Lett. 21, 96 (1975)]

[19] **M.C. Koops, G.V. van Duyneveldt and R. De Bruyn Ouboter**; Phys. Rev. Lett. 77, 2542 (1996)

[20] **K.K. Likharev and L.A. Yakobson**; Zh. Tekhn. Fiz. 45, 1503 (1975) [Sov. Phys.Tech. Phys. 20, 950 (1975)]

[21] **S.S. Pei, J.E. Lukens and R.D. Lukens**; Appl. Phys. Lett. 36, 88 (1980).

[22] **A.M. Kadin**; Introduction to Superconducting Circuits; John Wiley & Sons, NY USA (1999)

[23] **M.Yu. Kupriyanov and V.F. Lukichev**; Fiz. Nizk. Temp. 7, 281 (1981) [Sov. J. Low Temp. Phys. 7, 137 (1981)

[24] **P.W. Anderson and A.H. Dayem**; Phys. Rev. Lett. 13, 195 (1964)

[25] **K. Hasselbach, D. Mailly and J.R. Kirtley**, J. Appl. Phys. 91, 4432 (2002)

[26] **J. Mengalis**; Focused ion beam technology and applications; Jour. Vac. Sci. Technol. B 5, 2 (1987)

[27] FEI Instruction manual; FEI company; Beaverton OR; USA (1993)

[28] **D.H.A. Blank, W. Booij, H. Hilgenkamp, B. Vulink, D. Veldhuis and H. Rogalla**; IEEE Trans. Appl. Supercond. 5, 2786 (1995)

[29] **G. Heim and E. Kay**; Jour. Appl. Phys. 46, 4006 (1975)

[30] **C. Camerlingo, P. Scardi, C. Tosello and R. Vaglio**; Phys. Rev. B. 31, 3121 (1985)

[31] **J.F. Ziegler, J.P. Biersack and U. Littmark**,; The stopping and range of ions in solids" Pergamon Press, New York, (1985)

[32] **K. Hasselbach, D. Mailly and J.R. Kirtley**; Jour. Appl. Phys. 91, 4431 (2002)

[33] **C.N. Lau, M. Markovic, M. Bockrath, A. Bezryadin and M. Tinkham**; PRL 97, 217003-1 (2001)

[34] **B.N. Taylor and E. Burstein**; Phys. Rev. Lett. 10, 14 (1963)

[35] **C.J. Adkins**; Rev. Mod. Phys. 36, 211 (1964)

[36] **O. Hoffman Soerensen, B. Kofoed, N.F. Pedersen and S. Shapiro**; Rev. de Phys. Appl. 9, 153 (1974)

[37] **M. Octavio, W.J. Skocpol and M. Tinkham**; IEEE Trans. MAG-13, 739 (1977)

[38] **J.M. Rowell**; Rev. Mod. Phys. 36, 215 (1963)

[39] **D.G. McDonald, E.G. Johnson and R.E. Harris**; Phys. Rev. B13, 1028 (1976)

[40] **P.E. Gregers – Hansen, E. Hendricks, M.T. Levinsen and G.R. Pickett**; Phys. Rev. Lett. 31, 524 (1973)

[41] **J.M. Rowell and W.L. Feldmann**; Phys. Rev. 172, 393 (1968)

[42] **T.M. Klapwijk, G.E. Blonder and M. Tinkham;** Physica 109 & 110B, 1657 (1982)

[43] **A.H. Silver and J.E. Zimmerman**; Phys. Rev. 157, 317 (1967)

[44] **R. Rifkin and B.S. Deaver**; Phys. Rev. B 13, 3894 (1976)

[45] **E. Il'ichev, V. Zakosarenko, L. Fritzsch, R. Stolz, H.E. Hoenig, H.-G. Meyer, M. Gotz, A.B. Zorin, V.V. Khanin, A.B. Pavolotsky and J. Niemeyer**, Rev. Sci. Instrum. 72, 1882 (2001)

[46] **E. Il'ichev**; Phys. C 350, 244 (2001)

[47] **A.M. Kadin, L.N. Smith and W.J. Skocpol**; J. Low Temp. Phys. 38, 497 (1980)

[48] **W.J. Skocpol, M.R. Beasley and M. Tinkham**; J. Appl. Phys. 45, 4045 (1974)

[49] **A.M. Kadin, W.J.Skocpol and M. Tinkham**; J.Appl. Phys 33, 481 (1978)

Chapter 3
DC SQUIDs based on Niobium Nanobridges

In the previous chapter superconducting nanobridges, patterned by means of focused ion beam milling in a Niobium thin film, were described. As was discussed, the Josephson-like characteristics exhibited by these weak links allow for the realization of superconducting quantum interference devices (SQUIDs) based on these structures. By combining two superconducting nanobridges in a miniature superconducting loop, SQUIDs with very small areas can be created. Recent interest in such small sized SQUIDs has been motivated by the applicability of these devices as the detectors of small spin systems [1,2,3], phonons [4] and magnetic flux in a scanning microscopy setup [5,6]. The research described in the later chapters of this thesis is aimed towards the development of high resolution scanning SQUID microscopy. The development of miniaturized SQUIDs could be a first, critical, step towards further improvement of the resolution of such systems.

In this chapter the characteristics of miniature SQUIDs are described. The smallest realized device has an effective area ($A_{eff} = \Phi_0/H_0$) of 3.6 x 10^{-2} μm^2. Apart from from an application point of view, the characterization of these devices is also of fundamental interest since, in contrast to classical S-I-S based SQUIDs, it appears that the device properties cannot be described by commonly applied RSJ modeling. The exact ranges of possible sensor performance and properties are thus not yet fully clear.

In the first section of this chapter realized devices and their properties will be presented. The smallest obtained SQUID will be presented here. In the next part limitations regarding the degradation and reproducibility of the realized devices are discussed. The last section will be devoted to the description and analysis of measured noise characteristics.

3.1 DC SQUIDs based on Niobium nanobridges

As stated in the introduction to this chapter, in this section DC SQUIDs based on Niobium nanobridges will be described. The devices were all FIB patterned, using the method described in Chapter 2, in 5 μm wide, 50 nm thick, pre–defined Nb striplines. By patterning two nanobridges, separated by a hole, SQUIDs are created. Current–voltage (*IV*) and voltage–field (flux) (*V-H*(Φ)) measurements were performed at $T = 4.2$ K. The measurement method is schematically depicted in figure 3 - 1.

In figure 3 - 2 a scanning electron micrograph of the smallest obtained SQUID structure is shown. It is based on two nanobridges with 80 nm designed widths, separated by a hole with a diameter corresponding to the beam size (150 nm). In figure 3 - 3 the *IV* characteristics for different applied fields and the voltage – applied field (*V-H*) modulations corresponding to this device are shown. Because of the small size of the SQUID, the maximum applicable magnetic field in the setup (approximately 75 mT) corresponds to an applied flux of about 1.5 Φ_0 through the SQUID loop. The effective area ($A_{eff} = \Phi_0/H_0$, where H_0 is the magnetic field required to complete one oscillation in the device *V-H* characteristic*)* of this SQUID, is approximately 3.6 x 10^{-2} μm^2. This is more than twice as large as the estimated hole size (1.6 x 10^{-2} μm^2), which corresponds to the geometrical area (A_{geo}) of the device.

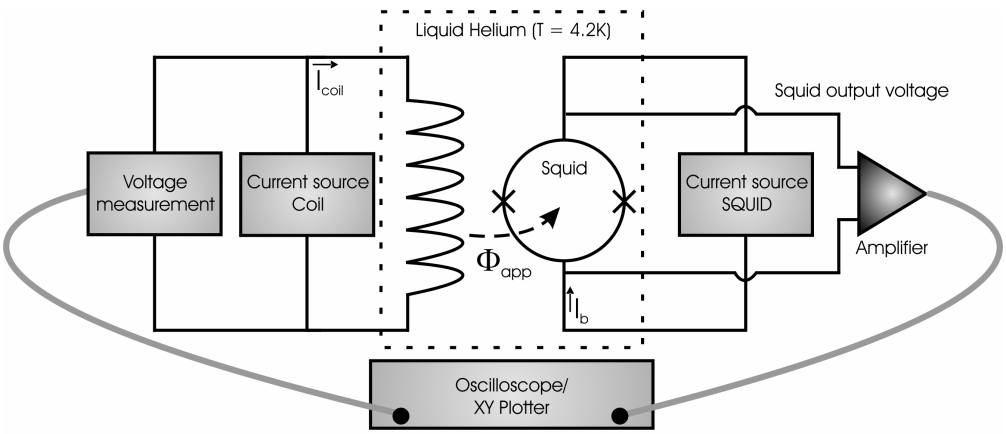

Figure 3 - 1:
Schematic representation of the experimental setup used for the measurement of the SQUID V-H characteristics. The value of the applied field is determined from the measured voltage across the two terminals of the (non–superconducting) Copper coils.

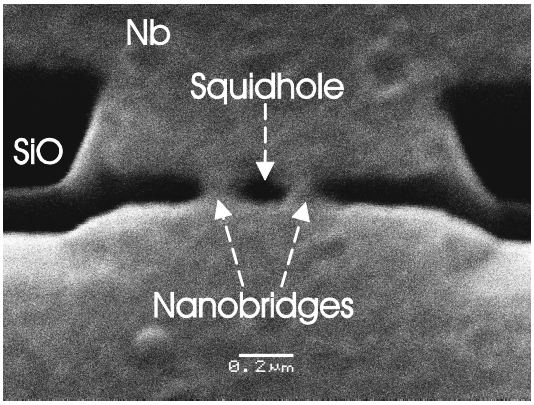

Figure 3 - 2:
Scanning electron micrograph of a SQUID based on Niobium nanobridges with an effective area of about 3.6 x 10⁴ nm². Designed bridge–width: 80 nm.

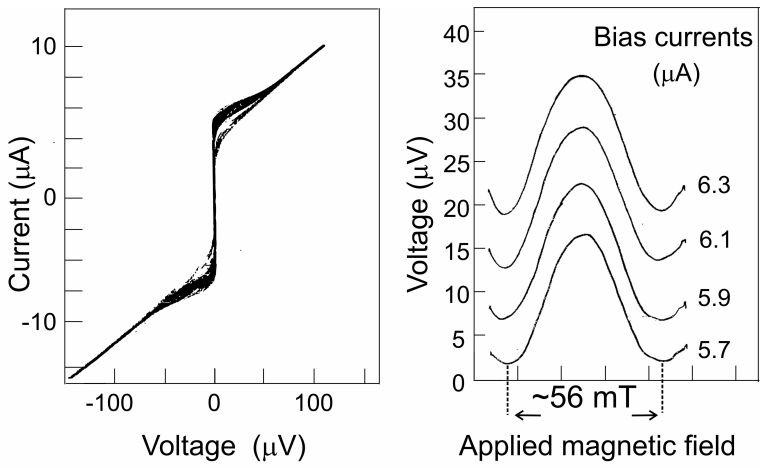

Figure 3 - 3:
(A) IV characteristic at T = 4.2 K for the SQUID shown in figure 3 - 2.
(B) Measured V-H modulation for different bias currents.

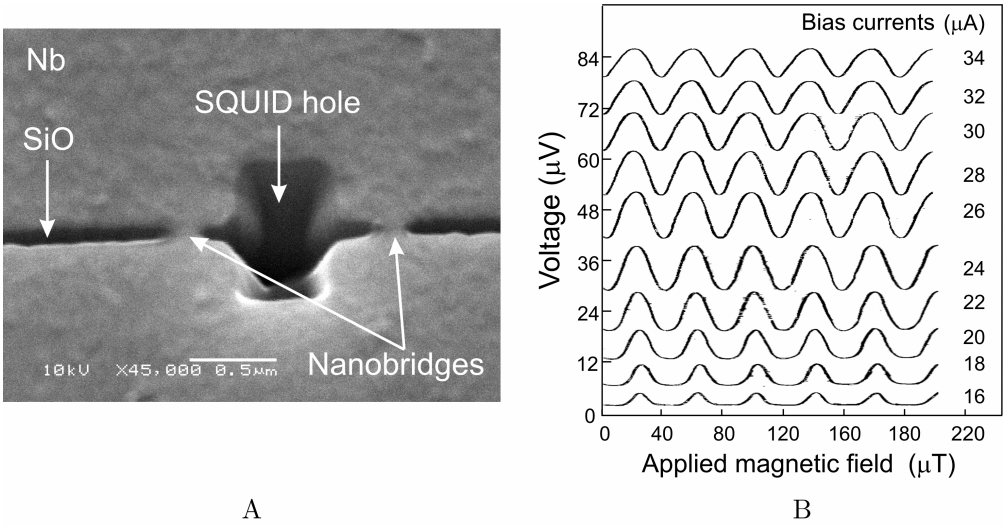

Figure 3 - 4:
(A) Scanning electron micrograph and (B) measured V-H characteristics of a SQUID based on Niobium nanobridges with an effective area of about 5 squared microns. Designed bridge–width: 80 nm.

The difference between A_{eff} and A_{geo} can be attributed to flux focusing effects [7]. Furthermore, the fact that the damaged Nb near the edges of the patterned structures is non-superconducting at $T = 4.2$ K results in an increased sensor diameter. The characteristics shown in figure 3 - 4 correspond to a reference device with an effective area of 5 μm^2, based on nanobridges with the same designed widths as was the case for the SQUID discussed above. Given the larger effective area of this SQUID, several oscillations in the *V-H* characteristics could be measured. Upon closer inspection of the depicted characteristics, shifts in the positions of the *V-H* maxima as a function of the bias current can be distinguished. This can be attributed to an asymmetry of approximately 30% in the critical currents of the two bridges.

.

A significant difference in the properties of both aforementioned devices can be noted ($I_{c,A} \approx 5$ µA, $I_{c,B} \approx 15$ µA; $\mathrm{d}V/\mathrm{d}\Phi_{max,A} \approx 50$ µV/Φ_0, $\mathrm{d}V/\mathrm{d}\Phi_{max,B} \approx 80$µV/$\Phi_0$). Critical currents ranging from 4 to 30 µA, maximum magnetic sensitivities ranging from 40 to 200 µV/Φ_0 and modulation depths of up to 50 µV have been measured for SQUIDs based on 80 nm wide bridges. This spread in the properties of devices based on bridges with the same designed widths is caused by the limitations posed by the FIB patterning process.

Because the eventual nanobridge diameters are smaller than the beam diameter, any irregularities in the beam properties during patterning can lead to significant differences in the sizes and shapes of the eventual bridges. For devices with $I_c \geq 25$ μA, hysteretic IV characteristics were measured, which do not allow for conventional current biased V-Φ measurements. The origin of this hysteresis, as described in the previous chapter, is attributed to thermal heating effects, which result from the hotspots associated with the phase-slip centers in the structure [8,9].

The characteristics of several produced sensors are compared in figure 3 - 5. In part (A) of this figure the critical current of different SQUIDs as a function of the designed bridge width is shown. In part (B) the maximum depths of voltage modulation (ΔV) and SQUID sensitivities ($\delta V/\delta\Phi$) are displayed. Typical measured values are 50 μV for the maximum modulation depth and 50 – 200 $\mu V/\Phi_0$ for the SQUID sensitivity. These values are comparable to those found in literature for classical DC SQUIDs based on tunnel junctions [10,11].

Applicability of RCSJ modeling

The prediction of the performance of "conventional" resistively shunted tunnel junction based SQUIDs is commonly based on RCSJ modeling, as described in chapter 1. The possible applicability of these design rules for DC SQUIDs based on superconducting nanobridges is not clear. The main reason for this is that there is no defined shunting resistor. The dynamic resistance (R_{dyn}) of the SQUID should be considered instead.

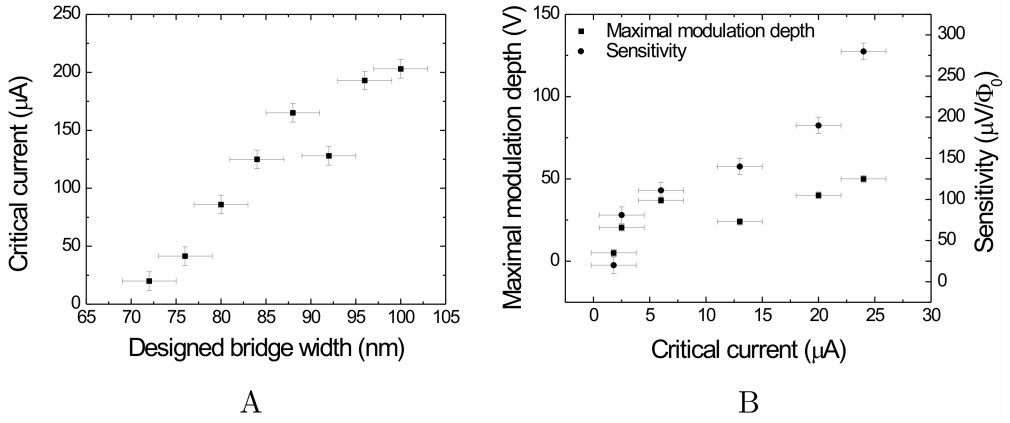

Figure 3 - 5:
(A) SQUID critical current as a function of designed bridge width (50 nm thick Nb film).
(B) Maximum modulation depths and sensitivities for SQUIDs based on Niobium nanobridges (50 nm thick film) with different critical currents.

The value of this resistance is expected to be determined not only by the normal zones across the bridge structure, but also by the non–superconducting shunting layer. This layer is formed by the Gallium implanted area. For large values of the applied bias current ($I_{bias} >> I_c$), R_{dyn} is well defined. Upon inspection of the SQUID IV characteristics, however, it can be noted that for bias currents just above $I_{c,}$ this value changes as a function of I_{bias}.

Several equations predicting SQUID performance in the RCSJ model are only valid in the regime where the screening parameter $\beta_L \approx 1$. In the limit of small $\beta_{L,}$, Tesche and Clarke have predicted that the current modulation depth, defined by $\Delta I_{\mathrm{c}}/I_{\mathrm{c}}$, should be about 1 [11]. For some of the described devices, however, much smaller modulation depths are reported. One possible reason for this is, as described in the previous chapter, the relatively large kinetic inductance (L_k) of superconducting nanobridges. From the literature it is known that L_k can be approximated by [12]:

$$L_k \approx \frac{1}{\pi}\frac{\Phi_0 l}{\pi I_c \zeta(T)} \tag{3.1}$$

Here l denotes the bridge length and $\xi(T)$ the coherence length. Based on this formula, for a bridge with $l \approx 150$ nm and $\xi(T) \approx 37$ nm a total kinetic inductance of 75 pH can be estimated.

In figure 3 - 6 (A) the relative modulation depth ($\Delta I_{\mathrm{c}}/I_{\mathrm{c}}$) is shown for different calculated values of L_k. It should be noted that, since the described equations for L_{k} only hold for bridges with lengths of several coherence lengths ($l > 3.49\ \xi(T)$), the data represented in these graphs is only valid if this condition holds.

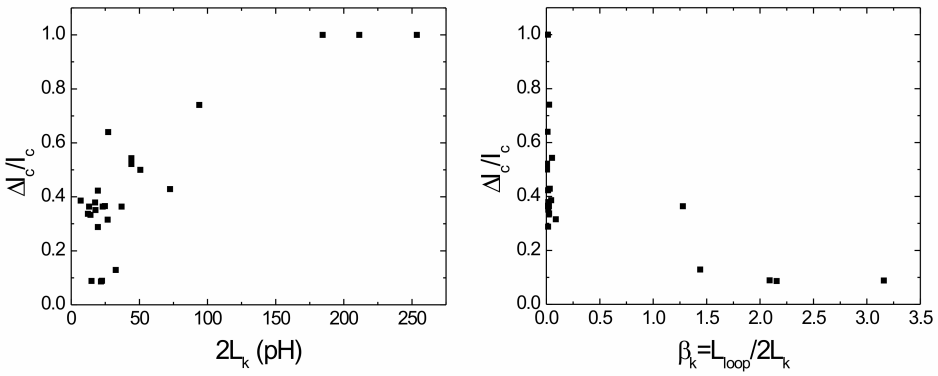

Figure 3 - 6:

$\Delta I_{\mathrm{c}}/I_{\mathrm{c}}$ vs. L_k (A) and $\Delta I_{\mathrm{c}}/I_{\mathrm{c}}$ vs. $L_{\mathrm{loop}}/2L_{\mathrm{k}}$ (B) for different SQUIDs based on Niobium nanobridges.

In part (B) of this figure $\Delta I_c/I_c$ is plotted as a function of L_k/L_{loop} , with L_{loop} the loop inductance of the SQUID. In analogy with the RSJ screening parameter β_L, which is defined by the proportionality between the Josephson and loop inductances, this ratio is called β_k. From this figure it can be concluded that for large values of L_k, the relative modulation depth tends to a higher value, ultimately reaching unity. This result resembles predictions made for RCSJ devices with small loop inductances (and thus relatively large Josephson inductances) by Clarke and Tesche [11], i.e. SQUIDs with $\beta_L << 1$.

Typically, the approximation of the maximum SQUID sensitivity is based on the value of the screening parameter $\beta_L = 2I_cL/\Phi_0$. For the SQUID shown in figure 3 - 2 ($I_c \approx 5\,\mu A$, $dV/d\Phi_{max} \approx 50\ \mu V/\Phi_0$, $R \approx 10\,\Omega$ and $L \approx 1$ pH), β_L would have a value of approximately 5 x 10^{-3}. From simulations described in [11] it is known that for $\beta_L < \approx 0.1$, $dV/d\Phi_{max} \approx \beta_L R/L$. This results in an estimated maximum modulation depth of $100\,\mu V/\Phi_0$, which is of the same order of magnitude as the measured value

Based on the literature [13], however, it can be expected that the total inductance of miniature nanobridge based SQUIDs is dominated by the contributions of the kinetic inductances of the bridges, which was given by equation 3 - 1. For the device discussed above ($l \approx 150$ nm and $\xi(T) \approx 37$ nm), a total kinetic inductance of 150 pH can be estimated, yielding a calculated value of $\beta_L \approx 0.75$. For such values of β_L, $dV/d\Phi_{max}$ can be estimated by $2\beta_L/(1+\beta_L)\ R/L$ [11], which results in $dV/d\Phi_{max} \approx 115\ \mu V/\Phi_0$. A possible explanation for the lower value of the measured maximum transfer would be overestimation of the kinetic inductances of the nanobridges.

As was described before, a systematic onset of hysteresis in the SQUID IV characteristics is noted for devices with $I_c \geq 25\ \mu A$, which corresponds to a nanobridge I_0 of approximately 12 μA. Classically, the McCumber parameter $\beta_c = 2\pi I_0 R^2 C/\Phi_0$ is used to differentiate between hysteretic ($\beta_c > 1$) and non–hysteretic ($\beta_c < 1$) junctions. The capacitance of a nanobridge is approximated by a parallel plate configuration consisting of the two banks of the electrodes: $C = \varepsilon_0 d/A$, with $\varepsilon_0 \approx 8.8$ x 10^{-12} F/m the permittivity of free space, d the separation corresponding to the geometrical bridge length (≈ 150 nm) and A the transverse area of the banks (≈ 5 μm x 50 nm). This yields a negligibly small value of $C \approx 10^{-17}$ F. At $T = 4.2$ K typical values for R are 10 – 20 Ω. Given these values for C and R, $\beta_c << 1$ for $I_c = 12\ \mu A$. Based on this discussion, patterned Nb nanobridges with $I_0 = 12\ \mu A$ at $T = 4.2$ K are likely to exhibit non-hysteretic IV characteristics at this temperature. This supports the claim that the hysteresis in the IV characteristics of the described devices results from self–heating effects, as is also reported for MgB_2 nanobridges in [14]. From the CPR measurements described in the previous chapter it is also known that a transition from the Josephson-like to the phase-slippage CPR regimes can be induced as a function of decreasing temperature. The critical current of the nanobridge at the cross-over is estimated to be 12 μA, which is in correspondence with the cross-over critical current measured for the SQUIDs (≈ 2 x 12.5 μA = 25 μA). In

order to obtain non-hysteretic SQUIDs, it can thus be concluded that the nature of the CPR in the nanobridges should be single-valued.

Upon analysis all realized devices exhibited an "excess current" (I_{exc}) in their IV characteristics. This means that the current at higher voltages does not extrapolate back to zero current at zero voltage. The "excess current" is defined as the interception of this extrapolation with the zero voltage axis. Its occurrence can be attributed to the extra charge transmitted in the multiple Andreev reflection process [15]. In figure 3 - 7 the measured excess current (I_{exc}) is plotted as a function of the SQUID critical current (I_c) for several devices. For lower critical currents, a near linear dependence of I_{exc} on I_c can be noted. This would be in accordance with predictions made in [16] and [17]. In these studies the contribution of the excess current to the total critical current is expected to scale with the gap voltages of both electrodes ($I_{exc} \approx 4/(3R_N)$ x $(\Delta+\Delta')$). For S-N-S type junctions Δ/R_N scales with the critical current. If a similar relation also holds for S-S'-S type structures, this could explain the linear increase of the total excess current as a function of the device critical current. For larger critical currents a linear dependence of I_{exc} on I_c is not apparent. This could be an indication of a change in the physical mechanism determining the CPR in the device. On average, devices with critical currents of approximately 150 μA are based on bridges with designed widths of 120 – 150 nm. Possibly this could indicate a transition from 1D depairing to a CPR determined by the nucleation and subsequent motion of vortices.

As was described in the previous chapter, a transition in the physical mechanism determining the CPR from one dimensional depairing to coherent vortex motion is expected for bridge widths of in the order of $\approx 4.4\ \xi(T)$. At $T = 4.2$ K, $\xi(T)$ for Nb ($T_c \approx$ 9 K) would have a length of approximately 37 nm, resulting in $4.4\ \xi(T) \approx 160$ nm.

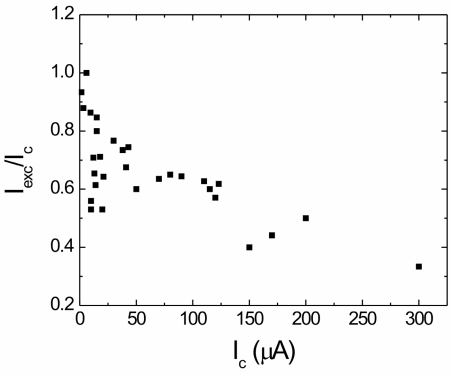

Figure 3 - 7:
Measured excess current (I_{exc}) as a function of the device critical current for several SQUIDs based on nanobridges with different designed widths.

The described deviation from linear behavior in I_{exc} vs. I_c could thus well be an indication of the proposed transition in the nature of the CPR. When interpreting this result, however, the uncertainties in designed bridge widths and the lack of measurement data describing devices with larger critical currents should be taken into account.

In the next section the limitations posed to the reproducibility of patterned SQUIDs are described. It turns out that even if there were an accurate model describing the characteristics of nanobridge based SQUIDs, the low device reproducibility would limit its application. Based on the measured critical current, however, a better expectation about the performance can be given.

3.2 Reproducibility and lifetime of nanobridge SQUIDs patterned by means of focused ion beam milling.

Reproducibility

As described in chapter 2, the nanobridge patterning process is based on the overlap of two focused ion beam profiles. Because the eventual structure will have dimensions that are smaller than or comparable to the diameter of the ion beam, this means that any irregularities in the beam during the patterning process will lead to significant differences in patterned devices. During a patterning session these differences could be caused by vibrations of the system. More importantly and significantly though, differences from session to session occur due to changes in the focus and shape of the ion beam. Since the focusing process is based on visual feedback (minimization of the stigmatism and optimization of the focus occurs before patterning by observing the sizes and shapes of patterned test–holes), it is assumable that significant differences in the beam shape and size occur over the course of different patterning sessions. Furthermore, the focus of the beam might vary as a function of the position on the sample. In figure 2 - 11 in the previous chapter the critical currents of several patterned nanobridges, created in different patterning sessions, were compared. Immediately noticeable was the fact that there is a large spread in the values of the critical currents of devices based on nanobridges with the same designed width. This holds both for structures created during the same patterning session as well as for devices fabricated in different sessions.

Even though the predictability of the characteristics of patterned devices is limited, the simplicity and fabrication time of the patterning technique allow for the creation of several devices per session. By preparing structures with a spread in designed bridge widths, the probability of obtaining one or more SQUIDs with the desired critical current is increased significantly. It can thus be concluded that by taking the expected spread in

characteristics into account it should not be a severe limitation on designed experiments. As a final comment it should be stated that with state of the art FIB systems much smaller beam diameters can be achieved than with the system used to fabricate the nanobridges described here. This would take away the need to apply the overlapping beam based patterning technique. Based on the assumptions described in this section the use of such a system could thus yield significant improvements on the reproducibility of patterned nanobridges. An overview, indicative of the spread in electronic properties and the onset of hysteresis in the device IV characteristics, of the properties of several realized SQUIDs is given in table 3 – 1.

Designed bridge width (nm)	I_c (μA)	$\mathrm{d}V/\mathrm{d}\Phi_{\max}$ ($\mu V/\Phi_0$)	$\Delta V_{\max}$ (μV)	R (Ω)
60	1.5	10	3.5	11
60	1.2	39	12	9.8
60	15	200	42	8.8
65	6	117	29	9.6
65	43	*hyst*	*hyst*	9.8
65	3.3	66	16	12
65	9.5	115	34	12.6
70	0.5	*hyst*	*hyst*	n/a
70	1	*hyst*	*hyst*	n/a
70	10	107	31	12.2
70	20	603	68	10
70	10	92	27	9
70	7	134	34	11.4
70	15	681	69	10
70	41	*hyst*	*hyst*	9.4
70	38	*hyst*	*hyst*	9.9
70	12	120	13	11.1
75	14	377	59	11.4
75	30	*hyst*	*hyst*	11
75	70	*hyst*	*hyst*	8.6
75	18	*hyst*	*hyst*	11.6
80	90	*hyst*	*hyst*	12
80	175	*hyst*	*hyst*	10
80	110	*hyst*	*hyst*	10.5
80	100	*hyst*	*hyst*	10.5
80	47	*hyst*	*hyst*	n/a
80	21	*hyst*	*hyst*	10.7
80	50	*hyst*	*hyst*	9
80	--	*hyst*	12	80
80	50	*hyst*	*hyst*	n/a
85	115	*hyst*	*hyst*	12.5
85	110	*hyst*	*hyst*	12.5
90	120	*hyst*	*hyst*	13
90	13	109	32	10.4
90	375	*hyst*	*hyst*	12
90	260	*hyst*	*hyst*	9

Designed bridge width (nm)	I_c (μA)	$\mathrm{d}V/\mathrm{d}\Phi_{max}$ ($\mu V/\Phi_0$)	ΔV_{max} (μV)	R (Ω)
90	200	*hyst*	*hyst*	10
90	200	*hyst*	*hyst*	9.5
90	250	*hyst*	*hyst*	10
90	123	*hyst*	*hyst*	12
100	425	*hyst*	*hyst*	10.6
110	170	*hyst*	*hyst*	10

Table 3 - 1:
Electronic properties of several realized SQUIDs. In the table, "hyst" denotes devices with hysteretic IV characteristics. SQUIDs with no measured resistance (n/a) exhibited significant curvature at large currents in the IV characteristic.

In this thesis the critical current of realized SQUIDs has predominantly been used to characterize the devices. The choice to use this parameter instead of the designed widths of the incorporated nanobridges was made, because the predictability based on this latter characteristic proved limited. It should, however, be noted that, even though I_c appears to be a better predictor of SQUID performance ($\delta V/\delta I$, ΔV_{max} etc.), its applicability is also limited. Firstly, the critical current of a nanobridge is determined by its cross–sectional area while the CPR of the structure is dependent on its width. Nanobridges with identical critical currents can have different shapes, resulting in different CPR's. Secondly, since the SQUID critical current is the sum of the critical currents of the two nanobridges, it is not a measure of the individual bridge characteristics. Depending on the amount of asymmetry between the two nanobridges, SQUIDs with different properties but identical critical currents can be realized. These limitations can account for the measured spread in device properties for SQUIDs with identical critical currents.

Lifetime

No significant degradation of the measured sensor properties was noted over the course of time. This is illustrated in table 3 – 2, where the electronic properties of three devices are monitored over the course of three months. No significant degradation can be noted. However, after several months and cooldowns most SQUIDs became defective from one cooldown to the other. The reasons for this are unclear, but are expected to be of accidental rather than intrinsic nature. Possible causes are the sensitivity of the SQUIDs for external influences such as static electricity during the handling of the device (wire bonding, sample mounting etc.) and thermal stresses occurring during cooling and subsequent warm–ups.

The prestructuring of the Niobium film by means of photolithography is done on a 2 inch wafer, yielding hundreds of sites that are suitable for focused ion beam patterning. After optimizing the focus of the ion beam several SQUIDs can be patterned within a

couple of minutes. This allows for a trial and error approach when designing the samples. Obviously, this poses severe limitations for industrial applications of such devices. However, for the experimental scientist conducting experiments in a laboratory, this should pose only minor setbacks.

Device 1				
	I_c (μA)	ΔI_c (μA)	ΔV_{max} (μV)	$dV/d\Phi_{max}$ ($\mu V/\Phi_0$)
Fabrication date	10	5.2	34	134
After 1 month	9.7	5.4	32	132
After 2 months	9.5	5.4	32	132
After 3 months	9	5.4	33	132
Device 2				
	I_c (μA)	ΔI_c (μA)	ΔV_{max} (μV)	$dV/d\Phi_{max}$ ($\mu V/\Phi_0$)
Fabrication date	8.8	5.2	29	117
After 1 month	8.3	5.0	31	125
After 2 months	8.0	5.0	27	110
After 3 months	8.2	5.0	28	113
Device 3				
	I_c (μA)	ΔI_c (μA)	ΔV_{max} (μV)	$dV/d\Phi_{max}$ ($\mu V/\Phi_0$)
Fabrication date	2.6	2.3	12	39
After 1 month	2.3	1.8	12	44
After 2 months	2.3	1.9	11	38
After 3 months	2.3	1.7	11	40

Table 3 - 2:
Measured SQUID characteristics for three different devices over the course of three months. No significant device degradation can be noted.

3.3 Noise measurements

Noise measurements were performed on a nanobridge based SQUID with a critical current of 15 μA and an area of 900 μm^2, using a conventional DC SQUID with an integrated flux–transformer [18] as a low temperature pre–amplifier. This measurement technique is schematically shown in figure 3 - 8. The principles of operation of a two stage SQUID setup are described elsewhere, e.g. in [19 and 20]. Depending on the voltage swing per Φ_0 in the first stage, an amplification (G) of 20 – 50 $\Phi_{0,stage\ 2}$ / $\Phi_{0,stage\ 1}$ can be achieved. The exact value of this coupling constant can be easily verified during

experiments. The used second stage SQUID has a known flux noise spectral density of 1.5 $\mu\Phi_0/\mathrm{Hz}^{1/2}$. If the flux noise spectral density of the first stage is several times larger than $(1.5\ \mu\Phi_0/\mathrm{Hz}^{1/2})/\mathrm{G}$, the contribution to the measured noise of the first stage should be the dominant factor. If the noise spectrum of the nanobridge based SQUIDs (typical $\mathrm{d}V/\mathrm{d}\Phi = 100\ \mu\mathrm{V}/\Phi_0$) was measured solely with an available commercial room temperature amplifier with a documented voltage noise spectrum of 2 $\mathrm{nV}/\mathrm{Hz}^{1/2}$, the minimum detectable flux noise spectral density would be around 20 $\mu\Phi_0/\mathrm{Hz}^{1/2}$. For this reason application of a low noise, low temperature pre–amplifier step, such as the 2–stage SQUID construction described above, is necessary.

Noise measurements were performed in a flux locked loop (FLL) scheme. In figure 3 - 9 the measured flux noise spectrum, exhibiting a white noise level of 1.5 $\mu\Phi_0/\mathrm{Hz}^{1/2}$ and a $1/f$ corner frequency of about 80 Hz, is shown. The clear peaks in the spectrum, occurring at approximately 30, 50 Hz and 46 kHz can be attributed to extrinsic influence on the measurement setup and the effects of the 50 Hz mains. This conclusion is based on the fact that similar peaks were also observed in measured spectra for completely different experiments and devices. The drop–off at approximately 50 kHz results from bandwidth limitations. The inductance of the SQUID washer is estimated to be 63 pH [7], yielding a calculated energy resolution of 7.1 x 10^{-32} Js (≈107 h).

The relatively high onset of $1/f$ noise (80 Hz, whereas for SIS tunnel junction based SQUIDs values as low as 1 Hz are commonly reported, e.g. in [21]) could be an indication of the degradation of the Niobium film resulting from the FIB patterning process. From literature it is known that the $1/f$ noise level depends strongly on the film quality [22]. It can be expected that the dominant $1/f$ noise source can be associated with the magnetic moments of electrons trapped in defect states in the superconductor [23]. Contributions to the total $1/f$ noise level related to the trapping and subsequent motion of flux lines in the SQUID body are likely to be limited due to the relatively small washer area.

For conventional SQUIDs the flux noise level reduces with a decrease of the geometrical inductance. However, due to the small effective areas, measurements of the noise characteristics of miniaturized SQUIDs proved challenging. Since all the devices are based on the same type of Josephson element, the flux noise spectral density (Φ_n) reported above for the 900 $\mu\mathrm{m}^2$ SQUID can be used to calculate an upper limit for the spin sensitivity (S_n) of smaller sensors. An expression for this spin sensitivity can be derived by calculating the total flux of a magnetic dipole that couples into the SQUID loop. If the magnetic dipole is located in the middle of the SQUID loop (with radius a), field lines returning within the loop will have no net contribution to the sensed total flux, as is schematically shown in figure 3 - 10. An estimate for the net flux coupled through the ring can be made by integrating the dipole field over the surface of an infinite circle from the edge of the superconducting loop.

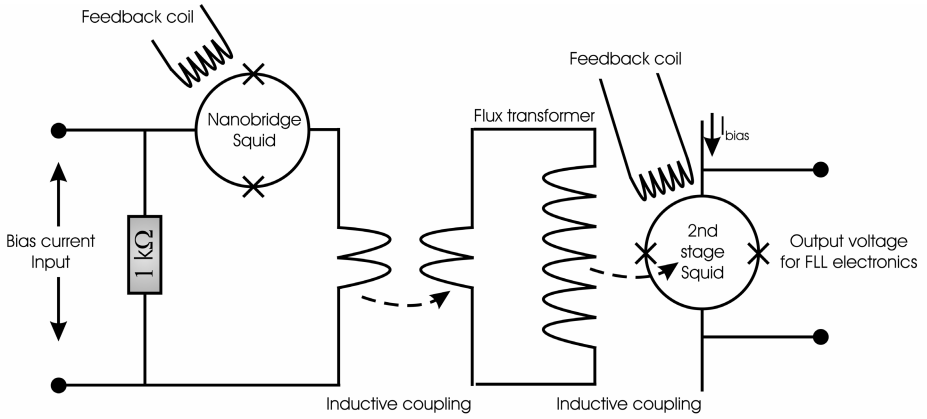

Figure 3 - 8:
Schematic representation of the two–stage SQUID measurement setup based on a flux transformer.

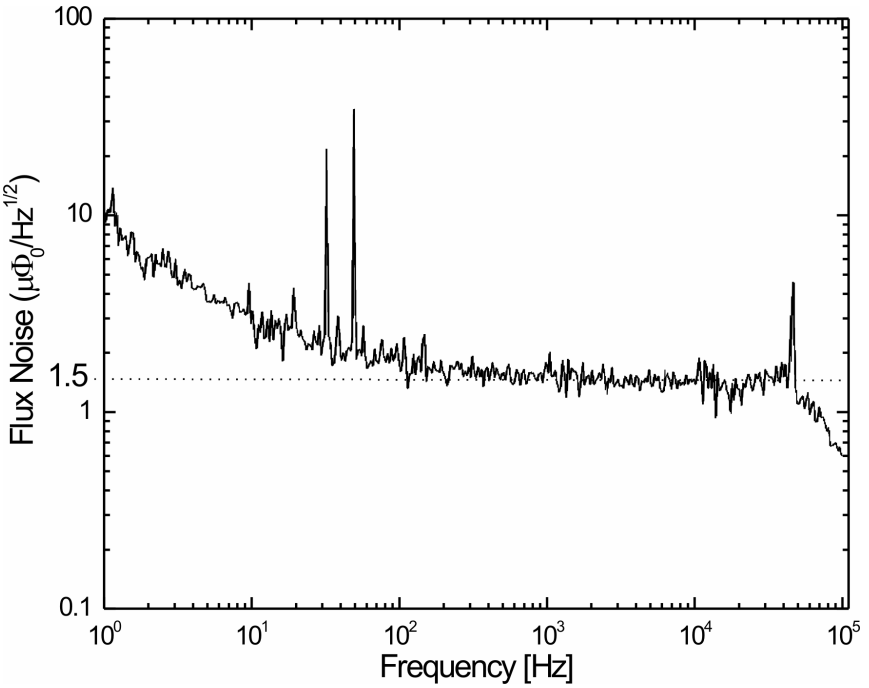

Figure 3 - 9:
Noise spectrum measured for a nanobridge based SQUID with an effective area of 900 μm^2 and an I_c of 15 μA.

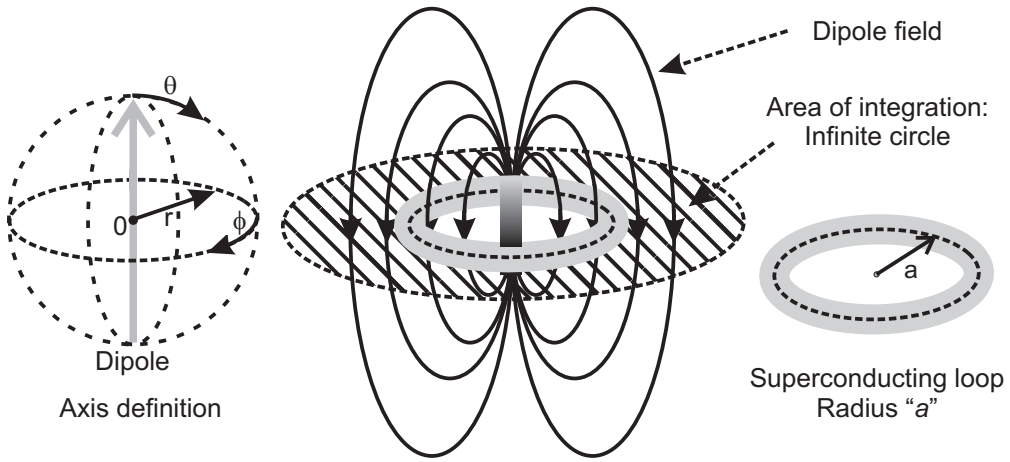

Figure 3 - 10:
The flux from a magnetic dipole located in the center of a superconducting loop coupling back into the loop can be estimated by integrating the total flux through the surface of a sphere with the radius of the loop.

A short derivation of the eventual expression will be given next. The magnetic properties of a single spin can be represented by a magnetic dipole with a moment with a magnitude equaling 1 μ_B (Bohr magnetron). Based on this, the magnitude of the magnetic field of a single spin can be described by the following expression [24]:

$$\left|\vec{B}(r,90^o-\theta)\right| = \frac{\mu_0\mu_B}{4\pi r^3}\sqrt{1+3\sin^2(90^o-\theta)} \tag{3.2}$$

In figure 3 - 10 the definition of the spherical coordinate system (described by r,θ,ϕ axes) is given. Since the magnetic flux equals the surface integral of the magnetic field, the flux through the surface of the imaginary circle minus the flux through the superconducting loop can be calculated as follows:

$$\Phi_{\text{int}egration\_area} = \frac{\mu_0\mu_B}{4\pi}\sin\theta\Big|_{\theta=90^o}\int_0^{2\pi}\int_a^{\infty}\frac{1}{r^3}rdrd\varphi = \frac{\mu_0\mu_B}{4\pi}2\pi\left|-\frac{1}{r}\right|_a^{\infty} = \frac{\mu_0\mu_B}{2}\frac{1}{a} \tag{3.3}$$

Since the detection of spins located inside the SQUID washer takes places in the presence of flux noise, described by the flux noise spectral density Φ_n, the spin sensitivity (S_n) in units of μ_B per $Hz^{1/2}$ can then be defined as:

$$S_n = \frac{\Phi_n}{\Phi_{1spin}} = \frac{2a\Phi_n}{\mu_B \mu_0} \tag{3.4}$$

Based on this expression, which was also reported in its final form in [5], a device with an area of 3.6 x 10^{-2} μm^2 and a flux noise spectral density of 1.5 $\mu\Phi_0/Hz^{1/2}$ would have a spin sensitivity of about 55 $\mu_B/Hz^{1/2}$.

This would imply that it is possible to reduce the spin sensitivity below the lowest experimentally reported values so far ($S_n \approx 70$ $\mu_B/Hz^{1/2}$ [25] (for a device with $a \approx 0.5$ μm and $\Phi_n \approx 0.4\,\mu\Phi_0/Hz^{1/2}$) and $S_n \approx 200$ $\mu_B/Hz^{1/2}$ [26] ($a \approx 100$ nm and $\Phi_n \approx 5.2\,\mu\Phi_0/Hz^{1/2}$)), which were obtained with EBL - based nanobridge devices.

The first reported value of S_n (≈ 70 $\mu_B/Hz^{1/2}$) was obtained for SQUIDs with steep, non–sinusoidal $V - \Phi$ characteristics, exhibiting large maximum transfers of up to 6 mV/Φ_0. As was described before, the expected flux noise is directly related to this maximum transfer. Based on the fabrication methods described in this thesis, SQUIDs with similar large voltage to flux sensitivities have also been created. An example of the $V - \Phi$ modulation characteristics of such a device, with $I_c \approx 20$ μA, is shown in figure 3 - 11. The maximum estimated value for $dV/d\Phi$ for this SQUID is 6 mV/Φ_0. Based on this large value, which is attributed to the steep slopes of the $V - \Phi$ characteristics separating the two nearly hysteretic states, a smaller flux noise level (and thus spin sensitivity) could in principle be expected. Noise measurements on such devices have, however, not been conducted.

Note should be taken that the derivation of the expression for the spin sensitivity is based on the assumption that the magnetic moments are located in the center of the SQUID loop. Furthermore, they should be aligned to an axis perpendicular to the plane of the washer. This is obviously not a realistic interpretation of a possible experiment. The highest spin sensitivity is expected when the dipole is located close to the edge of the washer. In practice, however, the accuracy of the positioning of the particles does not yet allow for such well-defined experiments.

However, apart from giving an estimate of the minimum value of S_n, based on the derived expression also different sensors can be compared. From literature it is known that for conventional DC SQUIDs based on tunnel junctions, the optimum flux noise level is expected for $\beta_L \approx 1$ [11]. For such devices, decreasing the geometrical inductance results in smaller levels of the energy resolution as long as $\beta_L > 1$. For $\beta_L < 1$, a decrease of the SQUID inductance is expected to result in an increase of the flux noise. Based on this, the assumption concerning the possible spin sensitivity of a miniaturized device

described above, should not be taken for granted until the noise properties of several devices with different loop inductances are characterized. Since no clear definition of β_L can be given for the described nanobridge based SQUIDs, it is conceivable that a miniature device could have a larger flux noise spectral density. Based on values reported in literature [25,26], however, low flux noise values can be expected for miniature devices.

3.4 Summary

The realization and characterization of SQUIDs based on FIB patterned Niobium nanobridges were discussed in this chapter. These devices were fabricated by patterning two nanobridges in a superconducting loop. The smallest realized device has an effective area of 3.6 x 10^{-2} μm^2. As described in chapter one, potential applications for such miniature SQUIDs are for the detection of small clusters of magnetic particles and in Scanning SQUID microscopes.

To estimate the spin sensitivity of such a small SQUID, noise measurements were conducted on a larger device ($A_{eff} \approx 900$ μm^2) based on the same type of nanobridge. The measured white noise level of the flux noise spectral density for this device was 1.5 $\mu\Phi_0/Hz^{1/2}$.

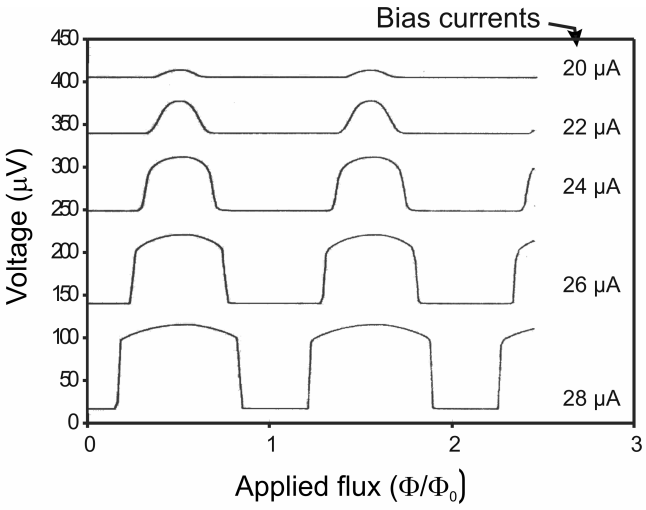

Figure 3 - 11:
Voltage to flux modulation characteristics for a SQUID with a critical current of approximately 20 µA. Because the device is nearly hysteretic, steep V-Φ curves are measured. $dV/d\Phi_{max}$ is approximated to be 6 mV/Φ_0.

Based on this value the estimated upper limit for the spin sensitivity of the miniature SQUID was approximately 50 $\mu_B/Hz^{1/2}$, which would make the device an attractive sensor for the study of clusters of magnetic nanoparticles.

The applicability of miniaturized SQUIDs in SSM systems will be determined by the development of proper read–out mechanisms. Conventional SQUID read–out mechanisms are based on the flux locked loop operation of the sensor. This requires the application of modulation fields corresponding to the coupling of several Φ_0 in the SQUID washer. Because of the small geometrical inductance of the miniaturized devices, this would locally require a large magnetic field. Apart from the technical difficulties associated with the generation and stabilization of such a field, this would also influence the sample which is to be studied. A solution for this would be developing an open–loop read–out mechanism, which does not require flux modulation. Such a setup, allowing for the operation of sensors with hysteretic IV characteristics, was recently developed by Hasselbach et al. [6]

Bibliography

[1] **M. Jamet, W. Wernsdorfer, C. Thirion, D. Mailly, V. Dupuis, P. Melinon and A. Perez**; Phys. Rev. Lett. 86, 4676 (2001)

[2] **J. Gallop, P.W. Joseph – Franks, J. Davies, L. Hao and J. MacFarlane**, Phys. C 368, 109 (2002)

[3] **S.K.H. Lam and D.L Tilbrook**; Appl. Phys. Lett. 82, 1078 (2003)

[4] **L. Hao, J.C. MacFarlane, S.K.H. Lam, C.P. Foley, P.W. Joseph – Franks, J.C. Gallop**; IEEE Trans. Appl. Supercond. 15, 514 (2005)

[5] **J. Dechert, K. Krischker, T. Goddenhenrich, M. Muck and C. Heiden**, IEEE Trans. Appl. Supercond. 7, 3143 (1997)

[6] **K. Hasselbach, C. Veauvy and D. Mailly**; Phys. C. 332, 140 (2000)

[7] **M.B. Ketchen**; IEEE Trans. Magn. 23, 1650 (1987)

[8] **A.M. Kadin, W.J. Skocpol and M. Tinkham**; J. Appl. Phys. 33, 481 (1987)

[9] **K. Hasselbach, D. Mailly and J.R. Kirtley**; J. Appl. Phys. 91, 4431 (2002)

[10] **J. C. Gallop, B.W. Petley**; J. Phys. E 9, 417 (1976)

[11] **C. D. Tesche and J. Clarke**; J. Low. Temp. Phys. 29, 301 (1977)

[12] **K.K. Likharev**; Rev. Mod. Phys. 51, 101 (1979)

[13] **J.H. Claasen**; Appl. Phys. Lett. 40, 839 (1982)

[14] **A. Malisa, S. Charlebois and T. Lindström**; Jour. Appl. Phys. 98, 124395 (2005)

[15] **T.M. Klapwijk, G.E. Blonder and M. Tinkham**; Physica 109 & 110B, 1657 (1982)

[16] **G.E. Blonder, M. Tinkham and T.M. Klapwijk**; Phys. Rev. B 25, 4515 (1982)

[17] **G.E. Blonder and M. Tinkham**; Phys. Rev. B 27, 112 (1983)

[18] **J. Pleikies, O. Usenko, K.H. Kuit, J. Flokstra, A. de Waard and G. Frosatti**; "SQUID developments for the gravitational wave antenna MiniGrail", to be published in IEEE Trans. Appl. Supercon. June (2007)

[19] **M. Podt, J. Flokstra and H. Rogalla**; Phys. C 372 – 376, 225 (2002)

[20] **M. Podt, L. Gottardi, A. De Waard, G. Frosatti and J. Flokstra**; IEEE Trans. Appl. Supercon. 15, 785 (2005)

[21] **V. Foglietti, W. Gallagher, M. Ketchen and A. Kleinasser, R. Koch, S. Raider and R. Sandstorm**; Appl. Phys. Lett. 49, 1393 (1986)

[22] **H. Weinstock and R. Ralston (eds.)**; The New Superconducting Electronics, Kluwere Academic Publishers, The Netherlands (1993)

[23] **R.H Koch**, **D.P. DiVicenzo and J. Clarke**;arXiv.org:cond-mat/0702025 (2007)

[24] **D.J. Griffiths**; Introduction to Electrodynamics, Prentice Hall, USA (1999)

[25] **R.F. Voss, R.B. Laibowitz, A.N. Boers, S.I. Raider, C.M. Knoedler and J.M. Vaggiano**; IEEE Trans. Magn. MAG – 17, 395 (1981)

[26] **S.K.H. Lam**; Supercon. Sci. Technol. 19, 963 (2006)

Chapter 4
Scanning SQUID Microscopy: Systems and Sensors

Based on research conducted in recent years, scanning SQUID Microscopy has proven to be a very powerful tool for the imaging of the magnetic flux directly above a sample. The first SQUID microscope, capable of performing one dimensional scans above a sample, was developed in 1983 [1]. The term "scanning SQUID microscope" was introduced in 1993 by Vu and van Harlingen to describe their cryogenic two dimensional SQUID magnetic imaging system, which was capable of achieving spatial resolutions of 20 μm and magnetic sensitivities of 10^{-5} $\Phi_0/\mathrm{Hz}^{1/2}$ [2]. Following the reports of these pioneering projects, around the world, numerous systems have been realized, yielding vast improvements in magnetic and spatial resolutions and even resulting in the development of commercial systems (Seiko Instruments, first reported in 1999 [3]).

A separation can be made into two distinctive groups of SQUID microscopes: Systems with both the sample and sensor immersed in a cryogen (liquid Helium or Nitrogen), yielding minimal separation between sensor and sample [3.4,5,6,7,8] and microscopes which allow for measurements of samples at room temperature by separating the SQUID and sample environments [9,10,11,12]. The research described in this thesis is conducted on two systems, both of which are of the first described type:

- A system based on linear actuators, as described in [5], developed at the IBM TJ Watson research center, Yorktown Heights NY, USA, and donated to the University of Twente. Two versions of this system are in use. The first one is operated in a liquid Helium environment, whilst the second one allows for variable temperature measurements (up to $T \approx 50$ K) in a Helium exchange gas environment.

- A system developed at the University of Twente, based on a low temperature piezo scanner. As is the case with the second system described above, the measurements are conducted in an exchange gas (Helium, $T = 4.2$ K) environment. Measurements can, however, only be conducted at $T = 4.2$ K.

In this chapter a description is given of both the used SSM sensors as well as the systems. In the first section some general aspects, applicable to both systems will be described. The SQUIDs, which are of a pick–up loop type geometry, are discussed in the second section, followed by a description of both systems in the final parts of the chapter.

4.1 General aspects

As discussed in the introduction, two scanning SQUID microscope systems will be described in this chapter. The main difference between the two systems is the scanning mechanism. As will be described later in the chapter, the scanning mechanism in the microscope developed at the IBM TJ Watson Research Center, Yorktown Heights NY, USA, is based on the translation of motion induced by linear actuators from the outside of the cryostat system to the inside. The microscope developed at the University of Twente is based on piezo scanners, which are operated in a Helium exchange gas environment at $T = 4.2$ K. This allows for operation within the system cryostat.

The sample to sensor geometry in both systems is, however, comparable. The SQUID, which is glued on a cantilever cut out of 25 μm thick Brass foil, is scanned in contact with and at an angle of approximately 10 degrees to the sample. Conducting the measurements with sample and sensor in contact yields the highest spatial resolution, because the separation between the two is minimized. Scanning at an angle is then, in turn, necessary to allow for minimal friction and to create room for the wire–bonds leading to the SQUID bonding pads. In such an angled geometry, the sample to sensor separation is minimized if the SQUID pick-up loop is located exactly at the edge of the SQUID chip. To achieve such a setup, the SQUID chips are polished before mounting.

Apart from the resemblance with respect to the applied sensors, the signal read–out mechanism in both systems is similar. The SQUID signal is measured and controlled using the same set of electronics (*SQUID controller, custom made at the IBM TJ Watson Research Center*). The read–out principle is based on a standard AC flux - modulated flux - locked - loop scheme (FLL) [13], schematically shown in figure 4 - 1. During measurements, the SQUID is operated at a constant bias current (I_b) just above the critical current and with a 100 kHz square wave modulating flux with a period corresponding to approximately 1/2 Φ_0, as is shown in figure 4 - 2.

By changing the DC value of the modulation flux, the working point of the SQUID is chosen such that the voltage difference between the two states corresponding to the square wave flux is zero. An external flux through the SQUID loop will shift this DC value yielding a nonzero voltage difference, which is then measured at the output of the FLL circuit. This signal is in turn also fed back to the SQUID via the modulation coil to restore the sensor to its original state yielding no voltage difference.

In practical systems the output voltage noise of a DC SQUID, typically in the range of $1nV/Hz^{1/2}$ [14], is smaller than the input noise of a conventional DC (pre-)amplifier.

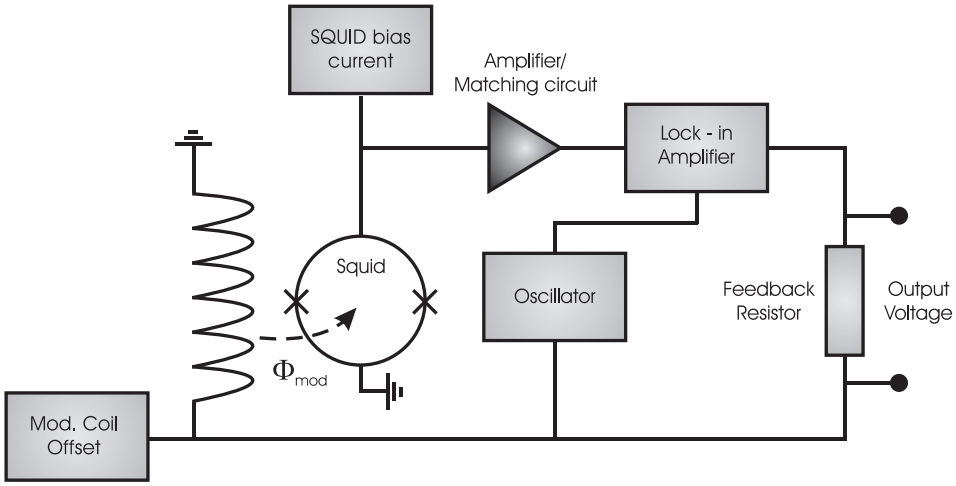

Figure 4 - 1:
Standard Flux Locked Loop (FLL) setup.

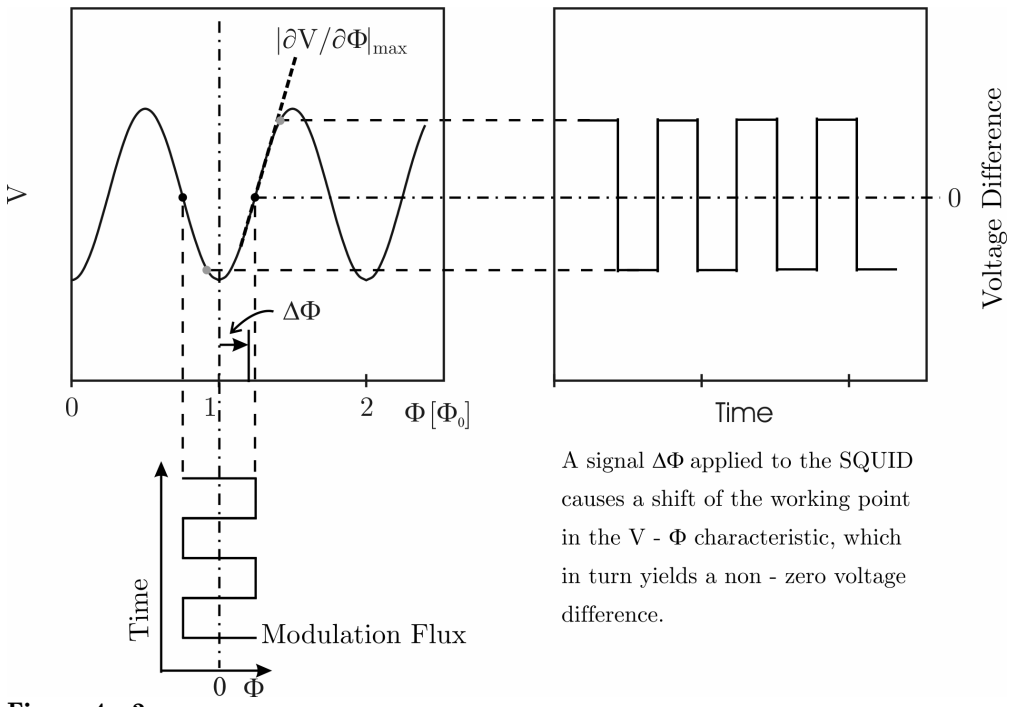

A signal $\Delta\Phi$ applied to the SQUID causes a shift of the working point in the V - Φ characteristic, which in turn yields a non - zero voltage difference.

Figure 4 - 2:
Flux – locked - loop (FLL) measurement principle.

To solve this matching problem usually a step–up transformer or a resonant LC circuit is used. For the SQUID microscopes described in this thesis a 10 : 300 transformer is used to amplify the SQUID AC voltage signal. The actual read–out electronics of both systems, operated at the same temperature as the sensors, are schematically shown in figure 4 - 3

As will be discussed in the next section, the modulation coils are implemented directly on the SQUID chips. The coil inputs are then connected to the rest of the circuitry using Aluminium wire bonds. The matching circuits, consisting of 10 : 300 step–up transformers, are composed of two torroids wound around the same ferrite core. The output of this transformer is then led to the room temperature pre–amplifier.

Since the measurement principle is the same in both SQUID microscopy setups, the used sensors are interchangeable. The only difference is the mounting configuration. In the next section the applied SQUIDs are described. The conventional sensors, designed at the IBM TJ Watson Research Center, are produced at the Hypres Inc. foundry [15]. Apart from these devices, also adapted versions of these sensors have been used, where focused ion beam patterning is applied to reduce the effective pick–up loop area. A complete overview of both these types of devices is given next.

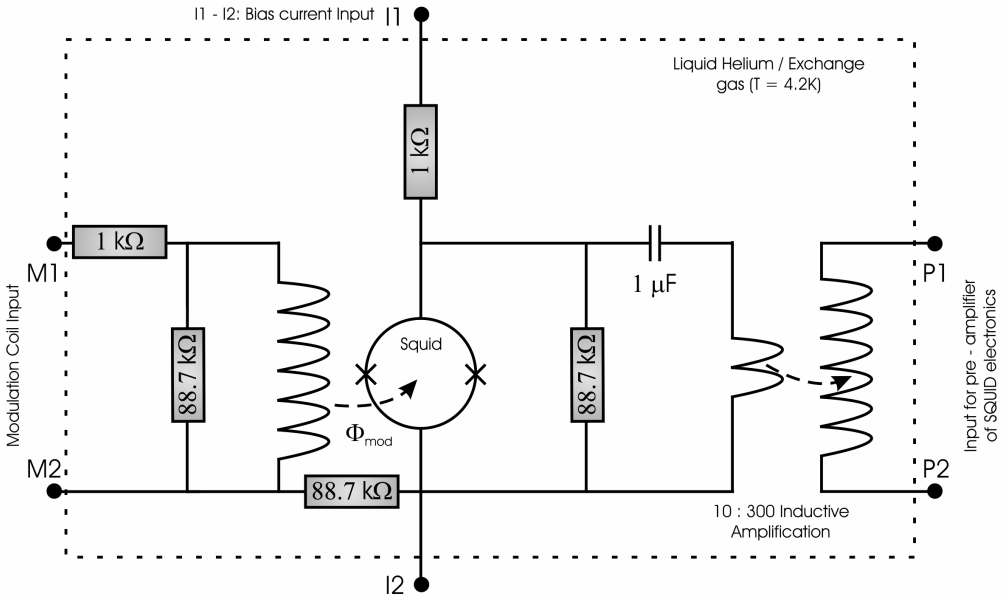

Figure 4 - 3:
SQUID read–out electronics: Low temperature part. M1 – M2 is the modulation coil input, P1 – P2 is the pre–amplifier output and I1 – I2 the connection for the SQUID bias current.

4.2 Scanning SQUID microscopy sensors

In this section the different SQUID types used for the microscopy measurements described further on in this thesis are discussed. All the sensors have a pick–up loop type of geometry. The pick-up loop, which is the sensor area sensitive to flux from the sample during measurements, is connected to the SQUID washer by means of magnetically shielded (superconducting) leads. The lateral separation between the two structures is approximately 1.2 mm. As described before, the SQUID chip is scanned at an angle with respect to the sample and the pick-up loop is located close to the edge of the chip. This implies that, during measurements, the pick-up loop is located significantly closer to the sample and is thus more sensitive to the flux patterns above the sample. The main advantage of such a design is that the sensitive area of the SQUID can be miniaturized, while the washer area, which incorporates the Josephson junctions and damping resistors, can be designed and optimized according to standard procedures.

The applied SQUIDs are based on conventional Nb – AlO_x – Nb trilayer junctions fabricated at Hypres. Two types of sensors are used: samples with complete pick–up loop geometries and half–fabricated structures, which allow for the nano–patterning of the pick–up loop structure by means of focused ion beam milling.

Pre-defined pick-up loop based SQUIDs

In the ideal SSM sensor optimized magnetic sensitivity and a relatively small effective area are combined. Furthermore, a good inductive coupling should exist between the SQUID washer and an external modulation source to allow for AC flux biased measurements, as described in the first section of this chapter. When fabricating such a device using available tri–layer photolithography technology, such as the junction technology offered by the Niobium foundry at Hypres, the dimensions of the sensors are limited by the dimensions of the smallest producible features and the criteria for the alignment of patterns in different layers. For the employed process all features should be at least 2 microns wide and separated by the same margin. This implies that a complex structure such as a SQUID washer with underlying modulation coil, which typically comprises several superconducting and insulation layers, will have a total area which is several times the minimum lead width. To overcome this limitation to the effective sensor area, the SQUIDs used in the SSM systems are based on a pick–up loop type geometry. In such a device the SQUID washer is separated by a relatively long shielded lead from the area which is sensitive to the magnetic flux produced by the sample that is to be measured. Because the SQUIDs are being operated at an angle relative to the sample this separation ensures that, when in contact, the pick–up loop is a lot closer to the sample and thus more sensitive to the flux patterns just above it.

In figure 4 - 4 a schematic overview of the sensors fabricated at Hypres is given. As mentioned before, two different versions are made: SQUIDs with fully patterned pick–up loops and half–fabricated devices, which have been completed in Twente by patterning the eventual pick–up loop structure with a focused ion beam.

The SQUIDs are based on junctions with an effective area of 22 μm^2, incorporated in a washer with an inductance of tens of pH. The designs are based on the 30 A/cm^2 Hypres process, which implies a designed SQUID critical current of 13.2 μA and junction capacitance of 9.4 x 10^{-12} F. To ensure non–hysteretic current–voltage characteristics, two shunt resistors of 5 Ω are incorporated in the design. Furthermore, a damping resistor of 5 Ω is applied in order to suppress LC resonances, which is in accordance with the following criterion:

$$R < \sqrt{\frac{L}{2C_j}} \approx 8.5\Omega \tag{4.1}$$

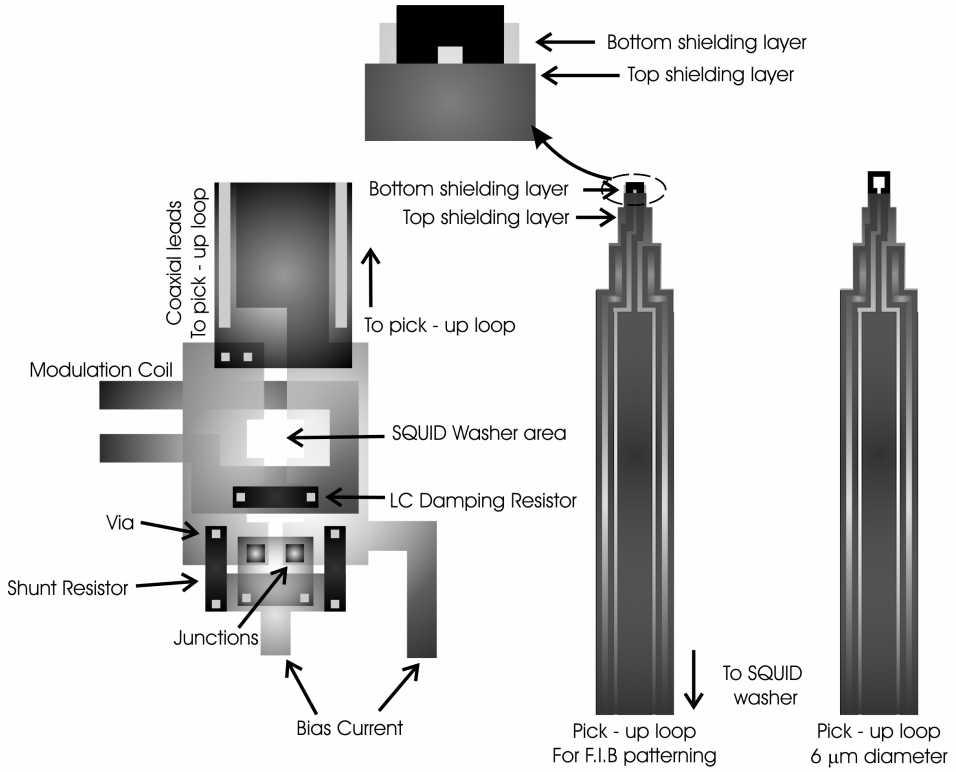

Figure 4 - 4:
Trilayer S-I-S SSM sensor layout.

A complete overview of the designed and calculated SQUID properties is given in table 4 - 1. In figure 4 - 5 an optical microscopy image of the SQUID washer area on one of the SSM sensor samples is shown. The separation from the pick–up loop to the SQUID washer is 1.2 mm, which, when scanning at an angle of 10 degrees corresponds to a lateral height difference with respect to the sample of approximately 210 μm. In order to get the pick–up loop as close to the sample as possible during scanning, the SQUID samples are polished using P4000 Silicon Carbide grinding paper.

Applying this polishing technique, samples where the pick–up loop is located exactly at the substrate edge can be realized. In figure 4 - 6, as an example, a picture of a polished sensor chip is shown. The pick–up loop in this picture is of the pre–fabricated type and has a diameter of 8 μm. The eventual separation from the edge is much less than this diameter. Three different pick–up loop diameters have been incorporated in the designs. Next to the 8 micron device, also sensors with pick–up loops of 6 and 10 micron diameters haven been produced. These measures correspond to the outer diameter of the structures.

The electronic characterization (IV and V-Φ measurements) of one device yielded the following results: $I_c \approx 12.5$ μA, $R \approx 3\ \Omega$ and $dV/d\Phi_{max} \approx 60\ \mu V/\Phi_0$. These values approximately correspond to the design parameters. The SQUID maximum transfer was estimated by $\beta_L R/L$. This formula was introduced in the previous chapter. It should be noted that the exact electronic characterization of the SSM sensors is not necessary for operation in a microscopy setup. For such experiments it is only important to determine the total voltage to flux sensitivity of the FLL setup.

Designed SQUID properties	
Junction area	5 x 5 μm^2
Effective junction area	22 μm^2
Washer inductance	16 pH
Damping resistor	8 Ω
Shunting resistors	2 x 8 Ω
Junction critical current	6.6 μA
Junction capacitance	9.4 x 10^{-13} F
Calculated SQUID properties	
Steward McCumber parameter (β_c)	0.5
Reduced inductance (β_1)	0.1
Flux noise spectral density ($S_\Phi^{1/2}$)	1.5 x 10^{-7} $\Phi_0/Hz^{1/2}$

Table 4 - 1: *Designed and calculated SQUID properties.*

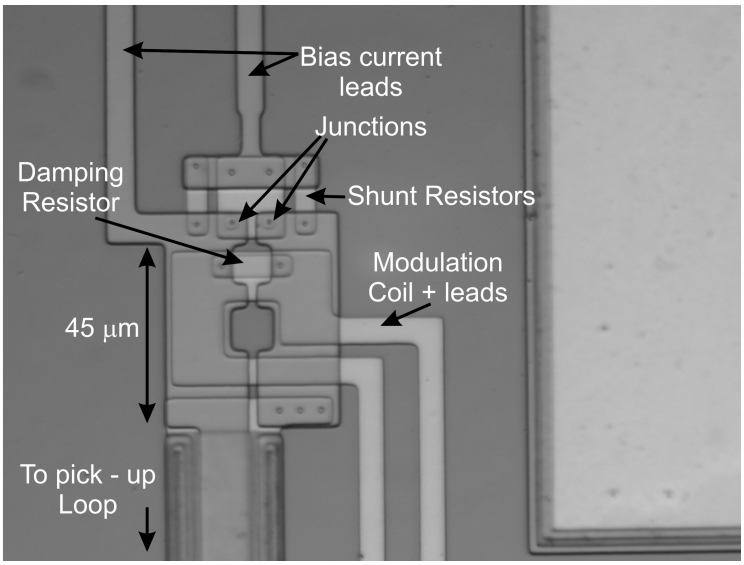

Figure 4 - 5:

Optical micrograph of the SQUID washer structure, fabricated at Hypres.

The 6 μm structure is the smallest pick–up loop geometry that can be fabricated at Hypres. Apart from the described SQUID magnetometers, also samples, based on the similar pick–up loop geometries, incorporated in a susceptometer layout have been produced. These devices, consisting of two pick–up loops connected to the SQUID washer and surrounding susceptometer coils, allow for standard susceptometry measurements. A complete description of these sensors can be found in [4]. In the next part of this paragraph sensors with pick–up loops patterned by means of focused ion beam milling are described.

FIB patterned pick-up loops

As mentioned before, the dimensions of the pick–up loops that can be realized using the standard lithography process available at Hypres are limited to line–widths of 2 microns. This results in the fact that the smallest producible device has an effective input coil with an outer diameter of 6 microns. To improve on this, as shown in figure 4 - 4, also samples were designed where the pick–up loop structure, which is to be finalized by means of focused ion beam milling, is half–fabricated at Hypres. Because the samples are produced in the standard runs, no flexibility concerning the order of the different layers exist.

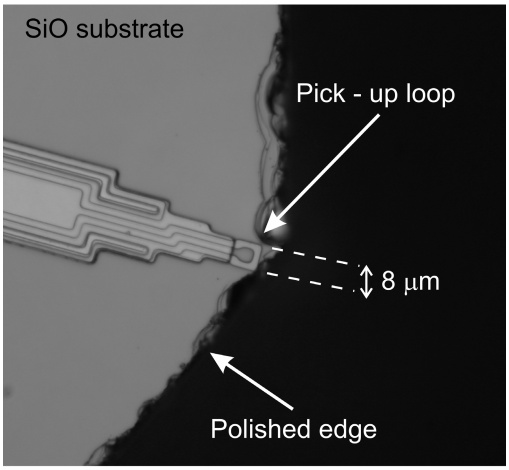

Figure 4 - 6:
Example of an SSM sensor with a pick–up loop with a diameter of 8 microns polished to the edge of the substrate. This image was taken using an optical microscope.

The eventual half–fabricated pick–up loops are thus covered by 500 nm of SiO, which is used to cover the complete sample area (with the exception of the contact pads). Furthermore, the pick–up loop structure, with a layer thickness of 300 nm, is separated from an underlying Nb shielding layer (100 nm) by a 135 nm thick insulating SiO layer. This bottom shielding layer was implemented in the original designs to reduce the parasitic inductance of the slit leading up to the pick–up loop.

The geometry of the half–fabricated devices consists of a small loop with 6 micron outer diameter, as shown in figure 4 - 4. The line width of the top part of the pick–up loop is 4 microns. This part of the structure half overlaps the underlying Nb shielding layer. The objective when patterning the pick–up loops in this arrangement of layers thus is to create a slit reaching the area where there is no more underlying shielding Nb and to pattern a pick–up hole connecting to this slit. Ideally, such a patterned geometry is more sensitive to the flux through the hole than through the shielded slit. However, due to flux focusing effects, the slit will still contribute significantly to the total pick–up loop inductance.

In order to keep the Nb underlying the slit in tact, care should be taken to pattern trenches with depths reaching no further than the bottom edge of the interlaying insulating SiO layer. This also implies that the suppression of superconductivity in Niobium structures patterned by means of FIB milling should be taken into account, as was described in chapter 2. For the applied process this effect is expected to extend as far as 35 nm inwards from the surface of a patterned structure.

To calibrate the patterning depth, the intensity of the FIB imaging signal, which consists of the amplified signal due to detected electrons emitted from the structure during patterning, is monitored. By monitoring this signal during the stepwise patterning of a trench in a multilayer structure (milled depth per step $<$ thickness of different layers $<$ total trench depth), the variation of the detected signal intensity as a function of the number of steps can be used as an indicator of the milling process. The results of such an experiment on the half–fabricated Hypres structures are shown in figure 4 - 7. Clear variations in the amount of detected electrons can be seen as a function of time. The short spike–like oscillations correspond to one etching scan. Taking into account that there is a difference in etch–rates for SiO and Nb, the relative lengths of the different signal levels correspond closely with the designed layer thickness. From the results of such experiments, the etch rates corresponding to the different layers comprising a sample can be calculated. Application of the determined values in the FIB patterning settings when structuring the eventual pick–up loop structures allows for controlled etching down to the interlaying SiO layer.

In figure 4 - 8 optical microscope images of two FIB patterned pick–up loops are shown. Because of the overlying insulating SiO layer, sample imaging by means of scanning electron microscopy proved to be challenging. The structure on the right hand side is polished all the way down to the pick–up loop edge, which, in principle, allows for minimal sample to sensor separation during SSM measurements. Several pick–up loops with hole diameters ranging from 200 to 500 nm have been created in similar fashion. As will be described in the next chapter, the eventual effective area of the sensor is, however, limited by flux focusing into the patterned hole during the measurements.

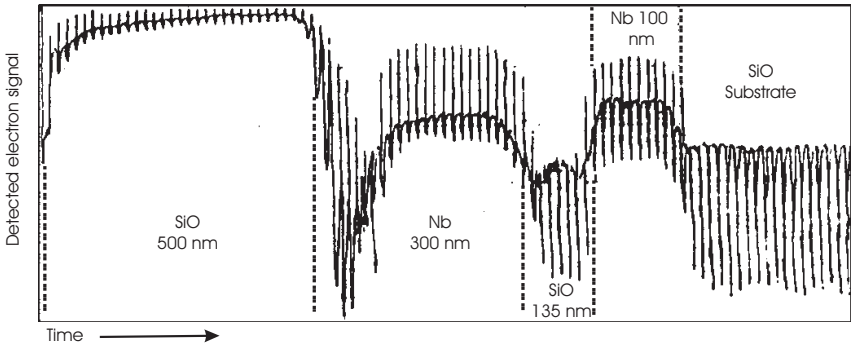

Figure 4 - 7:

By monitoring the detected electron signal during FIB patterning, the different layers comprising the sample can be detected, which allows for selectively etching down to a certain depth.

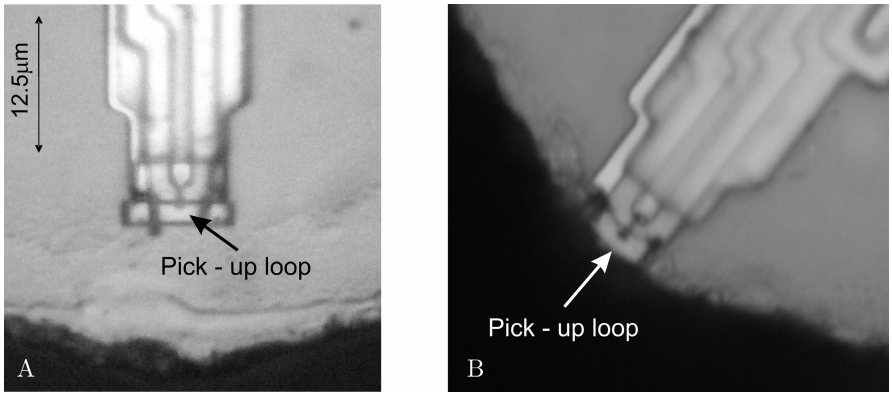

Figure 4 - 8:
Optical microscope images of two FIB patterned polished SSM sensors.

The extent of this effect can be somewhat reduced by narrowing down the pick–up loop leads and patterning several slits in the leftover parts of these leads.

To further miniaturize the effective area of the patterned pick–up loops, changes should be made in the design of the prefabricated structures. As described before, the geometry of these structures is limited by the employed fabrication process. Based on the presented method, achieving further miniaturization is not likely. In order to realize smaller pick–up loops the amount of layers, the layer–to–layer separation and the smallest achievable lead width should be reduced. This would require a complete new sensor design and fabrication process. From measurements described in the next chapter, however, it can be concluded that the sensors presented in this section already yield significant improvements in terms of SSM spatial resolution.

4.3 Scanning SQUID microscope systems

In this section the SSM systems, with which the microscopy experiments described in this thesis are conducted, are described. In the first part the system developed at the IBM TJ Watson Research Center is described. This system will be called the IBM SSM in further parts of this thesis. It is based on the translation of motion induced by linear actuators from outside the system into the cryostat. In the second part of the paragraph the piezo–based SSM system, which was built up in-house, is described.

Linear actuator based SSM system

In figure 4 - 9 a schematic overview of the IBM SSM system is given. The scanning motion, induced by 3 linear actuators (1 each for the X, Y, and Z directions), is translated via a pivoting principle into the cryostat. This is also schematically shown in this figure. Experiments have been conducted on two versions of this microscope:

- A version operating with sample and sensor in direct contact with the liquid Helium environment at $T = 4.2$ K.
- A variable temperature setup (*VT*), which is operated in a Helium exchange gas environment. Cooling is realized via thermal contact of the vacuum tube containing this gas to the surrounding liquid Helium.

The low temperature (4.2 K) version of the IBM SSM is operated with both sensor and sample in direct contact with the surrounding liquid Helium environment. In the variable temperature setup both sample and sensor are located inside a vacuum tube in a Helium exchange gas environment (pressure is typically 10 – 20 mbar). This vacuum tube is inserted in the same liquid Helium dewar used for the 4.2 K version of the system. Variation and stabilization of the temperature is achieved by operating local resistive heaters. Stable temperatures of up to 50 K can be reached in such fashion.

Even though the differences between the 4.2 K and variable temperature setup, as described above, are significant, both systems are discussed in the same section of this paragraph, since the scanning principle for both is comparable. Outside of the cryostat the motion of three linear actuators (*Newport 850G*) connected to three optical stages (for *XYZ* directionality) is transferred to the microscope stick. This motion is then translated to the sample mount (the other end of this stick) via a lever principle, by fixing the microscope stick in a pivot point at a certain position along its length. The corresponding lever ratio (2 for the 4.2 K system and 3 for the variable temperature setup) determines the eventual step sizes for the sample motion. The cumulative accuracy of the used actuators is limited to ≤ 0.1 % of the total travel range.

A limitation of the discussed scanning principle is the fact that, due to the lever based coupling, the sensor motion has a circular pattern. However, since typical scan ranges are of the order of 1 mm^2, the lateral height difference during scanning will be no more than a micron. When coarse positioning the sample over relatively large distances (up to 50 mm), though, there will be a significant variation in the separation between the sample and sensor.

Since, as described before, the scanning process is conducted with sample and sensor in contact and the cantilever is very thin and thus flexible, height variations in the order of micrometers are compensated for. In table 4 - 2 an overview of the described system properties is given.

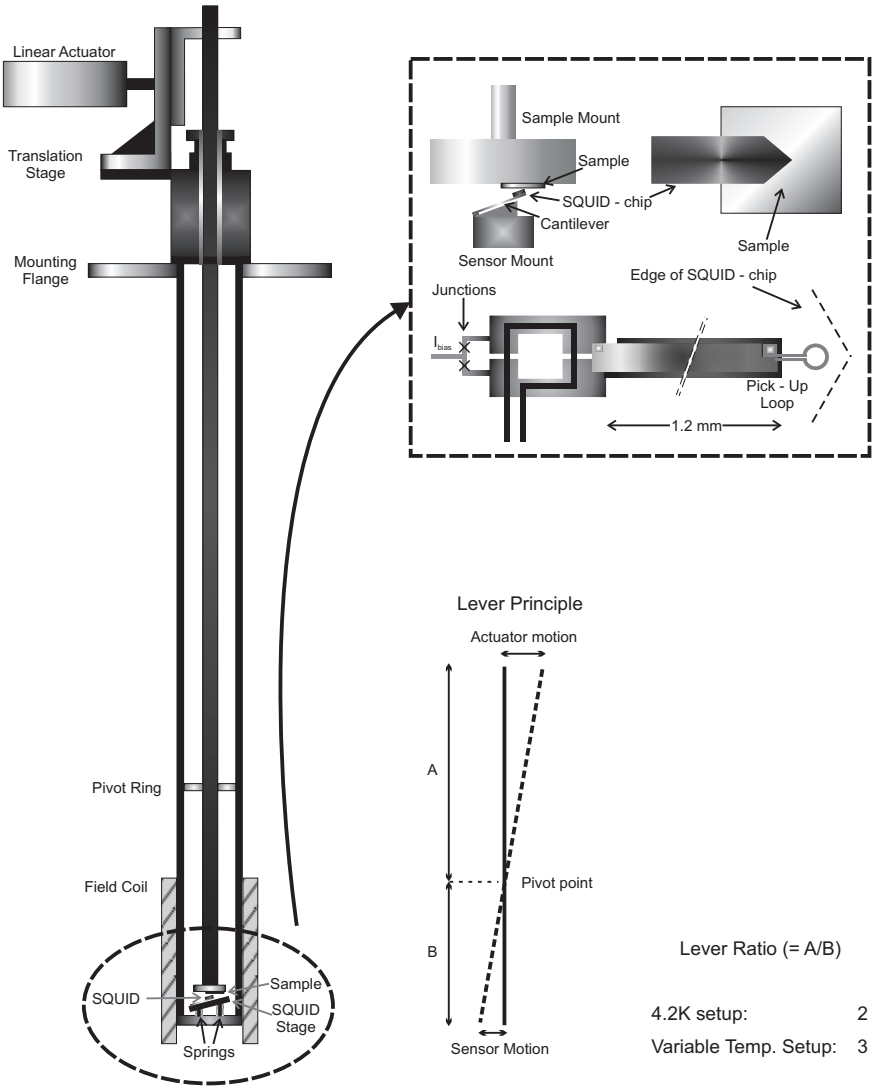

Figure 4 - 9:
4.2 K IBM Scanning SQUID microscope setup. The inset shows the arrangement of the sensor and sample during measurements. The system is operated in a liquid Helium environment.

The 50 liter cryostat used for SSM operation is equipped with a μ–metal shield, reducing the measured background field at the operating/cooling position at $T = 4.2$ K to approximately 2 μT. This was verified by counting the number of Abrikosov vortices penetrating a thin film of YBCO relative to the measured sample–area. To allow for the compensation of this residual background field and for field–dependent measurements, an additional field coil is mounted on the microscope stick. In the next chapter such measurements will be described in more detail.

System operation and data acquisition is achieved using a C++ driven application named *He3scan*, developed at the IBM TJ Watson Research Center. Using an NI–DAQ interface (*National Instruments PCI–6036E A/D card*) the amplified output of the SQUID electronics setup is measured as a function of the actuator position, which is controlled with a *Newport ESP300 Universal Motion Controller* through the RS32 serial port of a computer. Scan speeds (without lever–correction) ranging from 0.05 to 0.4 mm/s can be applied. Sample to sensor approach is realized by running one dimensional line scans as a function of the *z*–position. Typically, the sample–sensor distance is systematically reduced in steps of 10 microns until a steady signal is measured. When describing performed measurements in the next chapter, the different settings concerning pixel/image size and amplification will be given. Apart from *He3scan*, a separate C++ driven application named *Winmage* is used to display and manipulate acquired images.

In the next part of this paragraph the in-house built SSM system will be described. As discussed before, there are many similarities between this microscope and the IBM system. A key difference, though, is the scanning principle, which is based on commercially available piezo modules.

Newport 850G linear actuator based SSM setup properties		
Property	4.2 K System	*VT* system
Operating temperature	4.2K	4.2K – 50K
Operating environment	Liquid Helium	Helium exchange gas (~ 10 mbar)
Lever ratio	2	3
Step size accuracy (before lever reduction)	< 1 μm	< 1 μm
Travel range (before lever reduction)	50 mm	50 mm

Table 4 - 2:
Overview of the properties of the linear actuator based SSM systems.

Piezo based SSM setup

Improving on the spatial resolution of state of the art SSM systems, such as the IBM SSM described above, not only requires the miniaturization of the applied sensors. Limitations posed to the measurements by the scanning geometry should also be overcome. Given the pivot–point, lever–like coupling of the scanning motion produced by the linear actuators to the sample or sensor in the IBM SSM, step sizes are limited to $>$ 50 nanometers. Furthermore, over large scan areas lateral height differences will occur due to the circular scan motion.

Using conventional SSM sensors, which are produced by means of standard optical lithography, these limitations are negligible. As described, the smallest obtained sensor pick–up loop effective diameter is in the order of 4 microns, which is larger than the minimum applicable step size. Furthermore, typical sample to sensor separations of a couple of microns are achieved during measurements. The future development of nanopatterned pick–up loops, located close to the sample edge, would allow for the minimization of both the effective sample area and the sample to sensor separation during scanning. This could, however, create the need for a scanning system which is not limited by the minimum step size.

Based on these (future) requirements a choice was made to develop an SSM setup based on piezo actuators. These scanning modules can achieve step sizes of less than 1 nm. Furthermore, a direct coupling of the scanning motion to the sample or sensor can be realized, since the piezo scanners can be operated in a cryogenic environment. This eliminates the need of a lever–like construction.

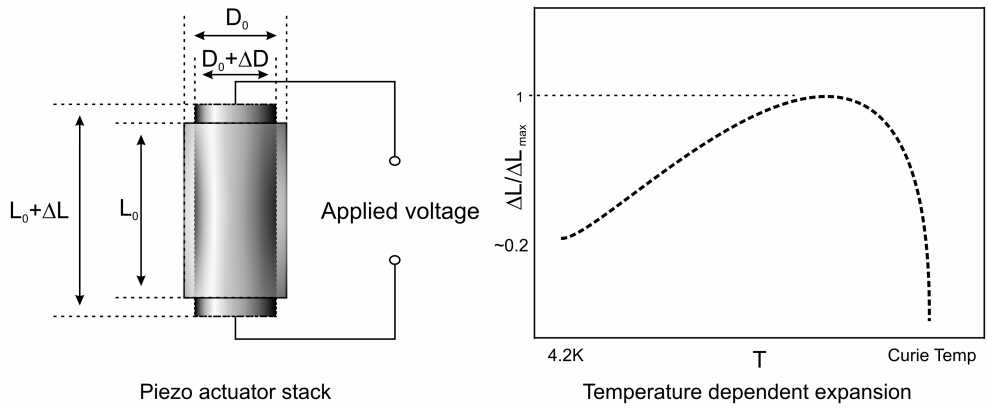

Figure 4 - 10:
(Left) Schematic of piezo actuator expansion. (Right) Typical temperature dependence of the expansion of a piezo actuator. Adapted from [16].

It is well known that the piezo–electric effect is limited by temperature. In figure 4 - 10 the expansion principle of a piezo–based actuator and the corresponding temperature dependence are displayed. From this picture it can be concluded that the range of a low temperature piezo scanning stage will be limited to about 20% of the room temperature range. Building a SQUID microscopy system based on typical piezo actuators would result in scanning ranges of less than a micron. To overcome this limitation, the SSM system was developed around a commercially available low temperature piezo scanning module [17]. According to specification, with this scanning module, the *ANSxy100* from *Attocube Systems Gmbh*, scan ranges as large as 30 x 30 μm^2 can be realized at $T = 4.2$ K. To allow for coarse positioning, three high precision piezo inertial positioning modules are also included in the system design.

The characteristics of the applied piezo positioning and scanning stages are summarized in table 4 - 3. A distinction is made between scanning motion, which is the linear expansion of the piezo actuator as a result of an applied voltage and travel, which is the inertial driven stick–slip motion of an actuator along a supporting axis. As shown in table 4 - 3, travel ranges of up to 7.5 mm can be achieved in such fashion.

In figure 4 - 11 a schematic overview of the layout of the realized piezo based SSM setup is given. As mentioned before, the sensor and sample positioning and signal readout methods are comparable to those of the linear actuator based system described in the first section of this paragraph. As is shown in figure 4 - 11, the whole system, including the scanning stage, is operated at $T = 4.2$ K in a Helium exchange gas environment. When warming up the system after measurements care is taken to avoid the condensation of water on the different piezo elements by flushing the whole vacuum tube with room temperature Nitrogen gas until temperatures above 273 K have been reached.

The system is operated via implemented *Labview* applications, which are used to control the coarse positioning through an *Attocube ANC150 electronic controller for positioners*, which is in turn controlled via the RS32 serial port of a computer.

Component	Operation	Range	Resolution
ANPxy/z100	Travel	7.5/6 mm (xy/z)	>5 nm (4.2 K)
	Scan	450 nm (4.2K)	~ 0.1 nm
ANSxy100	Travel	N/A	>5 nm (4.2 K)
	Scan	30 x 30 μm^2	~ 0.01 nm

Table 4 - 3:
(Low–temperature) Characteristics of the different piezo elements in the SSM setup.

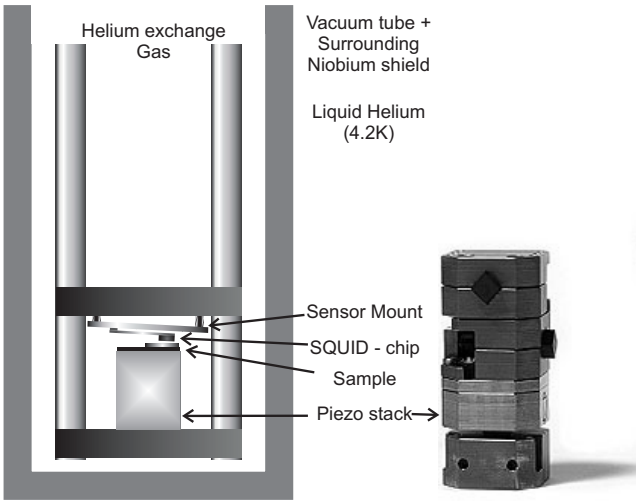

Figure 4 - 11:
Schematic layout of the piezo based SQUID microscope setup.

The (un-amplified) scanning voltage is generated using an *NI PCI–6036E A/D card*, which is also programmed to read–out the output voltage of the SQUID electronics. As mentioned in the first part of this chapter, the sensor read–out circuitry and electronics are similar to those implemented in the system developed at the IBM TJ Watson Research Center.

To control the sensor to sample approach a capacitive readout mechanism was implemented. The cantilevers on which the SQUID chips are glued consist of 2 strips of 25 μm thick brass, separated by approximately 1 mm. By measuring the change in the capacitance between these strips, which results from the induced deformation when the sample and sensor get into contact with each other, one can monitor the approach process.

In figure 4 - 12 (A) a measured capacitance curve (as a function of the number of piezo steps in z–direction) at room temperature is shown. In part (B) of this figure the approach mechanism is schematically depicted. To prevent damaging of the SQUID chip, a dummy was used for this measurement. Similar measurements have been conducted at $T = 4.2$ K with a SQUID chip on the cantilever. Typical changes in capacitance of a couple of pF can be detected when the chip and sample make contact. To prevent over–approaching, however, no complete capacitance curves, such as the one displayed in figure 4 - 12, have been recorded at this temperature.

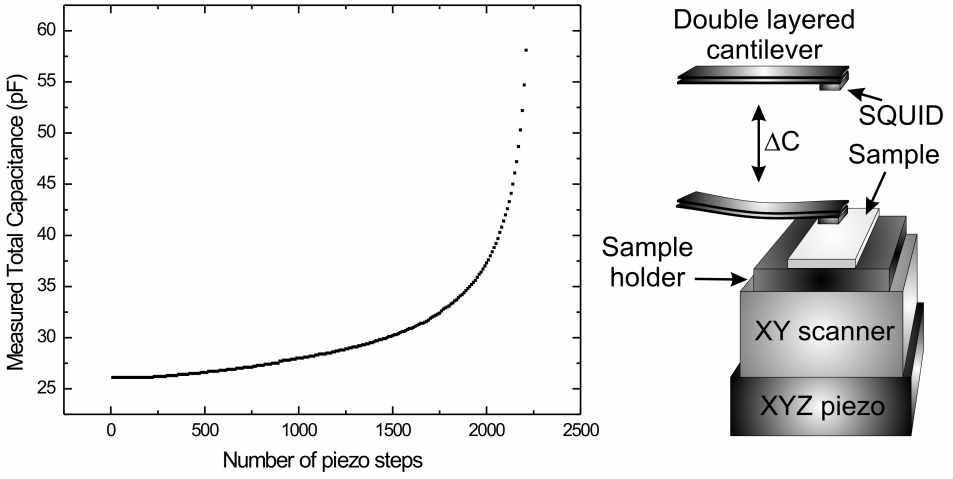

Figure 4 - 12:
Principle of capacitively monitored approach. (A) Measured capacitance as a function of z–piezo steps. (B) Schematic display of the approach mechanism.

4.4 Summary

In this chapter the available scanning SQUID microscopy systems and sensors have been described. Next to a piezo based setup, which was set up within the group, also the SQUID microscope donated by the IBM TJ Watson research center was discussed. Based on the applied scanning mechanism, the latter system allows for large scan–ranges, with step–sizes down to 1 μm. The potential of the piezo based setup lies in the accuracy of the piezo step sizes and scanning resolution (down to 1 nm). To fully utilize this potential the effective area of and separation from the sample of the applied sensors should be miniaturized.

In the next chapter SSM measurements, performed with both systems, will be described. Next to measurements conducted with the described conventional SSM sensors, also experiments based on the FIB miniaturized pick–up loop geometry SQUIDs will be discussed.

Bibliography

[1] **J.E. Zimmerman and J.E. Mercerea**; Phys. Rev. Lett. 13, 125 (1964)

[2] **L.N. Vu and D.J. van Harlingen**; IEEE Trans. Appl. Supercon. 3, 1918 (1993)

[3] **T. Morooka, S. Nakayama, A. Odawara, M. Ikeda, S. Tanaka and K. Chinone**., IEEE Trans. Appl. Supercond. 3491 (1999)

[4] **J.R. Kirtley, M.B. Ketchen, C.C. Tsuei, J.Z. Sun, W.J. Gallagher, L.S. Yu-Jahnes, A. Gupta, K.G. Stawiasz and S.J. Wind**; IBM Jour. Res. Dev. 39, 665 (1995)

[5] **J.R. Kirtley, M.B. Ketchen, C.C. Tsuei, J.Z. Sun, W.J. Gallagher, L.S. Yu-Jahnes, A. Gupta, K.G. Stawiasz and S.J. Wind**; Appl. Phys. Lett. 27, 1138 (1995)

[6] **K. Hasselbach, C. Veauvy and D. Mailly**; Phys. C 332, 140 (2000)

[7] **C. Veauvy, K. Hasselbach and D. Mailly**; Rev. Sci. Instrum. 73, 3825 (2002)

[8] **P.G. Bjornsson, B.W. Gardner, J.R. Kirtley and K.A. Moler**; Rev. Sci. Instrum. 72, 4153 (2001)

[9] **S.A. Gudoshnikov, Y.V. Deguzhnika, P.E. Rudenchik, Y.S. Sitnov, S.I. Bondarenko, A.A. Shablo, P.P. Psvlov, O.V. Snigirev and P. Seidel** ; IEEE Trans. Appl. Supercond. 11, 219 (2001)

[10] **S.A. Gudoshnikov, S.A. Liubimov, B.Y. Matveets, L.V. Mikhailenko, A.P. Deryuzhkina, Y.V. Sitnov and O.V. Snigirev**; Phys. C 368, 66 (2002)

[11] T**. Nagaishi, K. Minamimura and H. Itozaki**, IEEE Trans. Appl. Supercond. 11, 226 (2001)

[12] **E.F. Fleet, S. Chatraphorn, F.C. Wellstood, L.A. Knauss and T.M. Eiles**; Rev. Sci. Instrum. 72, 3281 (2001)

[13] **R.H. Koch, J.R. Rozen, P. Wöltgens, T. Picunko, W.J. Goss, D. Gambrell, D. Lathrop, R. Wiegert and D. Overway**; Rev. Sci. Intrum. 67, 2698 (1996)

[14] **C.D. Tesche and J. Clarke**, J. Low. Temp. Phys. 29, 301 (1977)

[15] **S.K. Tolpygo**, Hypres Niobium Integrated Circuit Fabrication Design Rules, Revision 23 (2006)

[16] "Piezo University", www.physikinstumente.com

[17] Attocube Systems product Catalog 2004 – 2005, Attocube Systems AG, Muenchen Germany (2005)

Chapter 5
Scanning SQUID Microscopy: Measurements

In this chapter measurements performed with the sensors and scanning SQUID microscopy systems described in the previous chapter will be discussed. Apart from the individual relevance of the different experiments, the aim of the results presented here is also to showcase the magnetic flux imaging capabilities of SQUID microscopy.

In the first section of this chapter, measurements on Abrikosov vortices in thin YBCO films will be described. These structures form ideal calibration sources because the relatively large and quantized flux is confined to a very small area. Furthermore, they appear naturally in any type II superconducting film which is cooled down to below its transition temperature (T_c) in a small background field. In the second section SSM experiments on superconducting structures, in which fractional flux quanta can exist, are described. For these experiments the unprecedented magnetic sensitivity of SSM proves essential.

One of the main advantages of the linear actuator based IBM SSM setup is the relatively large scan–range of up to 5 x 5 squared millimeters. Based on this specification, measurements of the magnetic flux above relatively large circuit areas can be performed. In the third section an example of such a type of experiment on Rapid Single Flux Quantum (RSFQ) circuitry developed at Hypres Inc. is described. One of the main practical issues concerning the implementation of such circuits is the trapping of magnetic flux during cooldown and subsequent operation. On the described RSFQ samples, structures have been implemented in which flux is selectively trapped away from sample areas containing the circuit elements. This controlled implantation can be monitored quite effectively over large distances using a SQUID microscope.

The increased spatial resolution resulting from the application of FIB defined pick–up loops is showcased in the fourth section. In this paragraph the current through a looped Carbon nanotube is imaged. The next section of this chapter is devoted to test measurements performed on the piezo–based scanning SQUID microscopy setup. This microscope should allow for high–resolution images given the small and accurate step sizes. The chapter is concluded with an outlook on the application of nanobridge based SQUIDs in SSM systems and a summary.

5.1 SSM measurements of Abrikosov vortices

As discussed in the introduction to this chapter, SSM measurements of thin film Abrikosov vortices provide good means to characterize the spatial resolution of the experimental setup. Apart from the dependence on the effective area of the sensor, this resolution is also determined by the position of the sensor relative to the SQUID during measurements. This should be taken into account when interpreting the results of such measurements, for experiments with the same sensor in a different sample to sensor geometry can result in distinctly different images of the vortex field. In figure 5 - 1 two images (200 x 200 μm^2) of Abrikosov vortices in a YBCO film at $T = 4.2$ K are shown.

For moderate applied fields, the amount of vortices per unit area is directly related to the background magnetic field (perpendicular to the sample) applied during the cooling process. The background field can be tuned by applying a current (I_{coil}) through a coil mounted around the sample area. From the difference in the amount of vortices (N) in both pictures it can be estimated that, for a compensating current of approximately 0.4 mA through the coil, the background field during cooling is minimized. Measurements, resulting in 200 x 200 μm^2 pictures with no vortices, have proven this estimate to be accurate.

From one picture to the other, notable differences in the sizes and shapes of the images of the vortices displayed in figure 5 - 1 can be detected. These can be attributable to the differences between the used sensors.

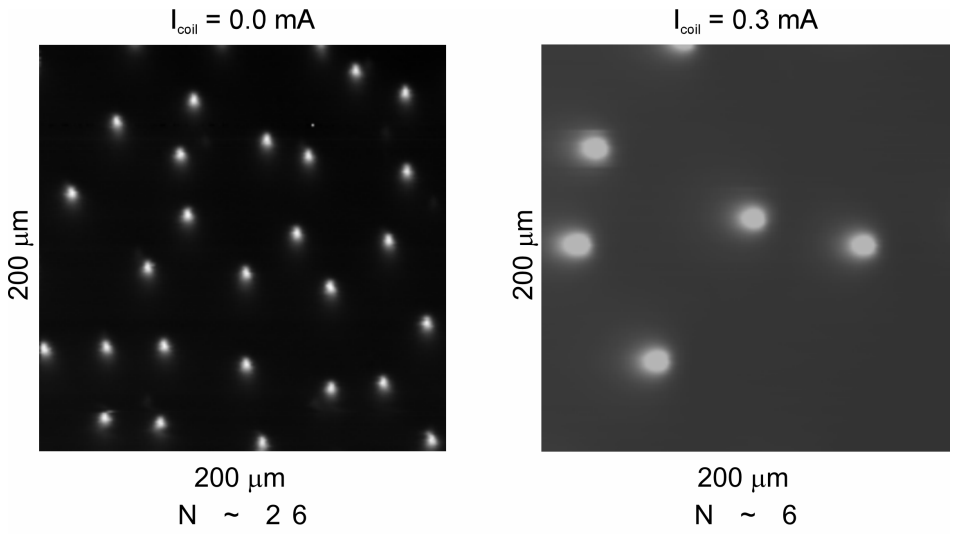

Figure 5 - 1:
Images of Abrikosov vortices in the same YBCO film at different background cooling fields with different SQUIDs and sample to sensor geometries.

For the left–hand picture (I_{coil} = 0.3 mA) an FIB–patterned pick–up loop SQUID was used (as described in chapter 4). The right–hand picture was realized using a conventional pre–fabricated pick–up loop structure with a width of 8 μm. Furthermore, the orientation of the tail–like features connected to each vortex differs from one picture to the other. This is the result of the fact that the orientation of the SQUID chip with respect to the scanning axes differs from one case to the other. In the rest of this section, experiments and calculations performed in order to describe the differences in both the shapes and sizes of applied SQUIDs and the sample to sensor geometries are described.

To quantitatively analyze the magnetic image of an Abrikosov vortex, a model incorporating the effective area of the SQUID, the sample to sensor separation and the relative scanning angle was developed by Kirtley et al. [1]. It is based on the assumption that the magnetic field of a vortex at a distance $r >> \lambda_L$ above its core is given by:

$$B(\vec{r}) = \frac{\Phi_0}{2\pi r^3}\vec{r} \tag{5.1}$$

Because the effective London penetration depth of a YBCO film at $T = 4.2$ K is typically in the order of 200 – 300 nm and the sensor to sample separation in the order of microns, it is presumed that this equation can be applied to describe the magnetic field, produced by an underlying Abrikosov vortex, at the location of the SQUID sensor.

To estimate the flux coupling into a superconducting loop with radius r_0, centered at a height h_0 above a vortex, a radial dependence of the flux is assumed. By comparing the loop area to the total area of a sphere which is intersected by this loop at a height h_0 in such a way that $h_0^2 + r_0^2 = r_{sphere}^2$, the flux through the superconducting loop can be calculated with the following equation:

$$\Phi_{loop} = \Phi_0 \left(1 - \frac{1}{\sqrt{1 + \left(\frac{r_0}{h}\right)^2}} \right) \tag{5.2}$$

The numerical integration of this equation using the sensor geometry, height and angle relative to the sample, yields the model for the expected measured flux as a function of the SQUID position. In figure 5 - 2 the measured and modeled cross–sections of the flux (Φ_s) above a vortex for two different pick–up loop configurations are shown. Because the pick–up loop geometry is not symmetric with respect to the scan directions, it is relevant to distinguish between the two scanning directions:

- The x–direction is in parallel to the leads connecting the pick–up loop with the SQUID washer. Because of this configuration, a tail appears in the vortex cross–section in this direction. This results from flux focusing due to these superconducting leads into the pick–up loop. The dimensions of the superconducting part accounting for this focusing effect are labeled as "part 2" in the figure.
- The y–direction is at a 90 degree angle with respect to the leads connecting the pick–up loop with the SQUID washer. No tail effect is expected because the pick–up loop is assumed to be symmetric with respect to this scanning direction.

From figure 5 - 2 it can be concluded that accurate fits of the measured data can be obtained for both pick–up loop configurations. The determined values of the fit–parameters (the "*height*" of the center of the pick–up loop above and the "*angle*" of the SQUID chip with respect to the YBCO film) are plausible.

Typical scanning *angles* are estimated to be about 10°, resulting in calculated *heights* in the order of a micron if the border of the pick–up loop is located precisely at the edge of the substrate. For the FIB patterned geometry, flux focusing into the pick–up loop was reduced by the creation of several interstices in the leads of the pick–up loop, effectively reducing its area. This accounts for the smaller tails observed in the measured x–direction vortex cross–section. To incorporate the patterned interstices in the simulation, the area of the second part of the pick–up loop structure was reduced by 50%.

A quantitative characterization of the resolving power of the measurements discussed above can be based on the Rayleigh criterion. In optics, the Rayleigh criterion is commonly applied to determine the minimum needed separation between two diffraction peaks in order to resolve them [2]. The intensity between the two peaks should fall off to 81% of the maximum value. The same type of criterion can be applied to describe the spatial resolution when measuring Abrikosov vortices with an SSM system. Based on this method, a resolution of 11.2 μm was reported by Kirtley et al. [1] for measurements conducted with a predefined 10 μm wide pick–up loop at a 20° angle to the sample.

In figure 5 - 3 the y–direction measurements, as displayed in figure 5 - 2, are shown together with a copy of the data, which was shifted with respect to the position axis in such a way that the drop between the two peaks is exactly 19% of the peak value. From this figure it can be concluded that, based on the Rayleigh criterion, the spatial resolution of the 8 μm wide (outer diameter) pick–up loop, scanned at a height of 2 μm above and an angle of 10° with respect to the sample, is approximately 6 μm. This corresponds to the effective diameter of the pick–up loop structure.

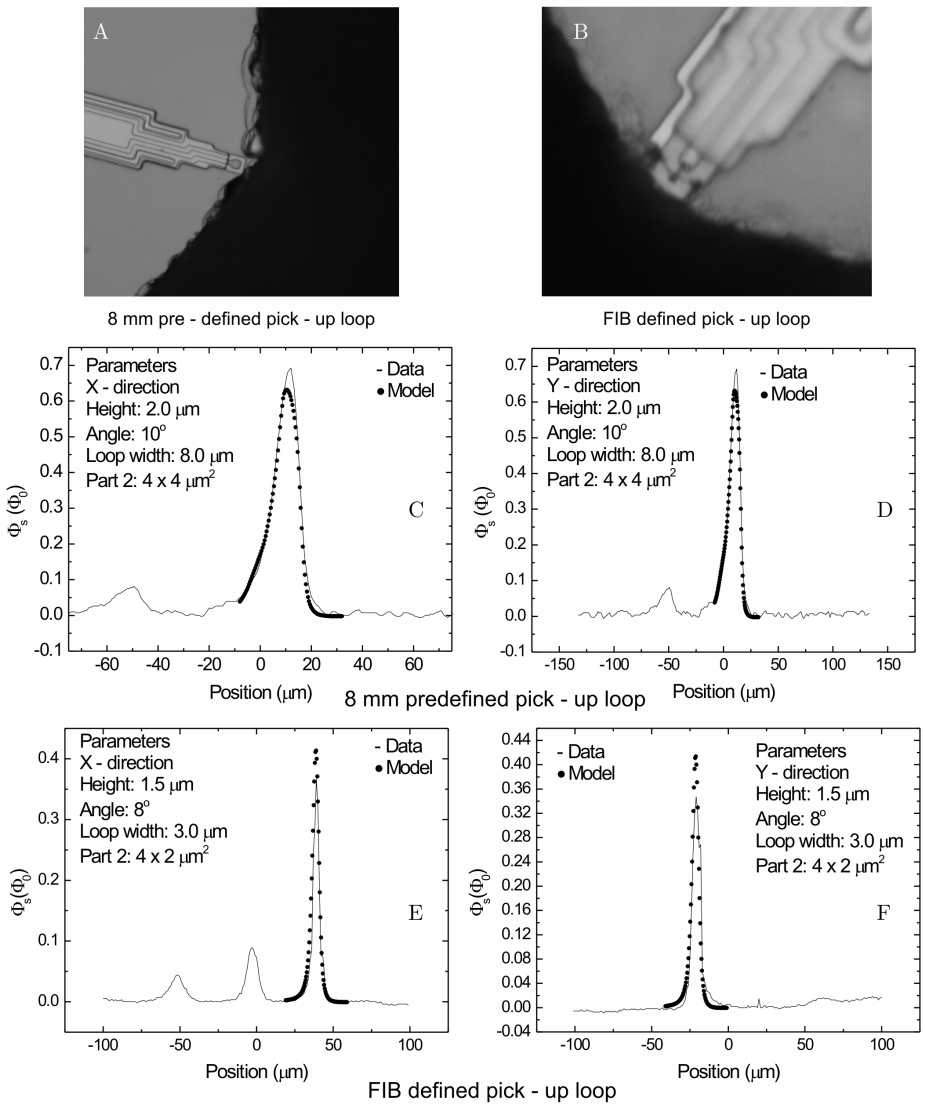

Figure 5 - 2:

Measured and modeled vortex flux cross-sections for two different SQUIDs and two different scan orientations with respect to the pick–up loop orientation (x = in parallel, y = at 90 degree angle). The FIB patterned sensor clearly yields a higher spatial resolution.

Note should be taken that the effective area of the sensor in this setup is larger. This latter value is characterized by the size of an imaged vortex, as will be discussed later in this section. The determined spatial resolution for the FIB patterned pick–up loop SQUID (*height* = 1.5 μm, *angle* = 8°), is estimated to be 3 μm, which could well correspond with its effective diameter.

A comparison of the effective areas (A_{eff}) of different pick–up loop geometries at set *heights* and *angles* can be based on the calculation of the integrated measured flux as a function of the scanned area, with the center of integration located in the middle of the image of a vortex. If the measured flux for areas away from a vortex is set to zero, the total integrated flux should become area–independent for areas that are larger than A_{eff}. This constant integral value, which should equal Φ_0 x A_{eff}, is a measure for the effective area of the SQUID during operation. The results of such a calculation for the measurement of an Abrikosov vortex with the FIB patterned pick–up loop geometry shown in figure 5 - 2, are shown in figure 5 - 4 (A). From this figure an estimated effective sensor area of 17.5 μm^2 is determined.

The determined total integrated flux does not appear to level out to a constant value for large areas. This can be caused by the presence of a residual SQUID signal in sample areas with no vortices. In part (B) of figure 5 - 4 a similar calculation is shown for measurements performed at a *height* of 3.5 μm and an angle of 10° with the pick–up loop geometry depicted in part (C) . The larger scanning height of this sensor compared to the one shown in figure 5 - 2 (B) is attributable to the fact that the latter pick–up loop is positioned closer to the substrate edge.

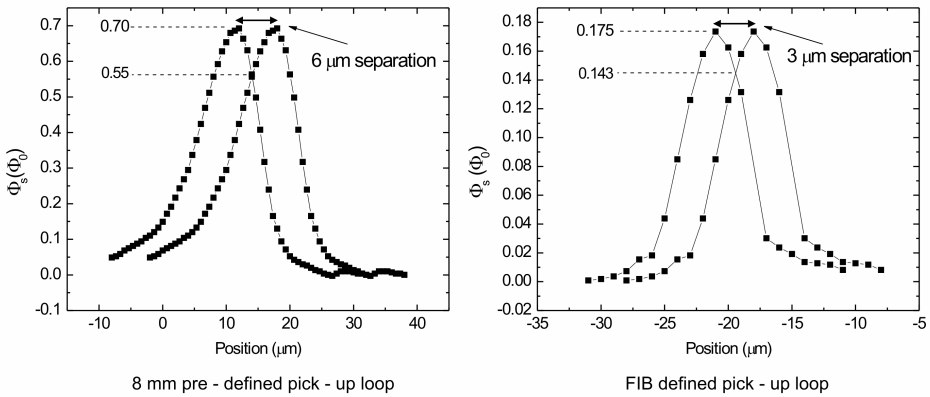

Figure 5 - 3:
Spatial resolution based on the Rayleigh criterion (19% drop–off between peaks) of the two sensor–sample configurations described in figure 5 - 2. Based on this graph, the resolution of the FIB patterned sensor is twice as high as is the case for the predefined pick – up loop.

Even though one would expect that, based on the larger sensor to sample separation, the effective area of the second pick–up loop (figure 5 - 4 (B) & (C)) would be larger, a measured value of 7 μm^2 was determined. This is the smallest effective area achieved using the FIB patterned pick–up loop type SQUIDs. A possible explanation for the low value is that, due to positioning relative to the sample, the coupling of flux into the pick up loop is not efficient. This could be caused, for instance, by a misalignment (tilt) of the SQUID chip relative to the YBCO film, which would cause a decrease of the aspect area of the pick–up loop relative to the film. This explanation is supported by the fact that during the measurements of a single vortex with this specific geometry a maximum flux of only 0.08 Φ_0 was measured. Due to the unprecedented magnetic sensitivity of SQUIDs, however, such a low coupling factor still yields significant signals.

In conclusion, it was shown in this section that, depending on the respective pick–up loop geometry and relative orientation to the sample, flux patterns spaced a few microns apart can be resolved. By optimizing the alignment of the sensor to the specific experiment, effective sensor areas smaller than 10 μm^2 can be achieved.

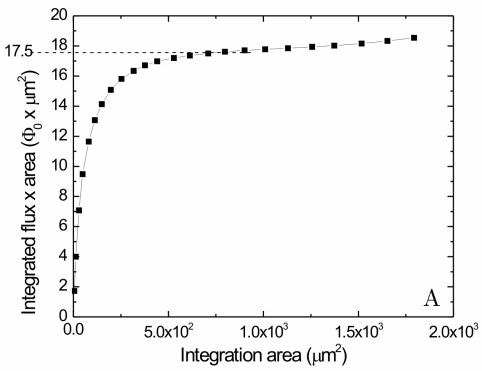

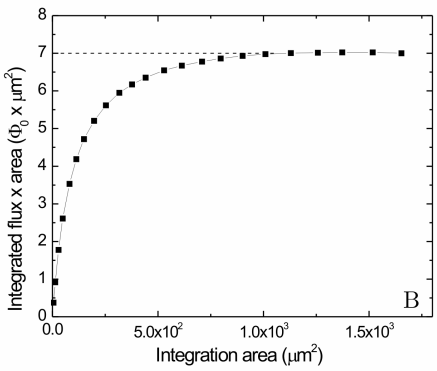

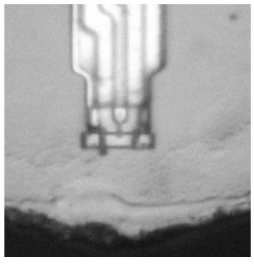

Simulated scan - parameters for the results shown in part B:

Height:	3.5 μm
Angle:	10°
Loop diameter:	2.9 μm

Figure 5 - 4:
Integrated flux as a function of integration area for two FIB defined pick–up loop geometries.
(A) Corresponding to the sensor described in figure 5 - 2.
(B) Corresponding to the sensor shown in (C).

All the results presented in this section are based on measurements of Abrikosov vortices in thin YBCO films at $T = 4.2$ K. These structures have typical diameters of hundreds of nanometers, which is still a lot smaller than the characteristic dimensions of the used pick–up loops.

The minimum achievable effective area of FIB patterned pick-up loop sensors similar to the ones described above will be limited by the limitations posed by the Hypres design rules. Even with an ideal patterning source, capable of creating structures with sub-nanometer dimensions, minimization of the pick-up loop effective area will be limited by flux focusing and the fact that the structure is covered by a thick layer of insulator. It should be noted, however, that, in practice, nanometer-sized pick-up loops will be of no use since the flux coupling from the sample into such structures will be very low. By redesigning the surrounding sample areas and predefined structures and utilizing an FIB system with a significantly smaller bundle width, the eventual sensor effective area should be reducible to 1 μm^2 or less. Given the proper sample and a small sensor to sample separation, such sensors would yield significant improvements of the spatial resolution during SSM operation.

In the next section some measurements on spontaneous fractional flux quanta, with characteristic dimensions of several microns, will be described. For these measurements minimization of the effective pick–up loop area plays a more important role than for the measurements described in this section. This results from the fact that the characteristic sizes of both the sensors and vortices are of the same order.

5.2 Imaging of fractional flux quanta

In Josephson tunnel junctions magnetic flux can penetrate in the form of Josephson vortices, which are formed in the tunnel barrier. In contrast to Abrikosov vortices, these structures have no normal core. The radius over which the superconducting phase varies, the characteristic dimension of the Josephson vortex core, is determined by the Josephson penetration depth (λ_j):

$$\lambda_j = \sqrt{\frac{h}{2\pi\mu_0 J_c (d + \lambda_1 + \lambda_2)}} \tag{5.3}$$

In this equation μ_0 is the magnetic constant of free space ($= 4\pi \times 10^{-7}$ N/A^2), J_c is the critical current density of the junction, d is the barrier thickness and λ_1 and λ_2 are the effective London penetration depths of the respective electrodes. The magnetic flux in these vortices is quantized in units of Φ_0, as is the case with Abrikosov vortices.

An interesting situation occurs in junctions with an intrinsic phase shift of the superconducting order parameter. Based on the order parameter symmetry, a "built–in" phase–shift of π can be created in structures based on a combination of the $d_{x^2-y^2}$–wave superconductor YBCO and the *s*–wave superconductor Niobium. In long Josephson junctions ($l >> \lambda_j$, with l the length of the junction) with a built in π–phase shift, the ground state, which turns out to be doubly degenerate, is characterized by the spontaneous generation of a magnetic flux corresponding to ½ Φ_0. After the first proposals of such structures [3,4,5], the existence of these "half flux quanta" was experimentally proven by means of scanning SQUID microscopy in 1994 [6]. Since then a lot of research based on such structures, for instance aimed at the investigation of the order parameter symmetry of high–temperature superconductors (e.g. in [7,8,9]) and the realization of rapid single flux quantum (RSFQ) logic incorporating these π–junctions (e.g. in [10]), has been reported. Scanning SQUID microscopy has proven to be a valuable technique for the imaging of these fractional flux quanta. The characteristic dimensions of the order of $2\lambda_j$ (several μm for thin YBCO films) of these structures, are within the limits of SSM spatial resolution. When visualizing half flux quanta, however, it is the high magnetic sensitivity of SSM systems which allows the technique to excel in comparison to other magnetic microscopy systems.

In this section SSM measurements on a double corner junction are described. Such structures, exhibiting two coupled fractional flux quanta, have been proposed as building blocks for qubits [11]. Possible quantum behavior is expected because of the low energy barrier between the two states describing the up–down and down–up flux configurations. The junction, which is schematically shown in figure 5 - 5, consists of a double cornered ramp–type junction between a $YBa_2Cu_3O_{7-\delta}$ and a Nb electrode. The barrier layer was made of Au and $SrTiO_3$. A complete description of the design, fabrication and characterization of such junctions can be found in [12].

Avoiding the trapping of flux in the junctions during cooldown poses one of the main experimental challenges when imaging the spontaneous flux quanta in these structures. In figure 5 - 6 SSM measurements of two states in a double corner junction are shown. In part (A) a down–up state is shown. Part (B) depicts an up–down state. In the latter figure, the total flux of the up peak appears to be larger than for the down peak, which could indicate additional trapped flux in the junction.

In analogy to measurements presented in the previous section, in figure 5 - 7 the total integrated flux as a function of the integration area is shown for two different measurement sets. In part (A) the integrated fluxes corresponding to an Abrikosov vortex measured in the YBCO leads leading up to a double corner junction and a half flux quantum measured at one of the corners are shown.

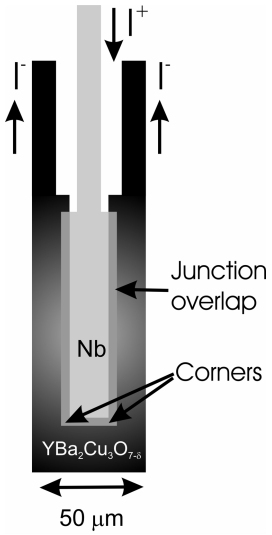

Figure 5 - 5:
Schematic of the double corner junction layout. The separation of the two corners is 20 μm, which is more than $3\lambda_j$ ($\lambda_j \approx 6$ μm).

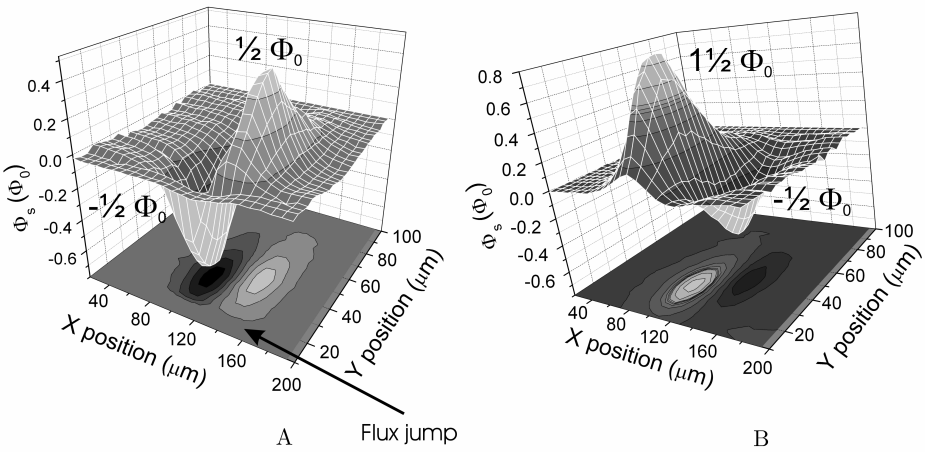

Figure 5 - 6:
(A) 3D SSM image of a down–up state in a double corner junction.
(B) 3D SSM image of an up–down state in a double corner junction, with superimposed trapped flux corresponding to 1 Φ_0.

When comparing the effective sensor area, which can be derived from the fit to the flux of an Abrikosov vortex, from this figure ($A_{eff} \approx 98$ μm^2) to values reported in the previous section ($A_{eff} < 20$ μm^2), a large discrepancy is noted. This can be attributed to the fact that a sensor with a pre–defined pick–up loop diameter of 8 microns was used. In combination with moderate alignment and sample–to–sensor separation, this could well cause the relatively large effective sensor area. Based on the integrated fluxes shown in part (B) of figure 5 - 7, it can be concluded that the total flux in the larger peak is approximately 3 times as large as the total flux in the smaller peak. This could correspond to a ratio of 1½ : -½ Φ_0.

Even though the measurements described in this section are not challenging in terms of the spatial resolution required to perform the imaging, the obtained results do illustrate the unprecedented magnetic sensitivity of the technique. If the typical area of a Josephson vortex (A_{jo}) is taken to be 10 μm^2 ($\lambda_j \approx 1.78$ μm, which is a realistic value), the peak value of the magnetic field above a half flux quantum in a corner junction would be approximately $B = 1/2\ \Phi_0/A_{jo} \approx 10^{-4}$ T. From figure 1 - 4 it can be concluded that with a magnetic force microscope the imaging of such structures would be impossible, whereas with a scanning Hall probe microscope such experiments would be performed close to limits of the magnetic sensitivity of the system. It is thus for experiments such as the ones described in this section that, in terms of sensitivity, SSM provides a true advantage compared to other magnetic imaging techniques.

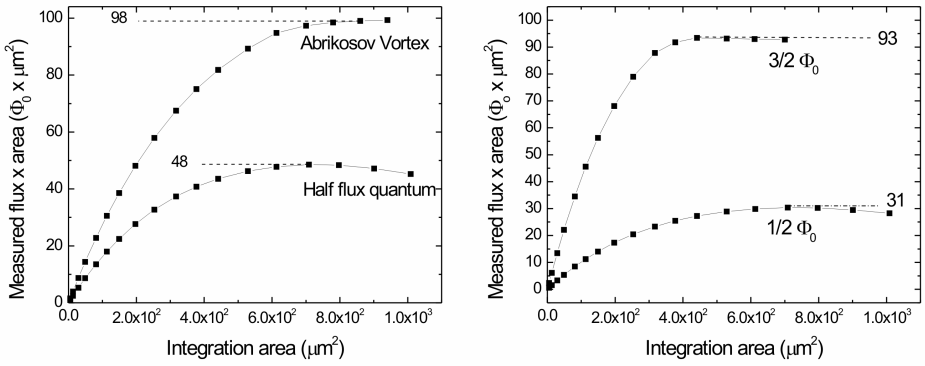

A B

Figure 5 - 7:

(A) Total integrated flux corresponding to a half flux quantum, as shown in figure 5 - 6, and an Abrikosov vortex (= 1 Φ_0) detected elsewhere on the sample.

(B) Total integrated flux corresponding to both the ½ and 1½ Φ_0 peaks shown in part B of figure 5 - 6.

5.3 Application of large scale imaging: Detection of flux trapping in RSFQ circuits

Rapid Single Flux Quantum (RSFQ) logic is a digital technology based on the high–speed switching (picoseconds) and low power dissipation exhibited by Josephson junctions [13,14]. The technique was first proposed in 1985 by Likharev, Mukhanov and Semenov [15,16]. RSFQ circuits are based on the generation, transfer and storage of single flux quanta (SFQ). Possible applications include high–speed data and signal processing in wireless and military technology and specific high–speed computation. Since the introduction of RSFQ logic several test circuits incorporating analog to digital and digital to analog conversions, transmission lines, and different pulse based logic modules based on high–temperature superconductors have been realized.

One of the main practical limitations that should be considered when designing RSFQ circuits is the trapping of magnetic flux in the superconducting loops, leads and junctions which are incorporated in the design. Since the logic in these circuits is based on the propagation of single fluxes, the existence of (similar) trapped fluxes in different parts of the structure could limit the operation. Ideally, to avoid flux trapping, the whole circuit should be cooled down to below its superconducting transition temperature at exactly zero field. In practice this is, however, impossible. To reduce the trapping of flux in active parts of the circuitry, ground plane hole structures have been proposed, which allow for the creation of selective flux trapping sites on the chip. An example of such a structure is described in [17]. In this section SSM imaging of trapped flux in an extensive RSFQ circuit (designed by O.A. Mukhanov, Hypres, Inc, Elmsformd, NY, USA.), is described. Due to intellectual property related issues, no information about the exact composition and functionality of the investigated circuits can be given. Given the purpose of the described results, this is, however, not of importance.

The described measurements serve as a showcase of the capability of the linear actuator based SSM system to scan large sample areas without any sacrifice in terms of spatial resolution. In figure 5 - 8 an SSM image, with an area of 1.6 x 1.6 mm^2, of part the RSFQ circuit is shown. In the top part of this image a part of an RSFQ circuit can be discerned. The scale bar on the left hand side of this image relates the grayscale encoding to the measured flux through the SQUID pick–up loop for each pixel. For this specific image the pixel size was 8 x 8 μm^2. Smaller pixel dimension could well have been applied, however. The only limitation in doing so is the added time it takes to complete one image.

The SSM image shown in figure 5 - 8 was taken at a cooldown field close to 0 T. Some trapped flux in the circuit can be noted. In figure 5 - 9 an SSM image of a ground-plane area on the same sample, taken at a cooling field of approximately 0.16 μT, is

shown. Several sites with trapped flux can be noted. It can thus be concluded that the applied field compensation significantly reduces the background field during cooling.

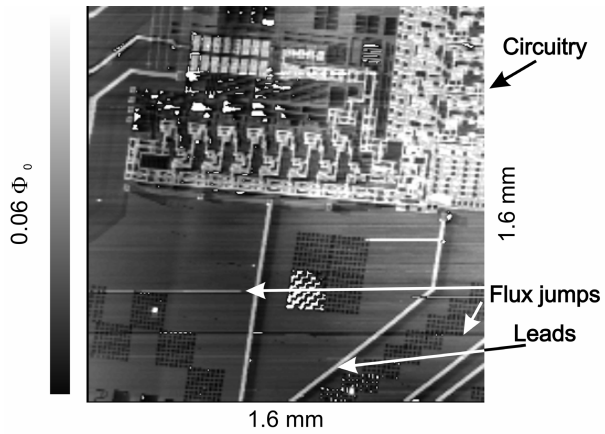

Figure 5 - 8:
1.6 x 1.6 mm^2 SSM image of an SFQ pulse based circuit. In the top part of the picture the main area of circuitry can be discerned. The bottom part of the displayed sample area consists of a superconducting ground plain, leads to the circuit elements and several test structures.

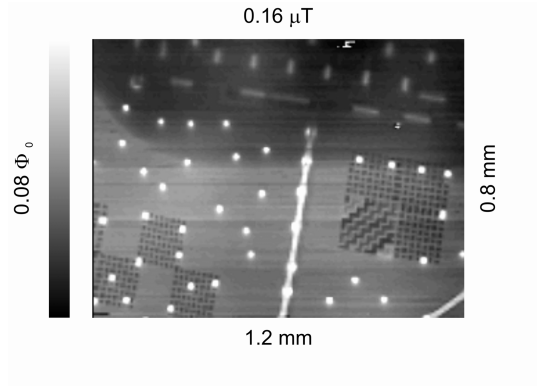

Figure 5 - 9:
1.2 x 0.8 mm^2 area of the same sample shown in figure 5 - 8, cooled at a background field of approximately 0.16 μT. Several sites with trapped flux in the superconducting ground plane can be noted. It can thus be concluded that the applied background field compensation is indeed effective.

To investigate the selective trapping of flux in different circuitry elements, zoomed in SSM images of parts of the sample were taken at different cooldown fields. An overview of three of such pictures is shown in figure 5 - 10. These images have a geometrical size of 200 x 200 μm^2 and are comprised of 2 x 2 μm^2 pixels. In the bottom parts of these images a part of the circuitry displayed in figure 5 - 8 can be discerned.

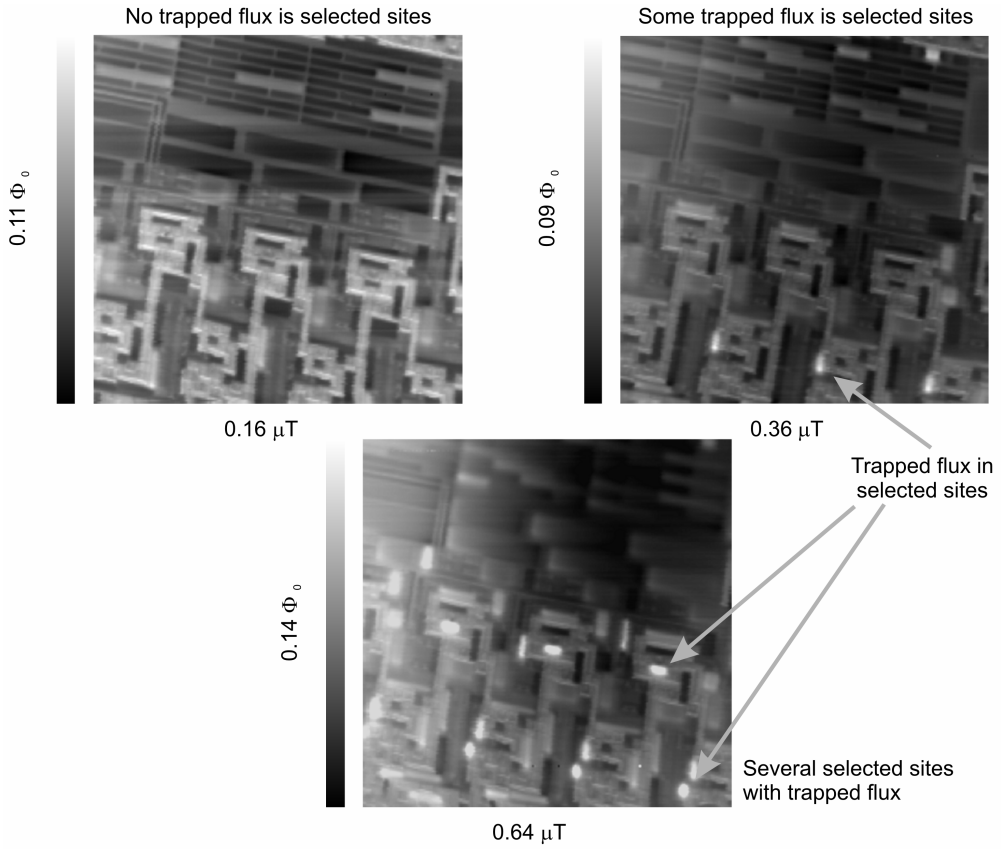

Figure 5 - 10:

Zoomed in SSM images (200 x 200 μm^2) of the sample shown in figure 5 - 8 for different values of the applied background field during cooldown. A gradual field dependent onset of flux trapped in selected pre-defined sites on the circuit can be noted. There are, however, no Abrikosov vortices trapped in the surrounding superconducting areas. This implies that, when cooling the displayed circuit in a background field, magnetic flux will be effectively and selectively trapped in predefined circuit areas.

At a background field of 0.16 μT no trapped flux can be noted in this area. When the cooling field is increased to 0.36 μT and 0.64 μT respectively, a gradual onset of trapped magnetic flux in specific predefined circuit sites can be noted. However, no trapped flux in the surrounding superconducting sample areas can be discerned. Based on this fact it can be concluded that there are indeed certain areas on the sample in which flux is selectively trapped.

The described measurements are good examples of the realizable magnetic imaging specifications of the linear actuator based SQUID microscopy system. Large scan ranges, combined with relatively small step sizes and high magnetic sensitivities allow for the detailed SSM imaging of relatively large sample areas. Typical scan ranges of conventional magnetic force microscope systems are limited to hundreds of microns. For scanning Hall probe microscopes scan sizes and resolutions comparable to the specifications of the SSM system described here have been reported [18].

In the next section experiments on the imaging of the current induced magnetic flux above a looped Carbon nanotube will be described. For these experiments both the magnetic sensitivity of the SSM technique and the increased spatial resolution provided by sensors with FIB defined pick–up loop geometries prove to be essential.

5.4 SSM imaging of the current induced magnetic flux above a looped Carbon nanotube

In this section SSM imaging of the current generated magnetic flux above a looped Carbon nanotube (CNT) is described. The aim of these experiments was to investigate the ratio of the current flowing around a loop in a CNT and the current tunneling to the next part of the CNT at the crossing right before such a loop. The described measurements were conducted with the linear actuator based SSM system while it was still at the IBM TJ Watson Research Center. The used sensors, however, consisted of FIB defined pick–up loop geometries, which were fabricated at the University of Twente. A complete description of the motivation, experimental procedures and results is given by Freitag et al. [19]. The used pick–up loop geometry is shown in figure 4 - 8 (B). In figure 5 - 11 (A) a schematic representation of the CNT layout during SSM imaging is shown. The straight lines leading away from the looped CNT represent the evaporated electrodes. Part (B) of this figure shows the measured SSM image.

Using the FIB predefined pick–up loop geometry a clear image of the current generated flux through the CNT loops is recorded. The effective pick–up area in this experiment turned out to be 12.1 μm^2. The same type of experiment, conducted with a conventional pre–fabricated pick–up loop sensor with a diameter of 4 μm, yielded results with far less definition. In this latter case the effective sensor area was too large to discern distinctive flux patterns resulting from the looped areas of the CNT. The measured flux pattern corresponds well with models of the generated flux resulting from an applied current through the CNT loop geometry. A quantitative analysis of the loop to tunnel current ration proved impossible because the signal to noise ratio during measurements was limited to approximately 2. It can thus be concluded that in terms of sensitivity no other magnetic imaging technique is applicable.

The described experiments on the looped CNT's serve as a clear illustration of an application where the added spatial resolution, resulting from the application of FIB patterned pick–up loop geometries, proves essential. However, upon inspection, the described results are clearly limited by the resolution of the system. This demonstrates the necessity for further sensor miniaturization and minimization of the sample to sensor separation. Thus, given the proper sample, the application and further development of FIB patterned pick-up loops can provide a vital improvement of the SSM imaging capabilities.

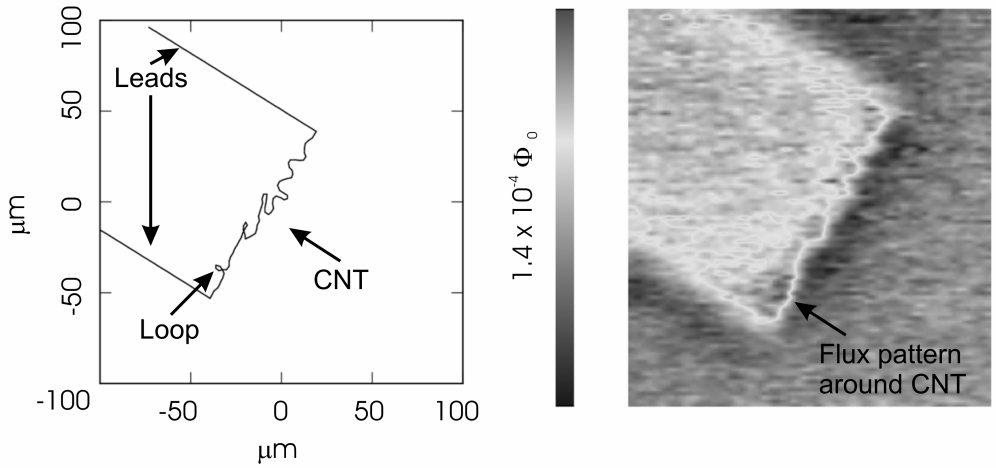

A B

Figure 5 - 11:

(A) Schematic of the nanotube layout during measurement. On the bottom left hand side a loop in the CNT can be discerned.

(B) SSM image of the area modeled in part (A).

5.5 SSM experiments with the piezo based system

In this section experiments conducted with the piezo based SSM setup, which was developed at the University of Twente, will be described. For testing purposes, one of the main practical limitations is the small scan range (≈ 30 x $30\,\mu m^2$ @ $T = 4.2$ K). A suitable test sample should thus consist of well defined magnetic structures with dimensions and relative mutual separations that are larger than the SQUID pick–up loop diameter (≈ 2 μm for the FIB patterned pick up loop used for the experiments described in this section). Furthermore, for calibration purposes, several structures should be detectable in the moderate scan range. In order to create such a sample, Nickel striplines were deposited on a SiO_x substrate through a stencil by means of pulsed laser deposition (PLD). With this technique, developed by Speets et al. [20], miniature structures can directly be deposited on a substrate.

In figure 5 - 12 (A) an atomic force microscopy (AFM) image of the realized sample is shown. Ni striplines with widths of approximately 4 μm and heights of approximately 135 nm were realized. As can also be discerned from the image, the mutual separation of the features is about 6 μm. During deposition, however, material was also deposited in between the structures, resulting in a layer with a thickness of approximately 40 nm in the interlaying gaps.

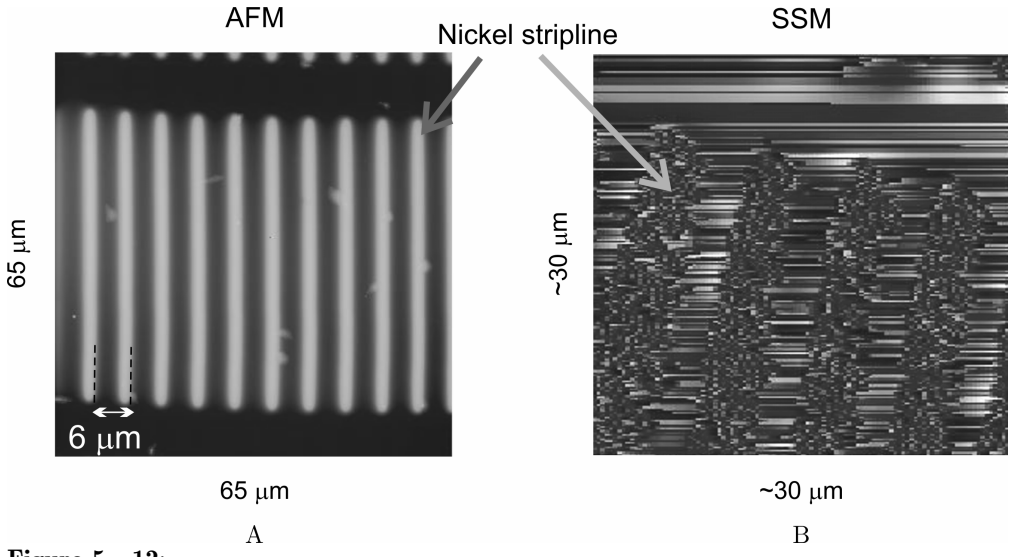

Figure 5 - 12:

(A) AFM image of the Ni striplines, deposited on a SiO_x substrate through a stencil by means of pulsed laser deposition.

(B) Measured SSM image (Grayscale range is approximately 10 Φ_0).

In part (B) of the figure the measured SSM image is shown. The grayscale range of this image is approximately 10 Φ_0. Four clear striplines can be discerned in the SSM image. Based on the measured mutual separation of 6 μm, this corresponds to a realized scan range of approximately 30 x 30 μm^2, which is in accordance with the specified characteristics of the scanning module at $T = 4.2$ K (as described in chapter 4).

In the image large line–to–line jumps in the measured SQUID output can be noticed. These result from flux jumps occurring during measurements. The reason for such unstable behavior is the fact that the magnetic field variations are relatively large. Still, however, the measured features are clearly resolvable, making the result suitable as a first test experiment. It can thus be concluded that a first successful SSM measurement was conducted with the piezo based setup.

For comparison, the flux profiles above Abrikosov vortices were also imaged with the piezo based SSM system. In figure 5 - 13 (A) the flux profile corresponding to a measured vortex in a thin film of YBCO at $T = 4.2$ K is shown. The used FIB patterned sensor was very similar to the ones described before for vortex measurements in the linear actuator based system. Because of the limited scan range (≈ 30 x 30 μm^2), no estimates of the background field during cooling can be given. This would require the observation of several vortices over a known area.

Parts (B) and (C) of the figure depict the measured and modeled cross-sections through the vortex flux pattern. From the displayed cross-sections it can be concluded that the images resemble the results obtained with the linear actuator system. As described in the figure, typical values of a couple of microns were determined for both the sample to sensor separation during measurement and the diameter of the pick-up loop. From this it can be concluded that, indeed, for both systems, the spatial resolution is limited by these parameters.

As described before in this thesis, it should be noted that the piezo based SSM setup was developed based on the future application of sub–micron sized SQUIDs. It is not until such sensors become available that the system can be used to its full potential in terms of the spatial resolution. The experiments described in this section, however, serve as a proof of functionality and thus as evidence of the successful development and testing of the system. In the next section an outlook on the possible application of miniature nanobridge based SQUIDs as SSM sensors will be given.

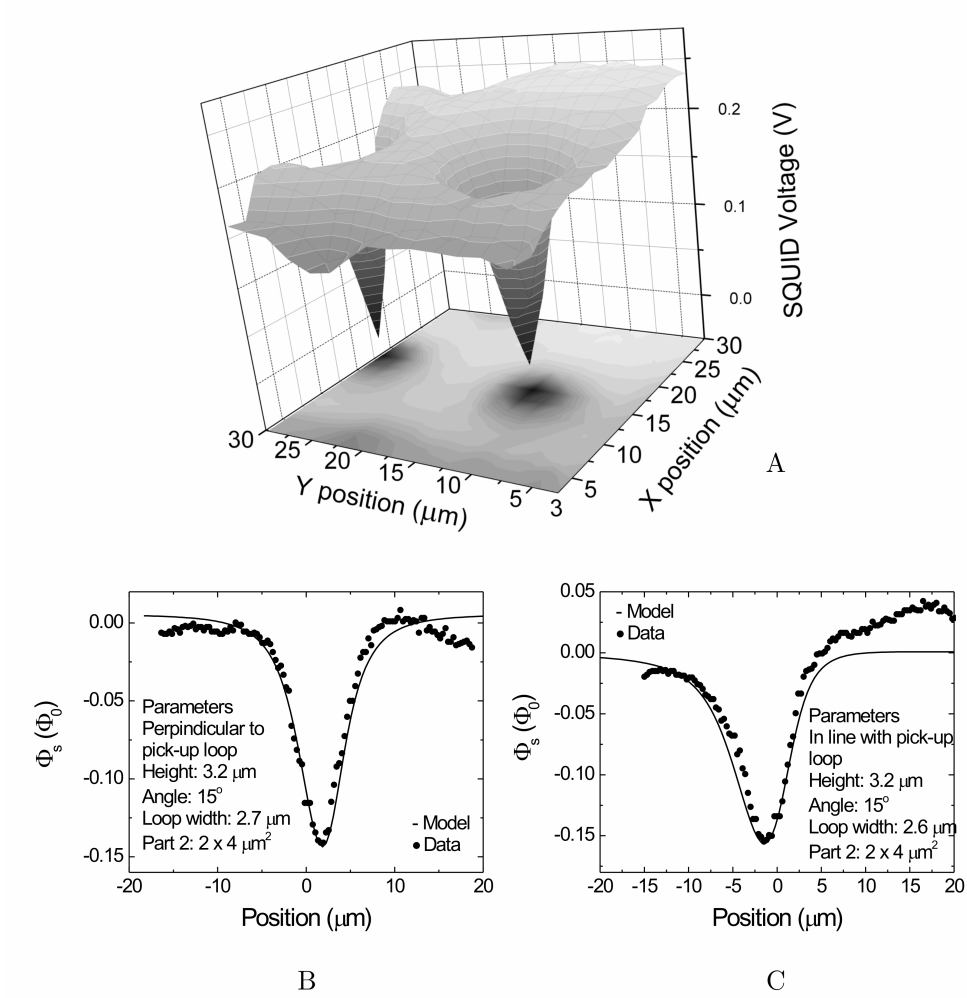

Figure 5 - 13:

(A) Image of a vortex in a thin YBCO film taken at T = 4.2 K in the piezo based SSM system.

(B) Measured and modeled vortex cross-section in the direction perpendicular to the pick-up loop orientation.

(C) Measured and modeled vortex cross-section in-line with the pick-up loop orientation.

5.6 Perspectives on the application of miniature nanobridge based SQUIDs in an SSM setup

As described in the introductory chapter to this thesis, one of the possible applications of miniaturized SQUIDs is in scanning SQUID microscopy. Application of devices such as the ones presented in chapter 3 could offer significant improvements in terms of spatial resolution. There are, however, several technical limitations one needs to take into account when applying these devices in an SSM setup. In this section some perspectives on the application of miniaturized nanobridge–based SSM sensors will be described.

Open loop operation

The simplest configuration in which a miniature SQUID can be applied as a sensor in an SSM system is in an open loop configuration. Such a setup, which is realized by biasing the SQUID in its most sensitive V-Φ point and measuring the voltage response, is limited by the fact that the output is non–linear and limited to input signals of $\Phi < \frac{1}{2}\,\Phi_0$. If such a configuration would be applied, the interpretation of measurements should take into account that large fluxes (or flux jumps during measurements) will not be noted due to the periodicity of the SQUID output.

Miniature nanobridge SQUIDs in an FLL setup

The main limitation of operating a miniature SQUID in an FLL setup is the coupling of flux into the SQUID washer for feedback purposes. To allow for complete control during operation, a coupling of several Φ_0 should be achieved. The simplest way to realize such a configuration is by patterning a current line lying adjacent to the SQUID washer in the same layer as the sensor itself. This is schematically shown in figure 5 - 14 (A). In part (B) a realized device with a hole size of approximately 1 μm^2 is shown. The resulting V-Φ oscillations are shown in part (C). To obtain this picture a current of approximately 25 mA was applied through the current line. This corresponds to the critical current of the stripline. For larger currents local heating effects appeared to considerably affect the SQUID response.

The magnetic field produced by a current (I) through a long straight wire at a distance d from the center of the wire can be described by [21]:

$$B = \frac{\mu_0 I}{2hd} \tag{5.4}$$

If the center of the SQUID washer is located at this distance d from the current line, the flux coupled to the SQUID is given by:

$$\Phi_{squid} = \frac{\mu_0 I A_{eff}}{2\pi d} \tag{5.5}$$

For a sensor with an effective area of 1 μm^2, an applied current of 25 mA and a separation of the centers of the current line and the washer of approximately 1 μm, the applied flux would be approximately 2.5 Φ_0. This is of the same order as the measured coupling for the configuration shown in figure 5 - 14. Increasing the current line width, and thus its critical current, does not necessarily result in a larger applied flux, since the effective separation from the SQUID will also increase.

From the experiment described above it can be concluded that a single film solution for the flux modulation of a miniature SQUID is not easily feasible. For a relatively large device ($A_{eff} \approx 1$ μm^2) a modulation of only a couple of Φ_0 can be realized. A possible solution for this is the development of a multilayer device with a nanobridge based SQUID overlaying a multi–turn field input coil. The realization of such a sensor would be hindered by the fact that the SQUID washer should be located exactly at the edge of the substrate. Furthermore, the alignment issues which play an important role when creating multi-layer devices will affect the minimum feature sizes. In all probability this will thus also limit the eventual SQUID size.

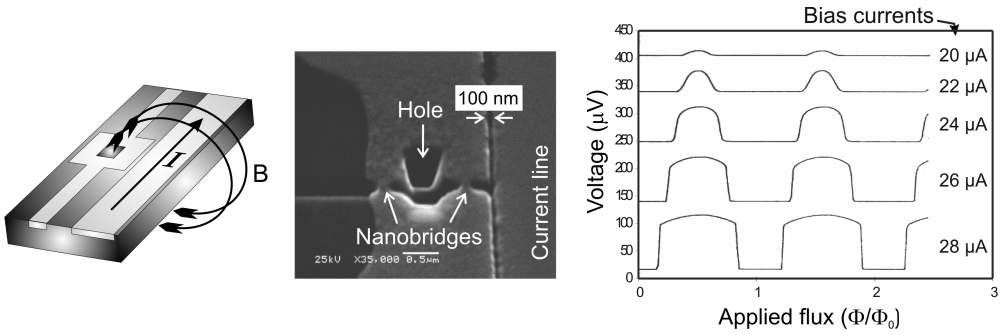

A B C

Figure 5 - 14:

(A) Schematic of a SQUID which is inductively coupled to an adjacent current line.

(B) SEM image of a realized device with a patterned hole size of 1 μm^2.

(C) Measured V-Φ characteristic.

Up until now, the possible effects on a sample of a feedback circuit located close to the pick–up area of the SQUID have not been considered. To optimally use the small effective area of miniaturized SQUIDs, the sample to sensor separation during SSM operation should be reduced to below 1 μm. For a configuration such as the one described in figure 5 - 14, this would imply that the flux from the modulation field near the sample would also be in the order of a couple of Φ_0. Since, for the experiments described in this chapter, typical fluxes of less that 1 Φ_0 were measured, this would result in a severe cross–influence from the SQUID read–out circuit on the sample. To overcome this, a pick–up loop geometry, with which the SQUID washer (and thus also the modulation coil) is separated from the sensor area (which is sensitive to flux from the sample), could be applied. Such a configuration will be described next.

SSM sensors based on superconducting (Niobium) nanobridges

In preceding parts of this thesis FIB patterned pick–up loops were described. The sizes of these structures, which are patterned in conventional SSM sensors fabricated at Hypres inc., are limited by the minimum feature sizes and layer to layer separations as determined by the fabrication process. In principle, further miniaturization can be achieved if the design of the pre–fabricated samples is optimized to the FIB patterning process.

A simpler approach to the development of SQUIDs with smaller FIB patterned pick–up loop geometries is the realization of such devices from a single Niobium layer. Due to the simplicity of the fabrication technique, superconducting nanobridges would be suitable replacements for multi-layer tunnel junctions. A proposal for a pick–up loop device based on Niobium nanobridges is given in figure 5 - 15. The SQUID washer simply consists of a relatively large superconducting loop interrupted by two nanobridges. Incorporated in the same layer is a current line which can be used to apply a modulating flux to the washer. Due to the relatively large size of this washer, a coupling of several Φ_0 can easily be realized.

The pick–up loop itself is realized by selectively patterning through areas of an overlying superconducting shielding layer. Following the deposition of an insulating interlayer, this shielding layer is deposited over the pick–up loop and the leads to the SQUID washer. In principle, such a top–shielding layer could also be incorporated in Hypres–made samples. For simplicity and testing purposes, however, a nanobridge based sensor such as the one discussed here, could be of preference. Furthermore, accurate FIB patterning on Hypres made samples is limited by the fact that there are several thick insulation layers separating the different superconducting films.

In principle sensors based on the design described above should have miniature effective areas. Flux focusing should be significantly reducible by the realization of several interstices around the pick–up hole. This approach is preferred above the

miniaturization of the complete superconducting area because, given the long duration of the latter process, drift during patterning would be of great influence on the eventual device geometry. This would then limit the minimum achievable sensor size. Ideally, the effective hole size could be miniaturized to dimensions comparable to the diameter of the ion beam by the definition of numerous well placed interstices.

In conclusion, in this section some perspectives on the application of miniature nanobridge based SQUIDs in scanning SQUID microscope systems were described. The direct application of nanoSQUIDs is limited by the incorporation of a modulation coil on the sample. A possible alternative to such devices would be a pick–up loop, nanobridge based SQUID.

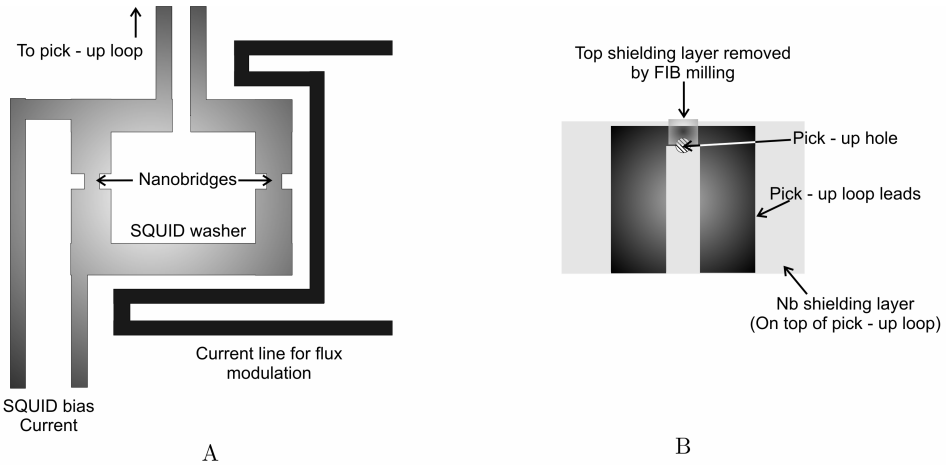

Figure 5 - 15:

Schematic layout of a possible SSM sensor based on Nb nanobridges.

(A) SQUID washer area with nanobridges and current line for flux modulation.

(B) Pick–up loop area with top shielding layer.

The whole sensor geometry (excluding the shielding and insulating layers) could in principle be fabricated out of 1 layer.

5.7 Summary

In this chapter several test experiments conducted with scanning SQUID microscopes (SSM) were described. Measurements on Abrikosov vortices in thin YBCO films were discussed in the first section. Due to their small sizes and relatively large, local and quantized magnetic flux, such vortices are very suitable calibration sources for SSM systems. The described measurements were performed with the linear actuator based SSM, developed at IBM Yorktown Heights.

In the second section, the imaging of fractional flux quanta, which can spontaneously appear in junctions between a high temperature and low temperature superconductor, were described. These experiments illustrate the high magnetic sensitivity of the technique. The capability to measure over large scan ranges without a decrease of (spatial) resolution was showcased by the imaging of rapid single flux quantum circuits, as described in the third section. In the fourth section the magnetic image of the current through a looped Carbon nanotube was discussed. The quality of the described images results from the increased spatial resolution obtained from the application of FIB patterned pick–up loop sensors.

Apart from measurements conducted with the linear actuator based system, also experiments with the in–house built piezo based SSM system were conducted. The results were described in the fifth section.

Finally, in the last section of this chapter, perspectives on the application of nanobridge–based SQUIDs in an SSM setup are discussed. It turns out that the direct application of a miniaturized nanobridge based SQUID is hindered by the necessity to apply a feedback field during measurements. This could be overcome by the development of nanobridge based pick–up loop sensors.

Bibliography

[1] **J.R. Kirtley, M.B. Ketchen, C.C. Tsuei, J.Z. Sun, W.J. Gallagher, L.S. Yu-Jahnes, A. Gupta, K.G. Stawiasz and S.J. Wind**; Appl. Phys. Lett. 66, 1138 (1995)

[2] **E. Hecht**; Optics, 4ᵉ edition, Addison Wesly Longman Inc. (2002): USA

[3] **V.B. Geshkenbein and A.I. Larkin**; JETP Lett. 43, 395 (1986)

[4] **V.B Geshkenbein, A.I. Larkin and A. Barone**; Phys. Rev. B 36, 235 (1987)

[5] **M. Sigrist and T.M. Rice**; J. Phys. Soc. Jpn. 61, 4283 (1992)

[6] **C.C. Tsuei, J.R. Kirtley, C.C. Chi, L.S. Yu-jahnes, A. Gupta, T. Shaw, J.Z. Sun and M.B. Ketchen**; Phys. Rev. Lett. 73, 593 (1994)

[7] **H. Hilgenkamp, Ariando, H.J.H. Smilde, D.H.A. Blank, G. Rijnders, H. Rogalla, J.R. Kirtley and C.C. Tsuei**; Nature 422, 50 (2003)

[8] **J.R. Kirtley, C.C. Tsuei, Ariando, C.J.M. Verwijs, S. Harkema, H. Hilgenkamp**; Nature Phys. 2, 190 (2006)

[9] **C.C. Tsuei and J.R. Kirtley**; Rev. Mod. Phys. 72, 969 (2000)

[10] **T. Ortlepp, Ariando, O. Mielke, C.J.M Verwijs, K.F.K. Foo, H. Rogalla, H.F. Uhlmann, H. Hilgenkamp**; Science 312, 1495 (2006)

[11] **E. Goldobin, K. Vogel, O. Crasser, R. Walser, W.P. Schleich, D. Koelle and R. Kleiner**; Phys. Rev. B 72, 054527 (2004)

[12] **J.A. Boschker**; "Manipulation and on-chip readout of fractional flux quanta", M.Sc. thesis, Faculty of Science and Technology, University of Twente, Enschede, The Netherlands, November 2006

[13] **K.K. Likharev**; New Superconducting Electronics, Kluwer, Dortrecht, The Netherlands (1993)

[14] **A.M. Kadin**; Introduction to Superconducting Cirtcuits, John Wiley & Sons, NY USA (1999)

[15] **K.K. Likharev, O.A. Mukhanov and V.K. Semenov**; SQUID'85, W. de Gruyter, Berlin, Germany (1985)

[16] **K.K. Likharev, O.A. Mukhanov and V.K. Semenov**; IEEE Trans. Magn. 23, 759 (1987)

[17] **O.A. Mukhanov**; IEEE Trans. Appl. Supercon. 3, 2578 (1993)

[18] **R.B. Dinner, M.R. Beasley and K.A. Moler**; Rev. Sci. Instrum. 76, 103702.1 (2005)

[19] **M. Freitag, J.C. Tsang, J.R. Kirtley, A. Carlsen, J. Chen, A.G.P. Troeman, H. Hilgenkamp and P. Avouris**; Nano Lett. 6, 1425 (2006)

[20] **E.A. Speets, P. te Riele, M.A.F. van den Boogaart, L.M. Doeswijk, B.J. Ravoo, G. Rijnders, J. Brugger, D.N. Reinhoudt and D.H.A. Blank**; Adv. Func. Mater., 16 1337 (2006)

[21] **D.J. Griffiths**; Introduction to Electrodynamics, Prentice Hall, USA (1999)

Chapter 6
Outlook

This chapter serves as an outlook on future research and applications based on the different topics described in this thesis.

Further miniaturization of nanobridge based SQUIDs

As was described in chapter 3 of this thesis, the smallest realized Nb nanobridge based SQUID had an effective area of 3.6 x 10^{-2} μm^2. The size of this device was limited by the dimensions of the FIB. Based on the applied patterning method and system, the fabrication of considerably smaller sensors appears to be impossible. The used FIB system has, however, a rather modest resolution (beam diameter ≈ 150 nm). State of the art systems boast beam diameters of 10 to 20 nm. Fabrication of similar devices with such a system could thus well result in far smaller SQUIDs. Given a proper design effective areas as small as 100 x 100 nm^2 should be realizable.

As an alternative patterning technique, electron beam lithography (EBL) could be considered. For EBL the realizable feature sizes are limited by the transfer of a pattern in a resist to the thin film. Broadening due to the ion etching step involved in this transfer limits minimum line widths to approximately 10 to 20 nm. With EBL, however, the serial fabrication of numerous devices is possible without having to prestructure the superconducting film. Furthermore, the ion induced damage to realized nanobridges will be small compared to the damage induced by the FIB process since considerably lower ion etching energies can be applied.

Next to miniature nanobridge based SQUIDs also small devices based on Josephson tunnel junctions could be considered. The most direct way to realize such sensors is by patterning them directly from a single predefined tunnel junction. A big advantage of these SQUIDs would be that commonly used design theories could be applied. A limitation to such a design would be that, in order to obtain quantum coherent effects in miniature junctions, large critical current densities should be achieved.

As a final note it should be stated that, since a SQUID incorporates two Josephson junctions or nanobridges in a superconducting ring, an ideal point source-like sensor will never be achieved. The sensor size will thus always be limited to the sum of the minimum achievable areas of both the junctions and the loop. Furthermore, the

reduction of this size will be limited by inevitable flux focusing from the superconducting leads connected to the SQUID.

Possible applications of miniature SQUIDs

Based on current research, one of the most interesting applications of sub–micron sized SQUIDs is for the detection of the spin–flips of clusters of magnetic atoms. As described in this thesis, several studies relating to such experiments have been reported in the literature. Since the spin sensitivity of a SQUID scales with its geometrical inductance, a reduction of the sensor area results in higher resolutions during measurements. The particles are commonly deposited inside the SQUID washer by spinning a diluted solution on a chip containing several sensors. Subsequent investigation by AFM is then applied to determine if, by chance, any suitable particle–sensor configurations were formed. A possible improvement on this "matter of chance" type of experiment would be the deposition of the particles on specific locations with an AFM or STM tip.

The application of miniature SQUIDs in a microscopy setup is limited by the realization of a suitable magnetic coupling to a feedback circuit. A possible solution to this would be the open loop operation of the sensors. Also, for the measurement of samples that are not sensitive to external magnetic fields, a feedback coil structure located close to the SQUID washer could be developed. A highly fashionable, but also functional geometry would be the realization of a sensor consisting of a miniature SQUID on, or located close to, an AFM or STM tip. With such a configuration both the topography and magnetic properties of the sample surface can be mapped. Furthermore, by utilizing the feed–back mechanism commonly applied in AFM and STM systems, accurate control on the sample to sensor separation can be achieved.

Scanning SQUID microscopy

In principle, with the described SSM systems the magnetic properties of any sample that can be cooled down to cryogenic temperatures can be probed on a micron scale. Further development could result in even higher resolutions. Interesting test samples are, for instance, expected to come from the field of novel (quantum) electronics. The mapping of flux in realized circuits or novel memory elements could well be important for the development of future devices.

Biophysics poses another field of research currently receiving a lot of attention. Unfortunately the study of most biological systems cannot be performed in cryogenic environments. For this purpose an SSM system could be developed where the sensor and sample environments are separated. Several of such systems have been realized worldwide. The main disadvantage of such a setup is that, by environmentally separating the sample from the SQUID, a lot of concessions are made in terms of spatial resolution.

The development of local cooling mechanisms for the SQUID and a thin thermally insulating layer between sensor and sample could result in an increase in the spatial resolution of such systems.

Ultimate limits on SQUID sensitivity and miniaturization

Ideally, the size of a SQUID should be optimized with respect to its prospective experimental application. For instance, the application of nanoSQUIDs in an SSM setup is only relevant if the length scales in both the measurement system and the sample are of the same order as the loop diameters of the sensors. By employing state of the art nanopatterning techniques capable of achieving line widths of tens of nanometers (FIB, EBL), in principle nanobridge-based sensors with areas of the order of 100 nm^2 should be realizable. Given the proper SSM system and sample, such devices could thus yield significant improvements in the spatial resolution of the technique.

In terms of magnetic sensitivity, reduction of the effective SQUID area does not necessarily result in an increase of the resolution. For RSJ SQUIDs with identical critical currents, the energy resolution varies as a function of the sensor inductance. Depending on the exact parameters, a decrease of the loop inductance can result in both a higher or lower energy resolution. If achieving optimal magnetic sensitivity is relevant for the experiment, this effect should be studied before determining the optimal sensor diameter. In practice this would then result in finding the best trade-off between magnetic and spatial resolution. With the exception of the measurements on the looped Carbon nanotubes, for the SSM experiments described in this thesis, however, the measured magnetic signal was far greater than the limits set by the sensitivity of the applied sensors. For such experiments thus, further miniaturization of the sensors and optimization of the measurement setup could result in vast improvements in the resolution of the technique.

SUMMARY

Recent interest in the development of small sized superconducting quantum interference devices (SQUIDs) has been motivated by the applicability of these sensors for the investigation of small, local, magnetic signals, such as the magnetization reversal of small magnetic clusters and the observation of local magnetic structures using a scanning SQUID microscope (SSM). Further miniaturization of the sensors offers a possibility to enhance the sensitivity and spatial resolution in these experiments. In the first part of this thesis the development of miniature SQUIDs based on Niobium nanobridges was described. From a fabrication point of view the realization of such devices offers less practical limitations compared to the development of miniature sensors based on "classical" Josephson tunnel junctions.

The nanobridge based SQUIDs were patterned by means of focused ion beam milling. Since the ion beam profile is inhomogeneous, structures with widths that are smaller than the beam diameter can be created by letting two beam profiles overlap. Simulations and experiments aimed towards the determination of the effects of the ion induced damage on patterned devices have proven that, in Niobium structures patterned with a 25 keV Ga focused ion beam, superconductivity is suppressed as far as 35 nm inwards from the surface at $T = 4.2$ K. This result was taken into account when modeling the dimensions of realized nanobridges.

From literature it is known that the current–phase relationship (CPR) in superconducting nanobridges is dependent on the dimensions of the structures. The CPR in short bridges ($l \leq 3.5\ \xi(T)$) is expected to be sinusoidal. The Josephson characteristics in narrow (width (w) $\leq 4.4\ \xi(T)$), longer structures are determined by one dimensional depairing of the superconducting wave function. In wider bridges the CPR results from the coherent motion of vortices across the structure. Measurements of the CPR in two Nb nanobridges have shown that, as a function of decreasing temperature, the transition from Josephson-like single-valued CPR's to multi-valued characteristics reminiscent of phase-slippage can be induced. The critical current close to the point of cross-over was approximately 12 μA for both structures. Since both intrinsic and thermal hysteresis in the current-voltage characteristic of the structure are associated with the phase-slip process, single-valued CPR's should be ensured in order to obtain non-hysteretic current-voltage characteristics.

By patterning two nanobridges in a miniature superconducting loop, SQUIDs are created. The smallest realized device has an effective area of 3.6 x 10^{-2} μm^2. Typical maximum sensitivities of 100 $\mu V/\Phi_0$ and modulation depths of up to 50 μV were measured for sensors based on Nb nanobridges with different widths. SQUIDs with critical currents

that are larger than approximately 25 μA exhibited hysteretic current–voltage characteristics. Such devices cannot be employed in a standard current–biased measurement setup. This critical current corresponds to the determined bridge critical currents close to the cross-over from 1-D depairing to Josephson-like characteristics. It can thus be concluded that the hysteresis in the current-voltage characteristics of the SQUIDs can be related to the phase-slip process in the nanobridges. No significant time–dependent degradation of patterned SQUIDs was noticed. Most devices, however, appeared to lose functionality after a certain period and/or several cooldowns. The origin of this degradation is expected to be of accidental rather than intrinsic nature.

The predictability of the characteristics of realized sensors based on the designed widths of the incorporated nanobridges turned out to be limited. This is attributed to the fact that, since the eventual bridge–widths are smaller than or comparable to the diameter of the FIB, any irregularities during patterning can result in significant differences in the shapes and sizes of realized structures. The critical current of the device appears to be a better predictor of the eventual sensor properties. To ensure that devices with certain critical currents are realized, several SQUIDs, with a spread in the designed widths of the nanobridges, are patterned per session. Even though such an approach would not allow the industrial application of the sensors, it does not inhibit small–scale experiments.

The white noise level of the flux noise spectral density of a SQUID with a critical current of 15 μA and an effective area of 900 μm^2, was determined to be approximately 1.5 $\mu\Phi_0/Hz^{1/2}$. In practice, the performance of similar measurements on miniaturized devices turned out to be limited by the small geometrical inductance of such sensors. Based on the flux noise spectral density reported above for the larger SQUID, the spin sensitivity of a sensor with an area of 3.6 x 10^{-2} μm^2 was estimated to be about 55 $\mu_B/Hz^{1/2}$. Based on this estimation, the application of such a device for the detection of small magnetic clusters would be an attractive option.

In the second part of the thesis experiments on Scanning SQUID Microscopy (SSM) systems and sensors were described. Measurements on two different SSM systems were discussed:

- SSM measurements conducted with a system based on linear actuators. The scanning motion, which is generated outside of the cryostat, is translated to the cryogenic environment via a lever principle. This system, called the IBM SSM hereafter, was developed at the IBM TJ Watson Research Center, Yorktown Heights, NY, USA.
- Experiments on a piezo–based setup, which was developed at the University of Twente. In contrast to the microscope described above, the scanning motion is generated within the cryostat.

For both systems, the principle of measurement and the applied sensors are comparable. The SSM sensors, based on the $Nb/AlO_x/Nb$ process offered by Hypres Inc., are of a pick–up loop type of geometry. In such SQUIDs, the washer area is geometrically separated from a small "pick–up area", which is incorporated in the SQUID loop. By polishing the SQUID chip, a separation between the pick–up loop and substrate edge of approximately 1 μm can be realized. During operation, the sensor is scanned in contact with and at an angle of approximately 10^o to the sample. This results in a difference in lateral separation between pick–up loop to sample and SQUID washer to sample of several hundreds of microns. In such a way it is ensured that the pick–up loop area is significantly more sensitive to the magnetic flux above the sample.

Two types of pick–up loop geometries have been employed. The dimensions of the first type, completely fabricated at Hypres, are limited by the minimum feature sizes and layer separations allowed by the design rules of the fabrication process. The smallest achievable effective pick–up loop area is approximately 4 x 4 μm^2. Further miniaturization is realized in pick–up loops of the second type. These structures, which are half–fabricated at Hypres, are patterned by means of focused ion beam milling.

In the fifth chapter several scanning SQUID microscopy experiments are described. Abrikosov vortices in thin YBCO films are very suitable calibration sources, since the relatively large field is quantized and confined to a small area. The modeling and comparison with measurements of the flux of such a vortex allows for the characterization of the realized sensor. The smallest measured pick–up loop effective area was approximately 7 μm^2. This value is largely determined by the geometry of the loop. Both the sample to sensor alignment and separation during measurements also affect the effective area of a sensor. The resolving power of different sensors can be characterized with a Rayleigh–like criterion. Based on this, structures with separations of approximately 3 μm can be resolved with the focused ion beam defined sensors. In practice, however, even smaller separations are still resolvable.

Several test experiments aimed toward showcasing the imaging possibilities of the IBM SSM have been conducted. The imaging of fractional flux quanta, which can appear naturally in Josephson π - junction configurations, is a clear example of a type of experiment which requires the unprecedented magnetic sensitivity offered by an SSM system.

One of the key specifications of the IBM SSM system is the ability to conduct measurements over large ranges (up to 5 mm), without making any sacrifices in terms of resolution. The described imaging of trapped flux in specific sample areas on a "rapid single flux quantum" (RSFQ) chip is a good example of the applicability of such scan ranges. The gain in spatial resolution, which results from the application of FIB patterned pick–up loops, was showcased by experiments on looped Carbon nanotubes. The magnetic flux due to the current loops can accurately be discerned with such sensors.

Summary

The scanning resolution in the IBM SSM is limited to steps of tens of nanometers. Furthermore, since the scanning motion is translated via a lever construction, the motion of the sensor relative to the sample is circular. For the current SSM sensors these limitations are not of importance, since the sensor size is far greater than both the minimum step size and the non–idealities in the motion path. The piezo based SSM was developed with the perspective of applying nanometer–sized sensors. Even though such sensors are not presently available, the ongoing developments in the field of nanotechnology and specifically nanopatterning, make future further miniaturization of SQUIDs likely.

As a proof of functionality, test measurements were conducted on the piezo based SSM system. The magnetic flux pattern above Nickel striplines with widths of approximately 4 μm and mutual separations of 6 μm was successfully imaged. Also flux profiles corresponding to vortices in thin YBCO films were measured. The obtained results are comparable to results of similar measurements performed in the linear actuator based SSM system. To optimally use the high spatial resolution obtained by the implementation of the piezo scanner modules, SSM sensors with even smaller effective areas should be developed. Furthermore, additional field compensation modules should be employed to allow for the imaging of field dependent flux patterns.

The research topics described in this thesis form a basis for the further development, miniaturization and application of both Niobium nanobridge based SQUIDs as well as pick-up loop based SSM sensors. The presented results on the first type of device not only showcase the realized SQUID miniaturization down to the nanoscale, but also yield significant understanding of the physical mechanisms determining the characteristics of such devices. From the overview of the SSM sensors, systems and measurements it can be concluded that state-of-the-art systems, operating at both high spatial resolutions and magnetic sensitivities, have been realized.

SAMENVATTING

(SUMMARY IN DUTCH)

De recente interesse in de ontwikkeling van geminiaturiseerde supergeleidende kwantuminterferentie detectoren (SQUIDs) wordt gemotiveerd door de toepassing van dergelijke sensoren voor onderzoek aan zwakke, lokale magnetische signalen, zoals de magnetisatieomslag van kleine magnetische clusters en de afbeelding van lokale magnetische structuren met behulp van een Scanning SQUID-Microscoop (SSM). Verdere miniaturisatie van de sensoren zou de vergroting van de gevoeligheid en ruimtelijke resolutie bij soortgelijke experimenten mogelijk maken. In het eerste deel van dit proefschrift wordt de ontwikkeling van op niobium nanobruggen gebaseerde geminiaturiseerde SQUIDs beschreven. De realisatie van dergelijke detectoren is, bezien vanuit technisch perspectief, minder complex dan de ontwikkeling van geminiaturiseerde sensoren die gebaseerd zijn op "klassieke" Josephson tunneljuncties.

De op nanobruggen gebaseerde SQUIDs zijn gestructureerd met behulp van een gefocusseerde ionenbundel (FIB). Omdat het profiel van deze bundel niet homogeen is, kunnen structuren met breedtes kleiner dan de bundeldiameter gefabriceerd worden door twee bundelprofielen te laten overlappen. Aan de hand van simulaties en experimenten is aangetoond dat de door de 25 keV Ga-ionen geïnduceerde schade aan gefabriceerde niobium structuren leidt tot een suppressie van de supergeleidende eigenschappen bij $T = 4.2$ K tot 35 nm inwaarts vanaf de rand van de structuur. Dit resultaat is meegenomen in de modellering van gerealiseerde nanobruggen.

Uit de vakliteratuur is bekend dat de stroom-fase relatie (SFR) in supergeleidende nanobruggen afhankelijk is van de afmetingen van de structuren. Verwacht wordt dat de SFR in korte bruggen (lengte (l) $\leq 3.5\ \xi(T)$, met $\xi(T)$ de temperatuurafhankelijke supergeleidende coherentielengte) sinusoïdaal is. De Josephson-karakteristieken van smalle (breedte (w) $\leq 4.4\ \xi(T)$), langere bruggen worden bepaald door eendimensionale opbreking van de supergeleidende elektronenparen. In bredere bruggen wordt de SFR bepaald door de coherente beweging van Abrikosov vortexen door de structuur. De experimentele bepaling van de SFR in twee niobium nanobruggen heeft aangetoond dat, als functie van afnemende temperatuur, de transitie van Josephson-achtige enkelwaardige SFR's naar meerwaardige karakteristieken geïnduceerd wordt. De kritische stroom nabij deze overgang bleek voor beide structuren ongeveer 12 μA te zijn. Aangezien aan het "phase-slip" proces zowel intrinsieke als thermische hysterese in de stroom-spanningskarakteristieken van de structuren gekoppeld wordt, zijn enkelwaardige SFR's noodzakelijk voor het verkrijgen van niet-hysteretische karakteristieken.

Door twee nanobruggen in een geminiaturiseerde supergeleidende ring te structureren wordt een SQUID gecreëerd. De kleinste gerealiseerde detector heeft een effectief oppervlak van 3.6 x 10^{-2} μm^2. Typische maximale gevoeligheden van 100 $\mu V/\Phi_0$ en modulatiedieptes tot 50 μV zijn gemeten voor sensoren gebaseerd op niobium nanobruggen met verschillende breedtes. SQUIDs waarvan de kritische stroom bij een temperatuur van 4.2 K meer dan ongeveer 25 μA bedroeg, bleken hysteretische stroom-spanningskarakteristieken te vertonen. Dergelijke detectoren kunnen niet worden toegepast in een conventionele stroomgestuurde meting. Deze kritische stroom komt overeen met de voor nanobruggen gemeten waarde nabij het omslagpunt van enkelwaardige naar meerwaardige SFR's. Op basis hiervan kan dus worden geconcludeerd dat de hysterese in de stroom-spanningskarakteristieken van gerealiseerde sensoren gekoppeld kan worden aan het "phase-slip" proces. Er is geen significante tijdsgerelateerde degradatie van de gerealiseerde sensoren vastgesteld. De meeste SQUIDs bleken na een bepaalde periode of na meerdere afkoel-/opwarmcylci hun functionaliteit te verliezen. Verwacht wordt dat de oorzaak van deze degradatie van toevallige, en dus niet van structurele aard, is.

Het is gebleken dat, op basis van de ontworpen breedtes van de nanobruggen, de karakteristieken van gerealiseerde SQUIDs moeilijk te voorspellen zijn. Dit kan worden geweten aan het feit dat de uiteindelijke brugbreedtes kleiner zijn dan de diameter van de gefocusseerde ionenbundel. Onregelmatigheden tijdens het structureringsproces leiden zodoende tot grote variaties in de afmetingen en vormen van de gerealiseerde nanobruggen. De kritische stroom van gerealiseerde sensoren bleek een betere indicator voor de karakteristieken van de detectoren. Om ervoor te zorgen dat tijdens het structureren SQUIDs met een bepaalde kritische stroom worden verkregen, worden er per sessie meerdere sensoren, gebaseerd op nanobruggen met verschillende breedtes, gefabriceerd. Hoewel een dergelijke aanpak niet geschikt is voor een industrieel proces, worden experimenten op een kleinere schaal hierdoor niet belemmerd.

Het witteruisniveau van de fluxruis spectrale dichtheid van een SQUID met een kritische stroom van 15 μA en een effectief oppervlak van 900 μm^2 werd bepaald op ongeveer 1.5 $\mu\Phi_0/Hz^{1/2}$. In de praktijk blijkt de uitvoering van gelijksoortige metingen op kleinere sensoren bemoeilijkt te worden door de kleine geometrische inductie van dergelijke structuren. Op basis van de hierboven vermelde waarde van de fluxruis spectrale dichtheid voor een grotere SQUID, is de spingevoeligheid van een sensor met een effectieve oppervlakte van 3.6 x 10^{-2} μm^2 afgeschat op ongeveer 55 $\mu_B/Hz^{1/2}$. Aan de hand van deze schatting kan worden gesteld dat dergelijke geminiaturiseerde sensoren aantrekkelijk zouden zijn voor metingen aan kleine magnetische clusters.

In het tweede gedeelte van dit proefschrift worden experimenten aan Scanning SQUID-Miscoscopie (SSM) systemen en sensoren beschreven. Er zijn metingen gedaan aan twee SSM-systemen:

- SSM-metingen met een systeem dat gebaseerd is op lineaire actuatoren. De scanbeweging wordt buiten de cryostaat gegenereerd en via een hefboomconstructie overgebracht naar de cryogene omgeving. Dit systeem, hierna de IBM SSM genoemd, is ontwikkeld aan het IBM T.J. Watson Research Center te Yorktown Heights, New York, Verenigde Staten.
- Een op piëzo-elementen gebaseerde opstelling. Dit systeem is ontwikkeld aan de Universiteit Twente. In tegenstelling tot de hierboven beschreven microscoop, wordt de scanbeweging in de cryostaat voortgebracht.

Voor beide systemen geldt dat het meetprincipe en de toegepaste sensoren vergelijkbaar zijn. De SSM-sensoren, die gebaseerd zijn op de door Hypres Inc. aangeboden $Nb/AlO_x/Nb$ technologie, hebben een opvangspoelgeometrie. In dergelijke SQUIDs wordt de "washer", waarin de juncties zich bevinden, geometrisch gescheiden van een aan deze "washer" gekoppelde opvangspoel. Het substraat waarop de SQUID zich bevindt wordt zo gepolijst dat de opvangspoel precies aan de rand ligt. Tijdens de meting wordt de SQUID-chip in direct contact en onder een hoek van ongeveer 10 graden met het te onderzoeken object voortbewogen. Zodoende wordt er een significant verschil in de aftsand tussen enerzijds de "washer" en het object en anderzijds de opvangspoel en ditzelfde object bewerkstelligd. Op deze manier wordt ervoor gezorgd dat de opvangspoel vele male gevoeliger is voor magnetische fluxpatronen direct boven het te onderzoeken object dan het SQUID "washer" gebied.

Er zijn twee soorten opvangspoelgeometrieën toegepast. De afmetingen van structuren van het eerste type, die volledig bij Hypres Inc. zijn gefabriceerd, worden beperkt door de door het fabricageproces bepaalde minimale afmetingen. De kleinste fabriceerbare opvangspoel van dit type had een effectief oppervlak van ongeveer 4 x 4 μm^2. Verdere miniaturisatie kan worden gerealiseerd met opvangspoelen van het tweede type. Deze structuren, die als halffabricaat door Hypres Inc. worden afgeleverd, worden met behulp van een gefocusseerde ionenbundel gerealiseerd.

In het vijfde hoofdstuk van dit proefschrift worden diverse experimenten met scanning SQUID-microscopie systemen beschreven. Abrikosov vortexen in dunne laagjes YBCO zijn ideale kalibratiestructuren, omdat de relatief grote hoeveelheid magnetische flux gekwantiseerd is en zich tot een gelimiteerd oppervlak beperkt. Aan de hand van de vergelijking van gemeten en gemodelleerde vortex fluxprofielen kan de toegepaste SSM-sensor worden gekarakteriseerd. De kleinste gemeten effectieve oppervlakte van een gerealiseerde opvangspoel bleek ongeveer 7 μm^2 te bedragen. Deze waarde wordt voornamelijk bepaald door de geometrie van de opvangspoel. De uitlijning van en de afstand tussen het te onderzoeken object en de sensor dragen hier echter ook aan bij. Het oplossend vermogen van verschillende sensoren kan worden gekarakteriseerd aan de hand van een Rayleigh-achtig criterium. Gebaseerd op een dergelijke vergelijking blijken structuren op een onderlinge afstand van 3 μm nog waarneembaar met de

opvangspoelsensoren van het tweede type. In de praktijk blijken nog kleinere structuren echter ook nog goed waarneembaar.

Er zijn diverse testexperimenten uitgevoerd met als doel het tentoonstellen van het afbeeldend vermogen van de IBM SSM. De afbeelding van halve fluxkwanta, welke op spontane wijze kunnen onstaan in Josephson π-juncties, vormt een duidelijk voorbeeld van een soort experiment waar de ongekende magnetische gevoeligheid van SSM systemen van groot belang is.

Eén van de belangrijkste eigenschappen van het IBM SSM systeem is de mogelijkheid om de magnetische eigenschappen van grote oppervlaktes (tot 5 x 5 mm^2) af te beelden zonder aan resolutie in te leveren. De beschreven metingen aan een chip met "rapid single flux quantum" (RSFQ) logica zijn wat dit betreft exemplarisch. De vergrote ruimtelijke gevoeligheid die wordt verkregen door het toepassen van de met de gefocusseerde ionenbundel gefabriceerde opvangspoelen, wordt tentoongesteld aan de hand van metingen van het fluxprofiel boven een koolstof nanobuisje.

De scanresolutie van de IBM SSM is gelimiteerd tot stapjes van tientallen nanometers. Tevens wordt de scanbeweging via een hefboomprincipe overgebracht, waardoor de relatieve beweging van de sensor ten opzichte van het te onderzoeken object cirkelvormig is. Voor de huidige generatie SSM sensoren zijn deze beperkingen niet van belang, aangezien deze detectoren een stuk groter zijn dan de minimale stapgrootte en niet ideale bewegingen. Het op piëzo-elementen gebaseerde SSM-systeem is ontwikkeld met als doel de toepassing van sensoren met typische afmetingen van tientallen tot honderden nanometers relevant te maken. Hoewel dergelijke structuren nog niet beschikbaar zijn, is het aan de hand van de huidige ontwikkelingen op het gebied van nanotechnologie, en in het bijzonder nanostructurering, te verwachten dat de verdere miniaturisatie van SQUIDs in de toekomst mogelijk zal zijn.

Om de functionaliteit van het op piëzo-elementen gebaseerde SSM systeem te bewijzen zijn diverse testexperimenten uitgevoerd. Het magnetische fluxpatroon boven dunne nikkellijntjes met typische breedtes van ongeveer 4 μm en onderlinge afstanden van 6 μm is succesvol afgebeeld. Tevens zijn de fluxprofielen van Abrikosov vortexen in een dun YBCO laagje afgebeeld. De verkregen resultaten zijn vergelijkbaar met metingen aan het IBM SSM-systeem. Om optimaal gebruik te kunnen maken van de door de toepassing van piëzomodules verkregen verhoogde ruimtelijke resolutie, zouden verder geminiaturiseerde sensoren moeten worden toegepast. Tevens zouden additionele modules ter compensatie van het magnetische achtergrondveld moeten worden ontwikkeld.

De onderwerpen die in dit proefschrift zijn beschreven vormen een gedegen basis voor de verdere ontwikkeling, miniaturisatie en toepassing van zowel op niobium nanobruggen gebaseerde SQUIDs alsmede op opvangspoelen gebaseerde SSM sensoren. De beschreven resultaten aan sensoren van het eerste type stellen niet alleen de succesvolle miniaturisatie van SQUIDs tot de nanoschaal tentoon, maar leveren ook een grote bijdrage aan het inzicht in de fysische mechanismen die de karakteristieken van dergelijke

structuren bepalen. Aan de hand van de gepresenteerde SSM-sensoren, systemen en metingen kan worden geconcludeerd dat hoogwaardige systemen, waarin hoge ruimtelijke resolutie en ongekende magnetische gevoeligheid worden gecombineerd, zijn gerealiseerd.

Dankwoord

(Acknowledgements)

Met de totstandkoming van dit proefschrift sluit ik een periode van vier jaar promotie-onderzoek af. Met veel plezier en een voldaan gevoel kijk ik terug op deze jaren. Zoals het vaak het geval is bij wetenschappelijk onderzoek, is het beschreven onderzoek het resultaat van een team effort. Hierbij dient niet alleen te worden gedacht aan de directe begeleiding, samenwerking en ondersteuning, maar ook aan zaken als collegialiteit en de geboden steun door het thuisfront. Als afsluiting van het proefschrift wens ik dan ook eenieder die hier een bijdrage aan heeft geleverd te bedanken.

Ten eerste zou ik graag Hans willen bedanken voor de aan mij geboden mogelijkheid om als promovendus aan de slag te gaan binnen de groep. Op zeer inspirerende, doch ongedwongen wijze heb jij mij de afgelopen jaren in de juiste richting gestuurd. Het getoonde vertrouwen en de geboden vrijheid weet ik ook zeer te waarderen. Ik zou dan ook liegen als ik zou zeggen dat het mij niet deert dat na een periode waarin ik onder jouw begeleiding stage-, afstudeer- en promotieonderzoek heb verricht, onze wegen zich zullen scheiden.

Grote dank gaat ook uit naar Dick en Frank. In de eerste plaats natuurlijk voor de onmisbare ondersteuning in het lab. Maar wat ook zeker genoemd dient te worden is dat ik, en met mij iedere promovendus in de groep, ter doorbreking van de dagelijkse beslommeringen altijd bij jullie terecht kon voor een praatje of geintje.

This section of the acknowledgements is written in English especially for John Kirtley. It has been a great honor to have worked with you on several occasions over the past years. Not only do I want to thank you for the valuable knowledge you shared with me and the fact that you created the opportunity for the donation of your SQUID microscope to the group, but also for the inspiring and enjoyable time we had in the lab operating the microscope together!

Alexander (Brinkman) en Alexander (Sasha Golubov) wil ik bedanken voor alle geboden hulp als ik weer eens een vraag had over theoretische aspecten gerelateerd aan het onderzoek. Jullie fundamentele kennis is in een experimenteel ingestelde omgeving van grote waarde. Jaap zou ik graag willen bedanken voor de nuttige discussies over SQUIDs.

I would like to thank Simon van der Ploeg and Zhenya Il'Ichev for their help in realizing the CPR measurements at the IPHT in Jena, and Li Xing for his help with the piezo based SSM system. Paul wil ik graag bedanken voor de gerealiseerde Nikkel teststructuren.

Acknowledgements

Ans en Inke wil ik natuurlijk ook van harte bedanken. Een promotie volbrengen zonder jullie administratieve ondersteuning lijkt mij zeker niet aan te raden. Harry en Jan zou ik graag willen bedanken voor de (zo goed als) continue toevoer van vloeibaar helium en de hieraan gerelateerde geboden technische ondersteuning.

Maarten en Jeroen, van harte bedankt voor het nakijken van de meest gelezen delen van dit proefschrift. Bert, Hendrie en Rob wil ik graag bedanken voor het nuttige werk dat zij tijdens hun afstudeeronderzoek hebben verricht. Tevens wil ik Johannes bedanken voor de hulp bij het realiseren van de in dit proefschrift beschreven ruismetingen. Ik heb met zeer veel plezier met jullie samengewerkt.

Gedurende de jaren heb ik het genoegen gehad met een aantal collega's het kantoor te delen: Koray, Mark, Maarten en Jeroen, bij deze wil ik jullie bedanken voor de leuke tijden die wij samen hebben gehad.

Voor alle gezelligheid in het lab, in de kroeg, tijdens conferenties en andere activiteiten dien ik een hele lijst promovendi, studenten en anderen te bedanken, te weten: Kris, Martin van E., Martin P., Johannes, Reinder, Kees, Alexandar, Alexander B., Jeroen, Mark, Maarten, Rob, Joost, Thijs, Koray, Harald, Hendrie, Simon, Bert, Claire, Pieter, Arjen M., Arjen J., Fran(s)k!, Matthijn, Paul, Martijn the L., Joska, Peter de V., Vedran, Kurt, Sybolt, Karthi en Ariando. Ik wens jullie allen veel succes in de toekomst.

Grote waardering heb ik voor de onvoorwaardelijke steun die mij altijd is geboden door mijn ouders. Hoewel jullie ver weg wonen heb ik nooit het gevoel gehad niet op jullie te kunnen rekenen. Mijn dank is groot voor alles wat jullie in mijn leven voor mij en natuurlijk ook voor Mirièl hebben gedaan.

Tevens kon ik altijd rekenen op de steun van andere familieleden. Oma, Miriël en WG, bedankt voor het feit dat ik altijd terecht kon bij jullie in het zonnige Limburg. Wim en Jopie wens ik te bedanken voor al hun advies aangaande mijn toekomstige betrekkingen. Tonny en Jeannette, bedankt voor alle steun die jullie aan Meriam en mij hebben geboden de afgelopen jaren. Hoewel jullie officieel geen familie zijn, zijn jullie dat de laatste jaren gevoelsmatig natuurlijk wel geworden.

Tot slot wil ik graag Meriam bedanken voor haar onvoorwaardelijke steun, liefde en toewijding. Met het afronden van mijn promotie breekt een nieuwe periode aan in ons leven. Samen staan wij sterk, zo ook in deze toekomstige fase!

Aico